TECHNISCHE UNIVERSITÄT WIEN
Vienna | Austria

Diplomarbeit

Numerical Simulations of an Electrochemical Flow Cell using Finite-Element Simulations

Ausgeführt am Institut für Angewandte Physik
der Technischen Universität Wien

unter der Anleitung von
Ao.Univ.Prof. Dipl.-Ing. Dr.techn. Michael Schmid
und
Dr.techn. Jiří Pavelec

durch
Claus Kovacs

Acknowledgements

A thesis is not the work of a single person. Many people have contributed to its success and I am grateful for every contribution. I want to thank my supervisors Michael and Jiří for their support especially throughout the challenging year 2020. Additionally, I want to thank Gareth S. Parkinson for giving me the opportunity to work in this highly interesting field of surface science through his ERC project. Special thanks go to Ulrike Diebold for introducing me to the surface science group and starting this whole journey for me. For their help with electrochemistry I want to express my gratitude towards Lukas Kalchgruber and Dominik Dworschak. Last but not least I want to thank my parents for their unending support!

Abstract

Our everyday lives depend greatly on catalytic processes and since we should take responsibility on utilising our available resources provided by nature with greatest efficiency, optimising these aforementioned methods should have high priority. One method to investigate the catalytic properties of surfaces is by means of electrochemical measurements. For this purpose, a new flow cell will be built to study the performance of single atom catalysts. Among other things, the final design of the flow cell will include in-situ infrared absorption measurements as well as detection of reaction products using mass spectrometry during measurements. To optimise the electrochemical flow cell, simulations utilising the finite-element simulation program COMSOL Multiphysics were performed on a simple test geometry which was deliberately chosen to be as simple as possible to act as an ideal benchmark to test the influence of all involved effects like for example positioning of electrodes. Three different types of simulations were performed and compared to each other. First, all electrochemical processes were substituted by a concentration influx at the working electrode which resembles the case of a perfectly uniform current distribution across the electrode surface. Then simulations were performed using concentration-independent electrode kinetics and to include effects of concentration dependence, simulations using a concentration-dependent Butler–Volmer formalism were performed. Concentration dependence means that the generated species due to the applied electrochemistry influence the cell performance. In the last part of this thesis, two different parameter studies were conducted to determine the impact of different electrode positions and the influence of the channel height, i.e., the distance between working- and counter electrode, on the cell performance. The channel height is crucial when probing with infrared absorption is desired during measurements. Simulation results show that for the simulated experiment (dissolution of metal by an applied voltage pulse) no significant impact of the generated reaction products on the cell performance occurs.

Zusammenfassung

Unser tägliches Leben hängt stark von katalytischen Prozessen ab. Da wir die Verantwortung dafür übernehmen sollten, unsere verfügbaren Ressourcen, die von der Natur bereitgestellt werden, mit größter Effizienz zu nutzen, sollte die Optimierung dieser oben genannten Methoden hohe Priorität haben. Eine Methode zur Untersuchung der katalytischen Eigenschaften von Oberflächen sind elektrochemische Messungen. Zu diesem Zweck soll eine neue Durchflusszelle gebaut werden, um die Leistung von Einzelatomkatalysatoren zu untersuchen. Das endgültige Design der Durchflusszelle umfasst unter anderem die Insitu-Infrarotabsorptions-Messung sowie den Nachweis von Reaktionsprodukten mittels Massenspektrometrie während der Messungen. Um die elektrochemische Durchflusszelle zu optimieren, wurden Simulationen mit dem Finite-Elemente-Programm COMSOL Multiphysics an einer Testgeometrie durchgeführt, die bewusst so einfach wie möglich gewählt wurde, um als idealer Maßstab für den Einfluss aller beteiligten Effekte wie beispielsweise der Positionierung von Elektroden zu dienen. Drei verschiedene Arten von Simulationen wurden durchgeführt und miteinander verglichen. Zunächst wurden alle elektrochemischen Prozesse durch einen Konzentrationsfluss an der Arbeitselektrode ersetzt, der dem Fall einer vollkommen gleichmäßigen Stromverteilung über die Elektrodenoberfläche entspricht. Anschließend wurden Simulationen mit konzentrationsunabhängiger Elektrodenkinetik durchgeführt. Um die Auswirkungen der Konzentrationsabhängigkeit zu berücksichtigen, wurden Simulationen mit einem konzentrationsabhängigen Butler-Volmer-Formalismus durchgeführt. Konzentrationsabhängigkeit bedeutet, dass die aufgrund der angewandten Elektrochemie erzeugten Reaktionsprodukte die Zellleistung beeinflussen. Im letzten Teil dieser Arbeit wurden zwei verschiedene Parameterstudien durchgeführt, um den Einfluss verschiedener Elektrodenpositionen und den Einfluss der Kanalhöhe, d.h. des Abstands zwischen Arbeits- und Gegenelektrode, auf die Zellleistung zu bestimmen. Die Kanalhöhe ist entscheidend, wenn eine Messung mit Infrarotabsorption gewünscht wird. Die Simulationsergebnisse zeigen, dass für das simulierte Experiment (Auflösung von Metall durch einen angelegten Spannungsimpuls) kein signifikanter Einfluss der erzeugten Reaktionsprodukte auf die Zellleistung auftritt.

Contents

Section 1

Introduction

About more than 90 % of all chemical products have been processed using a catalytic process during their production [1, p.1; 2, p.7; 3, p.18]. With the ever-growing demand of resources all around our planet, humankind should strive to not only improve the existing ones, but also develop new, more efficient catalysts. Since heterogeneous catalysis usually happens between the interface of a solid and a fluid, studying the surface with regard to its catalytic properties paves the way to new and improved catalysts. One method of said examination may be performed via electrochemical measurements. To examine surfaces for their catalytical properties by means of electrochemistry, an electrochemical flow cell as depicted in Fig. 1.1 has been proposed [4, p.11].

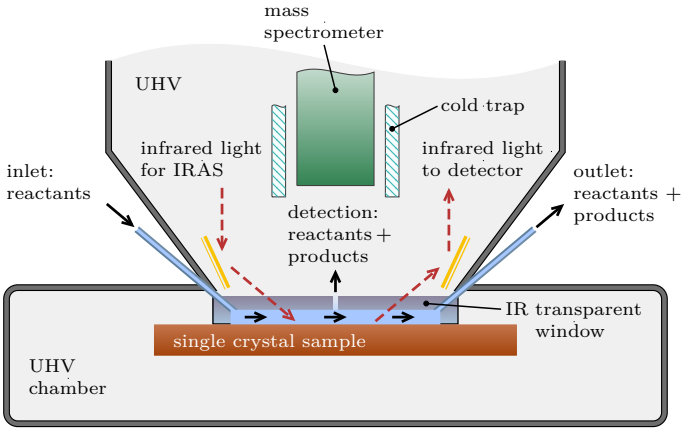

Figure 1.1: **Schematic of a measurement process using the flow cell.** Reactants enter from the left, flow over and react with the surface which acts as the working electrode and exit on the other side. The counter- and reference electrode are not drawn in this schematic. During an electrochemical measurement, the surface of the sample is probed using infrared absorption spectroscopy (IRAS). Adapted from [4, p.11] with permission from the author.

During measurements, e.g., by using voltammetry, potential control will be retained by operating the cell using a three-electrode set-up while the flow of fluid through the electrochemical cell ensures that reaction products created at the surface will be transported from their origin to the point of detection for differential electrochemical mass spectrometry (DEMS). During electrochemical measurements, the surface will be probed using infrared reflection absorption spectroscopy (IRAS). Additionally, the status of the surface will be probed before and after an electrochemical measurement which means the surface must be kept under ultra-high vacuum (UHV) conditions during transfer to not contaminate the surface. Using this set-up, the

surface and its properties can be observed in real time while performing the electrochemical measurement, which will give insight on absorption-desorption processes at the electrode surface with regard to its catalytical properties.

Since the results from measurements using this electrochemical cell will depend on its performance, greatest effort must be made in its design. The main goal of this thesis is to investigate this design by means of numerical simulations utilising the program COMSOL Multiphysics. For this, simulations on a simple test geometry, which still accounts for all significant effects, are performed. Among other things, positioning of the electrodes which influences the current density on the electrodes as well as height of the liquid layer above the sample are important details that need to be resolved in simulations. The latter mentioned distance, which is the channel height, should be as thin as possible to ensure probing using infrared while an electrochemical measurement is being performed, ideally without influencing the electrochemical performance in a negative way. With the results obtained from simulations in this thesis, the real cell can be designed.

In the past, various different experiments and simulations on electrochemical systems have been performed with a selection being listed here. Measurements including infrared spectroscopy, but without liquid flow have been performed [5] on an electrochemical cell with a channel height of 100 µm. Simulation as well as experiments using an electrochemical flow cell with a channel height of 20 µm have been done in Ref. [6]; this design did not include IRAS, however. Similarly, simulations of an electrochemical flow cell with a channel height of 20 µm have been performed [7]. Experiments utilising an electrochemical flow cell without IRAS and with a channel height of 25 µm and 22.5 µm have been described in [8] and [9], respectively. While simulations of electrochemical systems were carried out, they made simplifications with regard to the involved electrochemistry.

This thesis has two main parts, with the first one covering the basics of electrochemistry and the second one presenting results obtained from simulations using COMSOL Multiphysics.

Section 2

Fundamentals

Beginning with a short introduction about thermodynamics, the fundamentals regarding electrochemistry related to this thesis will be presented in this section. These include electrode kinetics, which consists of the Nernst equation as well as the Butler–Volmer equation, both of which are used in the description of faradaic processes. Additionally, the three-electrode set-up including the role of all involved electrodes will be described, which usually represents the operational mode of an electrochemical cell. Following, all used physics modules from COMSOL Multiphysics will be described. The last part of this section will deal with mass transport caused by flow and diffusion.

2.1 Thermodynamics

The Gibbs free energy for a system containing a single phase is given by [10, p.697 & 126]

$$G(p,T) = H - TS = U + pV - TS, \tag{2.1}$$

with enthaply H, temperature T, entropy S, internal energy U, pressure p and volume V of the examined system. The total differential of Eq. (2.1) is

$$dG = dU + pdV + Vdp - TdS - SdT, \tag{2.2}$$

which reduces to

$$dG = dU + pdV - TdS, \tag{2.3}$$

for constant pressure and temperature.

Using the first law of thermodynamics [10, p.175], Eq. (2.3) can be rewritten as

$$dG = \underbrace{\delta Q - pdV}_{dU} + pdV - TdS = \delta Q - TdS. \tag{2.4}$$

The heat Q is a path-dependent process function and therefore the infinitesimal change in its value is denoted by δQ[1]. The second law ot thermodynamics [10, p.336] states that

$$TdS \geq \delta Q, \tag{2.5}$$

which results in a negative change of the Gibbs free energy dG when the system is not at equilibrium and dG equals zero at equilibrium.

[1] Such infinitesimals are called *imperfect differentials* [11, p.20]. Additional information about this topic can be found in [12, p.36ff].

For a reversible process involving particles of various chemical species i, the change of the internal energy U can be written as [11, p.35ff; 12, p.217]

$$dU = TdS - pdV + \sum_{i=1}^{n} \mu_i dN_i + \ldots, \tag{2.6}$$

where dN_i denotes an infinitesimal change in the number of particles N_i of the species i as particles are added or subtracted. In this equation, μ_i is the chemical potential. This means, contributions to the internal energy due to a change in composition in a multi-component system are considered. All other contributions to the internal energy like, e.g., electric, magnetic or gravitational effects are not included in the equation. Using Eq. (2.6) the chemical potential can be calculated as

$$\mu_i = \left(\frac{\partial U}{\partial N_i}\right)_{S,V,N_{j\neq i}}, \tag{2.7}$$

which describes the change in energy due to a change in the number of particles. Since it is not so easy to keep the volume and entropy constant while changing the number of particles, it is convenient to express the chemical potential as a dependence on the change of Gibbs free energy. Inserting Eq. (2.6) into Eq. (2.2) yields

$$dG = Vdp - SdT + \sum_{i=1}^{n} \mu_i dN_i, \tag{2.8}$$

and the chemical potential can be written as

$$\mu_i = \left(\frac{\partial G}{\partial N_i}\right)_{T,p,N_{j\neq i}}. \tag{2.9}$$

The change in the Gibbs energy of a system at constant temperature and pressure is given by

$$dG = \sum_{i=1}^{n} \mu_i dN_i, \tag{2.10}$$

which means that for example a reaction of two participating species at the thermodynamic equilibrium is characterised by

$$dG = 0 \quad \Rightarrow \quad \mu_1 dN_1 + \mu_2 dN_2 = 0. \tag{2.11}$$

Hence, from Eq. (2.11) one can see that under the above stated assumptions, any increase in species one with chemical potential μ_1 must result in an equal decrease of the other species with chemical potential μ_2.

2.2 Electrode Kinetics

Processes occuring at the electrode are of heterogeneous nature which means they occur at the interface of the electrode and electrolyte. These can be described by the transfer of electrons through the surface in which they are called faradaic processes or happen without charge transfer. The latter ones, called non-faradaic processes can be described by charging of the surface using a capacitance.

Faradaic currents are named after Michael Faraday who, after performing electrolysis, published 1833 his law which connects the current flowing through a cell with the amount of material produced. The reaction rate occurring at an area A due to the current i is given by [13, p.22]

$$\text{Rate}\left(\text{mol s}^{-1}\,\text{cm}^{-2}\right) = \frac{i}{nFA} = \frac{j}{nF}, \tag{2.12}$$

which depends on the current density j given in units of $\text{A}\,\text{cm}^{-2}$, n being the stoichiometric number of electrons in the process and F representing the Faraday constant. Depending on the direction of electron flow with regard to the surface, faradaic currents can either be categorised as oxidation or reduction. Oxidation is defined as a process where a reactant is converted into a product (in the solution), while electrons are transferred into the metal surface. The metal surface acts as an electron sink (anode). Reduction occurs when the oxidant (electron acceptor) reacts to the product (in the solution) while electrons are being moved from the metal interface into the solution. In this case the electrode (conductive electrode) acts an electron source and is called cathode. Please note that the involved processes are usually of a complex nature involving multiple steps and additionally including surface reactions (adsorption, desorption) [13, p.23].

A selection of equations and description of their processes involving electron transfer through the electrode surface will be presented hereinafter.

2.2.1 Nernst Equation

The following reaction will be considered where substance A reacts to B and vice versa. Its respective reaction is given by [14, p.57]

$$\text{A} \underset{\text{k}_b}{\overset{\text{k}_f}{\rightleftharpoons}} \text{B}. \tag{2.13}$$

The constants k_f and k_b usually are temperature-dependent and denote the reaction rate coefficient in forward- and backward direction, respectively. For example a greater value of k_f means that the conversion from A to B happens more frequently. The differential equation describing the reaction defined in Eq. (2.13) is given by [14, p.57]

$$\frac{d[\text{A}]}{dt} = -\text{k}_f[\text{A}] + \text{k}_b[\text{B}], \tag{2.14}$$

with square brackets denoting concentrations of the species. With the initial concentration [A] set to one and the requirement that concentration is conserved, i.e., [A] + [B] = 1, the solution of Eq. (2.14) is given by

$$[\text{A}] = \frac{\text{k}_b + \text{k}_f\,\text{e}^{-(\text{k}_f+\text{k}_b)t}}{\text{k}_f + \text{k}_b}. \tag{2.15}$$

At equilibrium the concentrations do not change, i.e., $d[A]/dt = 0$. Using this, the equilibrium constant K_{eq} can be calculated from Eq. (2.14) which is given by

$$K_{eq} = \frac{\text{k}_f}{\text{k}_b} = \frac{[\text{B}]_{eq}}{[\text{A}]_{eq}}. \tag{2.16}$$

The concentrations at equilibrium ($[A]_{eq}$ and $[B]_{eq}$) can be determined by evaluating the limit of Eq. (2.15) as time t goes to infinity which gives

$$[A]_{eq} = \lim_{t\to\infty} \frac{k_b + k_f\, e^{-(k_f+k_b)t}}{k_f + k_b} = \frac{k_b}{k_b + k_f}. \tag{2.17}$$

The influence of the equilibrium constant K_{eq} on the concentrations at equilibrium is shown in Fig. 2.1.

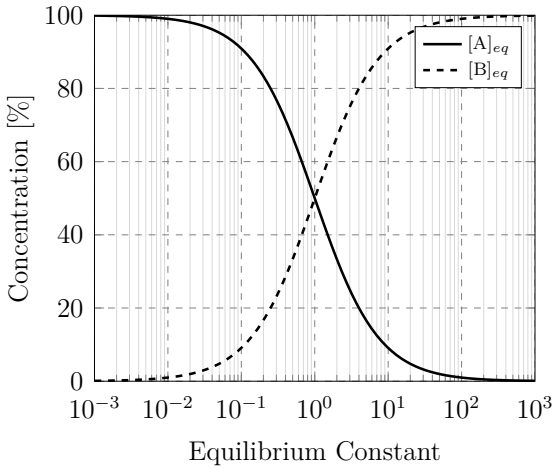

Figure 2.1: **Equilibrium concentrations $[A]_{eq}$ and $[B]_{eq}$ vs. K_{eq} using $k_b = 1$.** This figure shows $[A]_{eq}$ using Eqs. (2.16) and (2.17). The equilibrium concentration $[B]_{eq}$ is given by conservation of concentration, i.e., $[B]_{eq} = 1 - [A]_{eq}$. Depending on the magnitude of K_{eq}, the equilibrium concentrations for the two species $[A]_{eq}$ and $[B]_{eq}$ vary to one or the other extreme. At low values, the forward reaction from A to B is suppressed which leaves a greater concentration of the initial concentration A at the equilibrium. At equality, i.e., $k_f = k_b$, the speed of both forward and backward reaction are equally fast which results in $[A]_{eq} = [B]_{eq} = 0.5$. For high values of k_f the forward reaction of Eq. (2.13) prevails. In this situation the concentration of reactants B dominates due to the product A being turned into B with a high turnover rate in the forward direction of the reaction.

In general, the equilibrium constant is given by [15]

$$K_{eq} = \frac{\prod_j^p a_j^{\nu_j}}{\prod_i^r a_i^{\nu_i}}, \tag{2.18}$$

with the indices j and i indicating products and reactants of the reaction, respectively, as well as their associated activities a_k and stoichiometric coefficients ν_k. While the equation above is expressed through the activity, this quantity is usually not easy to determine. The activity is defined as [16, p.158]

$$a_i = e^{(\mu_i - \mu_i^\circ)/RT}, \tag{2.19}$$

with μ_i° being the chemical potential under standard conditions [17; 16, p.153ff]. The activity is dependent on concentration, temperature, pressure, interaction between chemical species, etc. At low concentrations the activity can be expressed as a ratio of the concentration c and a standard concentration c° using $a_i = c_i/c^\circ$, which usually applies to the conditions in

electrochemical cells [16, p.164ff]. When the system is not at equilibrium, K_{eq} depends on the time and is given by [15; 16, p.204]

$$Q = \frac{\prod_j^p a_j^{\nu_j}(t)}{\prod_i^r a_i^{\nu_i}(t)}. \tag{2.20}$$

Q is the reaction quotient. Figure 2.2 shows the concentrations of the species as well as the reaction quotient for the reaction given by Eq. (2.13), assuming $K_{eq} = 1$.

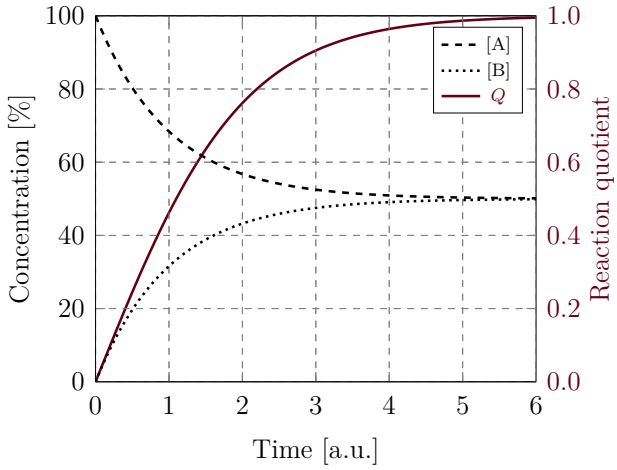

Figure 2.2: **Time evolution of reaction A $\underset{k_b}{\overset{k_f}{\rightleftharpoons}}$ B, given by Eq. (2.15) using $k_f = k_b = 0.5$.** Starting from the initial concentration values [A] = 1 and [B] = 0, the concentration [A] decreases while [B] increases as species A is converted into B. Additionally, the reaction quotient Q = [B]/[A] for each time is shown; Q converges against the equilibrium constant K_{eq}.

The dynamic behaviour of the reaction including its direction can be characterised using the values of Q and K_{eq}, as can be seen in Fig. 2.2. While Q is smaller than K_{eq}, the reaction shifts 'to the right' side of the equation, meaning that reactants are consumed and products emerge. At equilibrium both are the same and in the case of Q being greater than K_{eq}, the back reaction is favoured, which means that products are transformed into reactants.

At any point in a chemical reaction the driving force of the reaction ΔG is given by [13, p.51; 16, p.204]

$$\Delta G = \Delta G^\circ + RT \ln Q, \tag{2.21}$$

with G being the Gibbs free energy, ΔG° the Gibbs free energy under standard conditions and Q the reaction quotient. Standard conditions are defined at 1 bar pressure and substances have unit activity [18, p.293]. At constant temperature and pressure, the maximum additional non-expansion work $w_{\text{add, max}}$ is given by [16, p.99]

$$w_{\text{add, max}} = \Delta G. \tag{2.22}$$

To move n number of moles from one electrode to the other, the work nFE must be exerted, where E is the applied electric field between both electrodes. For the above stated assumptions (p, T = const; non-expansion work) this amount of work is equivalent to a decrease in the Gibbs free energy according to [13, p.48f; 16, p.220]

$$\Delta G = -nFE, \tag{2.23}$$

in which E is the cell potential, F the Faraday constant and n is the number of moles of electrons transferred during the reaction. The potential difference E when no current flows through the cell is called *emf* (electromotive force) and its sign in Eq. (2.23) ensures that for a positive *emf* the reaction happens spontaneously [13, p.49; 16, p.219]. Equation (2.23) relates the total charge transferred during the reaction (nF) to the electric potential E of the cell. Under standard conditions this becomes [13, p.49]

$$\Delta G^\circ = -nFE^\circ, \tag{2.24}$$

with E° being the standard redox potential. Substituting Eqs. (2.23) and (2.24) into Eq. (2.21) yields

$$\underbrace{-nFE}_{\Delta G} = \underbrace{-nFE^\circ}_{\Delta G^\circ} + RT \ln Q. \tag{2.25}$$

$$E = E^\circ - \frac{RT}{nF} \ln Q, \tag{2.26}$$

which is the Nernst equation and its importance resides in the fact that it describes potentials occurring in an electrochemical cell depending on the associated activities. While the equations above are expressed through the activity, this quantity is usually not easy to determine. At low concentrations and standard temperature and pressure, concentrations can be used in place of activities [13, p.52].

With the Nernst equation, cell potentials depending on the reaction quotient under non-standard conditions can be determined. There are several limitations of the Nernst equation which may have to be considered. As previously mentioned when replacing Q by a ratio of concentrations, all reactants and products must be diluted, otherwise the activities of the ions must be considered which are usually not easy to determine. Additionally, this equation is only applicable when no external current flows through the cell since any flow of current involves a change in concentrations at the electrode interface as described by Faraday's law [13, p.22]. This leads to an overpotential which will be described in the next section and hence the electrode potential will differ from the equilibrium potential.

2.2.2 Butler–Volmer Equation

In an electrochemical cell the potential difference between an applied potential E and the equilibrium potential is the overpotential η which is defined as [13, p.22; 19, p.40]

$$\eta = E - E_{eq}, \tag{2.27}$$

with E_{eq} given by the Nernst equation. Hence, the overpotential describes an electrochemical system under non-equilibrium conditions during its operation. Three main parts are contributing to the overpotential which are the activation-, ohmic- and concentration overpotential.

2.2.2.1 Activation Overpotential

The activation overpotential, sometimes called kinetic overpotential stems from the activation energy needed to drive a reaction, i.e., the energy needed to transfer an electron from the electrode surface into the electrolyte. For a one-electron process $O + e^- \rightleftharpoons R$, the relationship between current density i and overpotential η at the electrode-electrolyte interface is described by the Butler–Volmer equation, given by [19, p.37]

$$i = i_{ox} + i_{red} = i_0\Big(\mathrm{e}^{\alpha_a f\eta} - \mathrm{e}^{-\alpha_c f\eta}\Big), \tag{2.28}$$

with the constant $f = F/(RT)$ and i_0 being the exchange current density. In this equation, both anodic and cathodic currents occur simultaneously at the interface, with the factor α_a and α_c denoting anodic and cathodic transfer coefficients, respectively, which may be determined by using cyclic voltammetry (CV) or electrochemical impedance spectroscopy (EIS) measurements. In general, this overpotential mainly depends on the electrode materials and the involved reactions happening at the interface.

Discussion of Parameters Involving the Butler–Volmer Equation

A brief discussion of the parameters of the Butler–Volmer equation will be given in the following section. It is important to note that this discussion only considers the concentration-independent Butler–Volmer equation. Effects due to concentration will be discussed in Sec. 2.2.2.3. Figure 2.3 shows the Butler–Volmer equation according to Eq. (2.28).

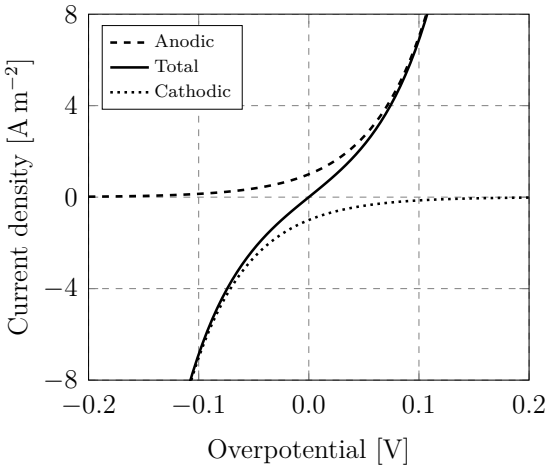

Figure 2.3: **Butler–Volmer equation given by Eq. (2.28) with $\alpha_a = \alpha_c = 0.5$ and $i_0 = 1\,\mathrm{A\,m^{-2}}$.** The anodic and cathodic parts contributing to the current density as well as the total current density are shown.

While for overpotentials η smaller than zero cathodic contributions to the current density dominate, for overpotentials greater than zero anodic contributions prevail. No net current flows at zero overpotential because anodic- and cathodic contributions to the current density cancel each other out. The impact of a change in the exchange current density i_0 on the Butler–Volmer equation is shown in Fig. 2.4.

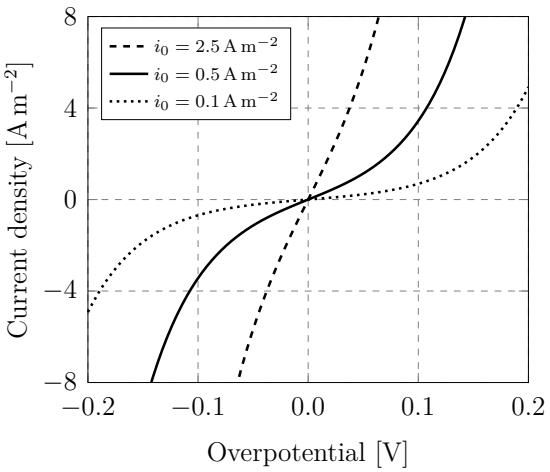

Figure 2.4: **Impact of exchange current density i_0 on the Butler–Volmer equation**. For different values of the exchange current density this figure shows the Butler–Volmer equation according to Eq. (2.28) for symmetrical charge transfer ($\alpha_a = \alpha_c = 0.5$).

With greater values of the exchange current density, more current can be transported through the electrode interface for the same overpotential. The exchange current density depends on the electrode material, temperature, the reaction mechanism, species concentration, etc. [20, 21].

The impact of different anodic and cathodic charge transfer coefficients α_a and α_c is shown in Fig. 2.5.

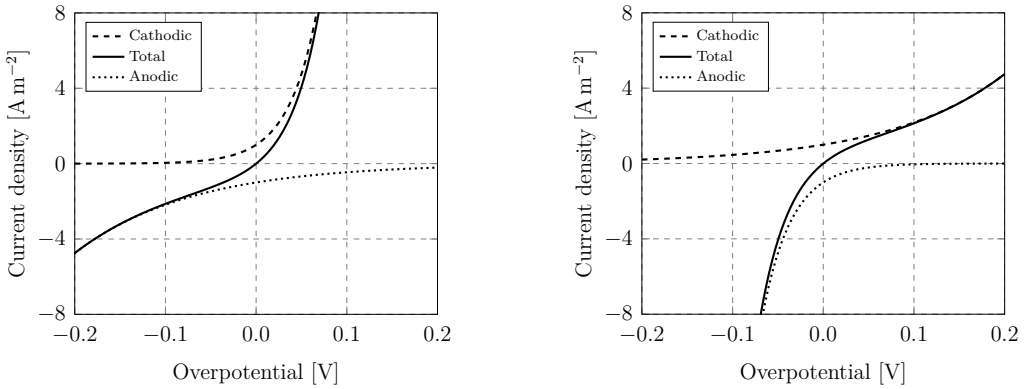

(a) $\alpha_a = 0.8$, $\alpha_c = 0.2$ (b) $\alpha_a = 0.2$, $\alpha_c = 0.8$

Figure 2.5: **Impact of different α_a and α_c on the Butler–Volmer equation**. Cathodic, anodic current densities and their sum according to Eq. (2.28) are shown in this figure.

Limiting Cases

At either high or low overpotentials the main contribution to the current density is dominated by anodic or cathodic currents, respectively. By taking the natural logarithm of both currents

i_{ox} and i_{red} in Eq. (2.28) separately, the following equations called Tafel equations can be obtained.

$$\ln|i| \approx \begin{cases} \ln|i_0| + \alpha_a f\eta & \text{for } \eta \gtrsim +0.1\,V \\ \ln|i_0| - \alpha_c f\eta & \text{for } \eta \lesssim -0.1\,V \end{cases} \tag{2.29}$$

Plots of Eq. (2.29) are called Tafel plots with one being shown exemplarily in Fig. 2.6.

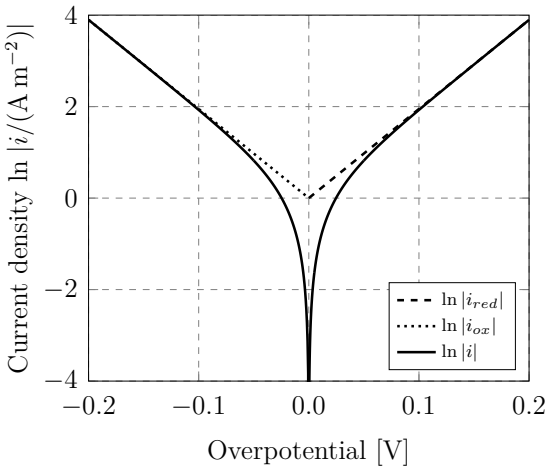

Figure 2.6: **Tafel plot with $\alpha_a = \alpha_c = 0.5$ and $i_0 = 1.0\,\mathrm{A\,m^{-2}}$ given by Eqs. (2.28) and (2.29).**

From these plots the exchange current density and the transfer coefficients can be determined. The exchange current density is the value at which the (extrapolated) lines defined by Eq. (2.29) intersect the y axis. The transfer coefficients define the slope of these lines. Figure 2.7 shows the impact of the transfer coefficients α_a and α_c on the Tafel plots.

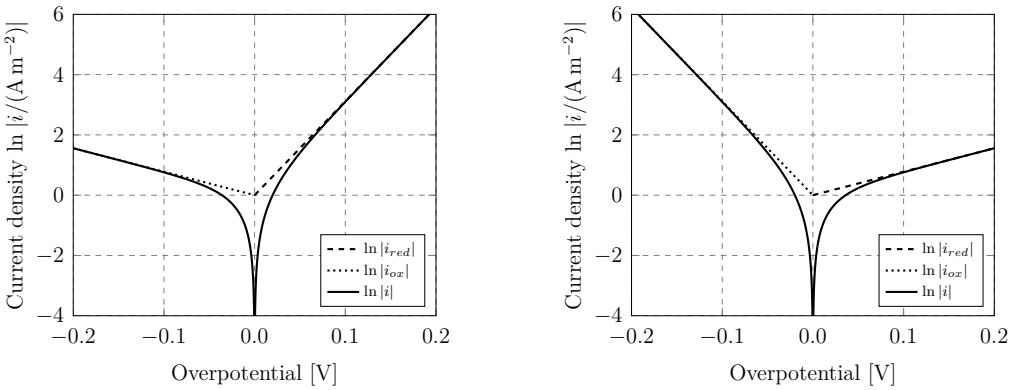

(a) $\alpha_a = 0.8$, $\alpha_c = 0.2$ (b) $\alpha_a = 0.2$, $\alpha_c = 0.8$

Figure 2.7: **Impact of transfer coefficients α_a and α_c on Tafel plots using $i_0 = 1.0\,\mathrm{A\,m^{-2}}$.** This figure shows the Tafel plots defined by Eq. (2.29) and the sum of oxidising and reducing current given by Eq. (2.28).

For numerical simulations, the respective Tafel equation is superior to the Butler–Volmer

equation when overpotentials with an absolute value larger than $\approx 0.1\,\mathrm{V}$ are to be expected. The reason for that is the linear nature of the Tafel equations which makes their computation easier [19, p.38 & 49]. While Tafel plots are used for high overpotential values, for overpotentials with a low absolute value ($< 25\,\mathrm{mV}$ at room temperature), Eq. (2.28) can be linearised into [19, p.37f]

$$i = i_0\big[\underbrace{(1+\alpha_a f\eta+\ldots)}_{\exp(\alpha_a f\eta)}+\underbrace{(-1+\alpha_c f\eta-\ldots)}_{-\exp(-\alpha_c f\eta)}\big] \approx i_0 f\eta(\alpha_a+\alpha_c). \tag{2.30}$$

This equation is known as the linearised Butler–Volmer equation.

2.2.2.2 Ohmic Overpotential

The second contribution to the overpotential is the ohmic- or resistance overpotential η_Ω which describes the influence of the ohmic resistance of the electrolyte. Minimising the ohmic overpotential can be achieved for example by adding an additional supporting electrolyte which reduces the solution resistance. Additionally, for a given cell current, decreasing the distance between electrodes as well as increasing the area of the electrodes reduces the ohmic overpotential.

2.2.2.3 Concentration Overpotential

Since any flow of current causes a change in the concentration of species, the third mentioned contribution to the overpotential is the concentration overpotential η_c. Any change in concentration due to a flow of current results in an extra voltage needed to drive the reaction as described by the Nernst equation. This means additional energy is needed to bring species to the electrode surface. Mass transport by diffusion plays a crucial role in that regard since due to the reaction, oxidising or reducing species get depleted locally in the electrode vicinity which inhibits occurring reactions. Usually the impact of η_c is the more severe, the faster the electrochemical reaction happens, which causes species to be consumed rapidly. Hence, by inducing mixing, e.g., by using a rotating disk electrode set-up, η_c can be minimised.

While the total overpotential can be expressed as the sum of all these three contributions it should be noted that other contributions may exist. Among other things, these are contributions from reactions happening prior to the electron transfer and formation of bubbles. A discussion of the impact of gas bubbles aggregating on the surface and impacting the cell potential can be found in [22]. All these mechanisms, influencing the electrolyte-electrode interface as described above are reducing the performance of the electrochemical cell and are usually referred to as polarisation [13, p.22ff].

2.2.2.4 Concentration-Dependent Butler–Volmer Equation

The Butler–Volmer equation given by Eq. (2.28) is only valid when the electrolyte is being well mixed. Without intermixing, aggregation of reaction products at the vicinity of the electrode-electrolye interface will hinder further reaction. As a result, less current

can be transferred through the electrode surface. This behaviour can be described using [19, p.112]

$$i_{loc} = i_0 \left(\frac{C_R}{C_R^*} \, \mathrm{e}^{\alpha_a f \eta} - \frac{C_O}{C_O^*} \, \mathrm{e}^{-\alpha_c f \eta} \right), \tag{2.31}$$

with the bulk concentrations C_O^* and C_R^* (the concentrations far away from the electrode surface). The two terms in the numerator of Eq. (2.31) are the concentrations of the species at the electrode surface. Without the flow of current ($i_{loc} = 0$), the potential difference obtained from the Butler–Volmer equation agrees with the Nernst equation [19, p.37; 13, p.93ff].

2.3 Three-Electrode Set-Up

When submerging two electrodes into an electrolyte while applying a certain potential between them, due to charge transfer through the electrode-electrolyte interface, species concentration will change, which results in a change of the measured potential. Therefore the measured potential using this set-up will drift as governed by the Nernst equation. To counteract this effect at the CE, a three-electrode set-up can be used as depicted in Fig. 2.8 which enables potential control of an electrode.

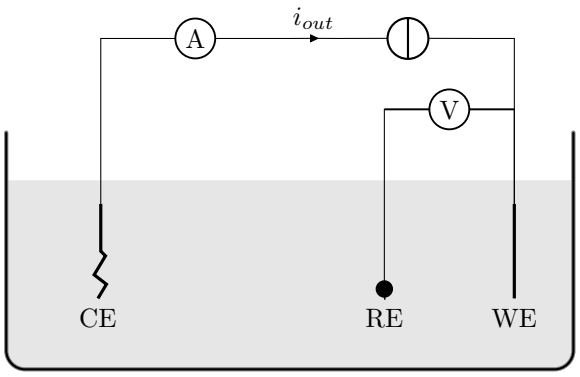

Figure 2.8: **Overview of the three-electrode set-up.** Working electrode (WE), counter electrode (CE) and reference electrode (RE) are submerged in an electrolyte and all charge in the electrochemical cell flows between WE and CE. The variable (DC) current source drives the current i_{out} between WE and CE. Image adapted from [23] in compliance with the CC BY-SA 3.0 licence[2].

Potential control is performed by a potentiostat and goes as follows: All charge is flowing between working- and counter electrode, driven by the (DC) power supply while the voltage is measured between the reference- and working electrode. As soon as the voltmeter shows a deviation between the measured voltage and the desired value (set point), the current applied by the power supply is changed to bring the measured potential back to the desired value. With this set-up, the reference electrode can serve as a stable reference point since no current flows through it.

[2] *Creative Commons Attribution-Share Alike 3.0 Unported.* URL: https://creativecommons.org/licenses/by-sa/3.0/legalcode.

To gain a better insight on its inner workings, the potentiostat will be discussed using the circuit depicted in Fig. 2.9 which represents one of the most simple potentiostats that can be built.

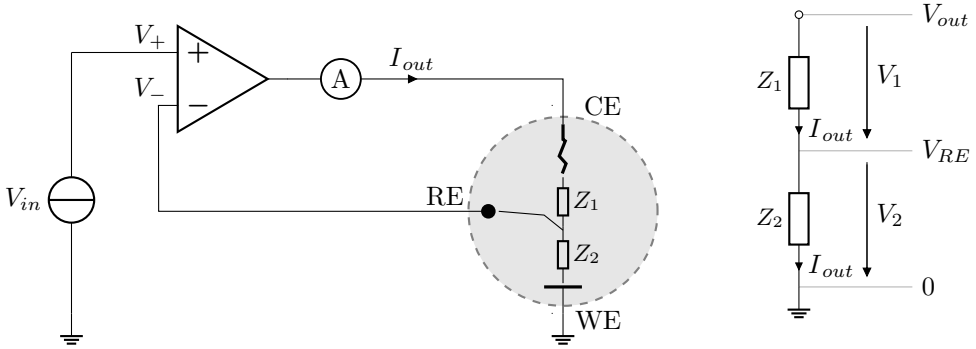

(a) (b)

Figure 2.9: **Electrical circuit of a simple potentiostat.** (a) shows the potentiostat circuit with the electrochemical cell consisting of working electrode (WE), counter electrode (CE) and reference electrode (RE). The cell is marked by a circle and connected to the potentiostat, controlled by an operational amplifier. The voltage divider between CE and WE is depicted in (b) with the total interface impedances Z_1 and Z_2 of CE and WE, respectively. (a) adapted from [24] in compliance with the CC BY-SA 3.0 licence[3].

At the heart of the simple potentiostat, as shown in Fig. 2.9a, is the operational amplifier (op amp). An ideal op amp has infinitely high input impedance, which means that no currents flow in or out of the op amps input terminals. The input terminals are the non-inverting and inverting inputs marked by plus and minus, respectively. If operated in a closed-loop configuration as shown in Fig. 2.9a, the op amp controls the output voltage to maintain the same voltage at the inputs (+, −).

A (variable) voltage V_{in} is applied at the non-inverting input terminal of the op amp against ground. Figure 2.9a is a negative-feedback circuit because a part of the output voltage, determined by the voltage divider, is fed back into the inverting input of the op amp. The operational mode of the potentiostat will be evaluated by analysing the circuit shown in Fig. 2.9a. Since no current flows through the reference electrode (RE), the only path for the output current I_{out} is between CE and WE. The behaviour of the electrochemical cell can be approximated as a voltage divider, as shown in Fig. 2.9b which yields

$$\left.\begin{aligned}(Z_1 + Z_2)\, I_{out} = V_1 + V_2 = V_{out} \\ Z_1\, I_{out} = V_1\end{aligned}\right\} \quad \frac{Z_1 + Z_2}{Z_1}\, V_1 = V_{out}. \tag{2.32}$$

Using the equality of input voltages V_+ and V_- we obtain

$$V_{in} = V_+ = V_- = V_{RE},$$

[3] *Creative Commons Attribution-Share Alike 3.0 Unported.* URL: https://creativecommons.org/licenses/by-sa/3.0/legalcode.

with V_{in} being the input voltage provided by the user and V_{RE} the RE voltage. Since the WE is grounded and V_{in} is set with respect to ground, the input voltage is the same as the voltage between RE and WE. By using $V_1 = V_{out} - V_{in}$, Eq. (2.32) can be rewritten as

$$V_{out} = \frac{Z_1 + Z_2}{Z_2} V_{in}, \tag{2.33}$$

which connects input and output voltage of the op amp, depending on the impedances with the premise that no currents flow in or out of the input terminals of the op amp and that the voltages V_+ and V_- are equal. The current I_{out} at the output terminal is given by

$$I_{out} = \frac{V_{out}}{Z_1 + Z_2} = \underbrace{\frac{Z_1 + Z_2}{Z_2} V_{in}}_{V_{out}} \frac{1}{Z_1 + Z_2} = \frac{V_{in}}{Z_2}. \tag{2.34}$$

The op amp applies and satisfies the conditions desired in potential control in the three-electrode set-up, as shown in Fig. 2.8. While no current flows through the RE interface, the major part of the current flows between CE and WE. The potentiostat maintains the potential between the grounded WE and CE at a fixed value through changing the state of the CE. Further details on this topic can be found in [13, p.632ff; 25, p.61ff].

2.4 Electrodes

In this section the purpose of the electrodes of a three-electrode set-up will be explained.

2.4.1 Working Electrode

The working electrode is the most important electrode of an electrochemical cell. It represents the surface one wants to study, which is subject to potential control as described in Sec. 2.3. Through a measurement, the state of this surface as well as reactions like, e.g., adsorption and desorption can be observed.

2.4.2 Reference Electrode

The purpose of the reference electrode (RE) is to provide a stable reference point against which potentials are being measured. To ensure that the RE potential remains stable during a measurement, no current is allowed to pass through it. Additionally, most RE are decoupled from the electrolyte, which means they are encased in a separate compartment connected to the electrolyte via, e.g., a porous frit. This ensures the flow of electrons and acts as a salt bridge, therefore connecting it to the other electrodes.

The main types of electrodes used as RE are the standard hydrogen electrode (SHE), saturated calomel electrode (SCE) and silver-silver chloride electrodes. In the case of the SHE, a Pt wire is submerged into a 1 M strong acid solution in which hydrogen is being bubbled at 25 °C. Despite the danger of fire explosions of hydrogen and the possible removal of liquid (evaporation) due to bubbling, which would change the concentration, the potential of the SHE is used as a zero point to measure potentials against.

The SCE electrode consists of a mercury electrode coated with calomel (Hg_2Cl_2) and the electrolyte is a solution of potassium chloride (KCl) and saturated calomel (buffered, saturated constant concentration). This extra buffer of salt ensures that the activities stay constant in spite of depletion of ions as they diffuse out of the cell through the liquid junction. The potential is stable as long as the potassium chloride stays saturated. The silver-silver chloride RE, which consists of a silver wire submerged in its precipitated salt AgCl, works similarly to the SCE. A detailed discussion about reference electrodes is given in [26].

2.4.3 Counter Electrode

The purpose of the counter- or auxiliary electrode is to complete the circuit which means the current in a three-electrode set-up flows between counter- and working electrode. The CE should not limit the current in the cell to ensure probing of the WE. For that, the size of the CE is usually chosen to be significantly larger than that of the WE to not limit the kinetics of the reaction. This electrode is usually made of a non-polarisable[4] inert material like platinum, gold or glassy carbon [26, p.13ff]. An inert electrode transports electrons through the surface but does not participate in the redox reaction, which means that no ions are emitted into the solution.

2.5 Finite Element Analysis

Numerical simulations with the finite element program COMSOL Multiphysics® 5.4 (Build: 346) were performed to aid the design process as well as gaining insights on the inner workings (e.g. the mass transport) of the electrochemical cell. In this section, the program COMSOL Multiphysics and its mode of operation with regard to this thesis will be discussed.

A simulation in COMSOL Multiphysics may include the following steps. First the geometry defining the problem has to be created. The next step is the addition of 'physics' which are realised by modules in COMSOL Multiphysics. Each single module defines a set of equations grouped together, e.g., the *Heat Transfer Module* solves everything related to the analysis of heat transfer. Additionally, boundary and initial conditions may be set as well as other parameters related to the problem like for example material properties. Conveniently, all modules can be combined and coupled to build a more complex model if needed. All modules related to this thesis will be described in the next section. The third step is the creation of a mesh, called meshing, which defines the spatial grid on which the equations are being solved. Here the aspect of finite element analysis comes into play since the equations are solved on a grid in space. Therefore, one should always keep in mind that the results of a simulation are always interpolated solutions of equations that have been solved on discrete points in space, and they do not represent analytical solutions. The fourth step is the creation of a study which defines in which way the equations are processed. For example time-dependent studies and stationary studies are available depending on whether the solution changes with time or not. During this step it is possible to adjust the solver which solves the mathematical equations. Here, for example the solver accuracy can be adjusted which sets the accuracy at which the solver stops and this impacts how accurate the obtained solution is. Following

[4] Electrodes forming a capacitance by a Helmholtz layer are called "polarisable".

a successful simulation, the results can be visualised and post processed in various different ways to extract and display the desired informations needed.

2.5.1 Used COMSOL Multiphysics Modules

Since modules used during simulations define the physics and with that the solved equations, they will be described briefly. In this section, illustrations of variables follow the depiction used in COMSOL Multiphysics with vectors being marked boldly.

2.5.1.1 Laminar Flow

The first module used is called *laminar flow* and simulates physics involving the flow of fluids [27]. In this thesis the flow was simulated using laminar flow. This module was used because the flow in the cell is expected to be laminar, which will be shown on page 24. The time-dependent form of the Navier–Stokes equation which is solved in this module is given by

$$\begin{aligned} \rho\frac{\partial \boldsymbol{u}}{\partial t} + \rho(\boldsymbol{u}\cdot\nabla)\boldsymbol{u} &= \nabla\cdot\underbrace{[-p\boldsymbol{I}+\boldsymbol{K}]}_{\boldsymbol{\sigma}(\boldsymbol{u},p)} + \boldsymbol{F}, \\ \boldsymbol{K} &= \mu\big(\nabla\boldsymbol{u} + (\nabla\boldsymbol{u})^T\big). \end{aligned} \tag{2.35}$$

In this equation ρ is the density of the fluid, μ its dynamic viscosity, p the pressure, $\boldsymbol{u}$ the velocity, $\boldsymbol{I}$ the second order identity tensor, $\boldsymbol{\sigma}(\boldsymbol{u},p)$ the stress tensor and $\boldsymbol{F}$ denotes a given external force. For a stationary study the first term $\rho(\partial\boldsymbol{u}/\partial t)$ in Eq. (2.35) is zero. Additionally to the Navier–Stokes equation, the continuity equation given by

$$\nabla\cdot\boldsymbol{u} = 0, \tag{2.36}$$

is solved during a simulation using the *laminar flow* module.

2.5.1.2 Transport of Diluted Species

The second module used is called *transport of diluted species* and it deals with chemical reactions with regard to transport, kinetics, etc. [28]. The physics used from this module is the convection-diffusion equation, given by

$$\begin{aligned} \frac{\partial c_i}{\partial t} + \nabla\cdot\boldsymbol{J_i} + \boldsymbol{u}\cdot\nabla c_i &= R_i, \\ \boldsymbol{J_i} &= -D_i\nabla c_i. \end{aligned} \tag{2.37}$$

In this equation c_i is the concentration of the species i, D_i is the diffusion coefficient, $\boldsymbol{u}$ denotes the velocity field the species is moving with and R_i describes source or sink terms. Similarly to the Navier–Stokes equations, the first term $\partial c_i/\partial t$ is set to zero during a stationary study. The second term $\nabla\cdot\boldsymbol{J_i}$ describes diffusion with $\boldsymbol{J_i} = -D_i\nabla c_i$ being Fick's first law and $\boldsymbol{u}\cdot\nabla c_i$ represents flow, as calculated by the *laminar flow* module.

2.5.1.3 Electrochemistry

This module is used to simulate various electrochemical processes involving a flow of current combined with chemistry (e.g. electrolysis, batteries, corrosion, electroplating, etc.). Faradaic currents can be simulated using three different methods. They are called primary-, secondary- and tertiary current distribution. The primary current distribution assumes zero overpotential. The secondary current distribution considers overpotentials and the current in the liquid phase is calculated using Ohm's law. The tertiary current distribution solves the full Nernst–Planck equation which means the current in the liquid phase depends on the local concentration of species. More information about current distributions can be found in [19, p.103ff; 29; 30]. All simulations in this thesis were performed using the secondary current distribution, which will be described here briefly.

The main variables of interest being solved for are the electric potential ϕ_s and current density $\boldsymbol{i}$. The electric potential in the electrode, which usually is made of a metallic conductor, is given by [19, p.74]

$$\boldsymbol{i}_s = -\sigma_s \nabla \phi_s, \qquad \text{with} \qquad \nabla \cdot \boldsymbol{i}_s = Q_s. \tag{2.38}$$

The index s indicates the variables in the solid phase and σ_s is the electrical conductivity in the electrode. While the left of Eq. (2.38) represents Ohm's law, the right side represents a charge conservation with Q_s being a current source term given in units of $\mathrm{A\,m^{-3}}$. The potential in the liquid ϕ_l as well as the current density in the liquid phase $\boldsymbol{i}_l$ are calculated similarly as for the electrodes by using [19, p.104f]

$$\boldsymbol{i}_l = -\sigma_l \nabla \phi_l, \qquad \text{with} \qquad \nabla \cdot \boldsymbol{i}_l = Q_l. \tag{2.39}$$

In all simulations the potential was applied directly at the electrode boundary surface. This means, the potential drop in the solid phase of the conductor was neglected. This was done due to the high electrical conductivity in the electrodes. At the electrode-electrolyte interface the kinetics are described using the overpotential η defined by [19, p.132]

$$\eta = \phi_s - \phi_l - E_{eq}. \tag{2.40}$$

E_{eq} is the equilibrium potential which is defined at equilibrium ($\Delta G = 0$) [19, p.35 & 269]. Its value is given by the Nernst equation and it depends on the species concentrations of oxidising and reducing species, temperature, etc. At the electrode surface the sum of all electrode reaction currents is implemented as a current density condition given by [19, p.107 & 129; 29]

$$-\boldsymbol{i}_s \cdot \boldsymbol{n} = \boldsymbol{i}_l \cdot \boldsymbol{n} = i_{DL} + \sum_m i_{loc,m}, \tag{2.41}$$

with i_{DL} being currents arising through non-faradaic reactions (charging of a double layer). During non-faradaic processes no electron transfer through the metal/solution interface occurs despite a flow of current and the energy put into the system is consumed by organisation of the electrode interface, which can be modelled as a parallel-plate capacitor [31–33]. Contributions due to faradaic reactions are represented in the sum of Eq. (2.41). The local current density can be calculated using for example the Butler–Volmer equation. The summation index m is used when more than one reaction is considered during a simulation. Additionally, more information about this module can be found in [19].

2.6 Mass Transport by Flow and Diffusion

During all studies presented in this thesis, mass transport only happens due to diffusion and flow, with electrochemistry being the cause of species generation via faradaic processes. Due to the importance of mass transport in the cell, its concepts of diffusion and flow shall be explored here briefly.

2.6.1 Flow

An important dimensionless number describing flow is the Reynolds number Re, which distinguishes laminar and turbulent flow regimes. The Reynolds number is defined as [34, p.125]

$$Re = \frac{\overline{v} L \rho}{\mu}, \tag{2.42}$$

with $\overline{v}$ being the average velocity, μ the dynamic viscosity and L the characteristic length. At low Reynolds numbers, flow is considered laminar which means it occurs uniformly and smoothly. Above a critical Reynolds number turbulences arise and the flow gets chaotic and unpredictable. There is also an intermediate state in between laminar and turbulent flow where turbulences start to emerge but are still predictable. This flow is usually called transition flow. The characteristic length depends on the geometry of the experimental set-up and has always a unit of length. For example to characterise flow through a pipe, the inner diameter serves as the characteristic length L. In cases where the pipe is only partially filled with fluid or when flow happens in non-circular geometries, the hydraulic diameter, given by $D_h = 4A/P$, is used as the characteristic length. In this representation, A is the cross-sectional area of the flow, and P denotes the wetted perimeter of the cross section. This treatment ensures that the hydraulic diameter for flow in a pipe yields two times the pipe radius. For flow in a square duct with width w and height h, in which the whole cross section is filled with fluid, i.e., no air is being transported, the hydraulic diameter is given by [35, p.91]

$$D_h = \frac{4wh}{2(w+h)}. \tag{2.43}$$

When the height h is much smaller than than the width w, Eq. (2.43) yields a value of $2h$ for the hydraulic diameter D_h. Usually, considerations are made with regard to circular pipes due to their abundant presence in fluid-transport applications but the following discussion will focus on a rectangular cross-sectional area. The reason for that is the geometry of the cell to be studied (see Sec. 3) which has a rectangular rather than a circular cross section. It is important to note that the Reynolds number must not be the sole judgement with regard to fluid flow occurring since other factors like surface roughness and pre-conditioning of the input stream may alter the flow behaviour. While roughness and obstacles of any kind increase the likelihood of turbulences occurring, a well conditioned input stream without inherent disturbances reduces the chance of arising turbulences. Taking pipeflow as an example, the Reynolds number at which turbulences occur is above around 2000 but the limit may reach values of over 100000 with a well conditioned experimental set-up [36, p.2].

The fluid profile $v(z)$ for flow occurring between two parallel plates is [37, p.85]

$$v(z) = -\frac{1}{2\mu}\frac{dp}{dx} z(h-z), \tag{2.44}$$

with the dynamic viscosity μ, the distance h between the two plates and the dp/dx is the pressure gradient causing the flow. The geometric representation defining the problem and its solutions according to Eq. (2.44) for a selection of parameters is shown in Fig. 2.10.

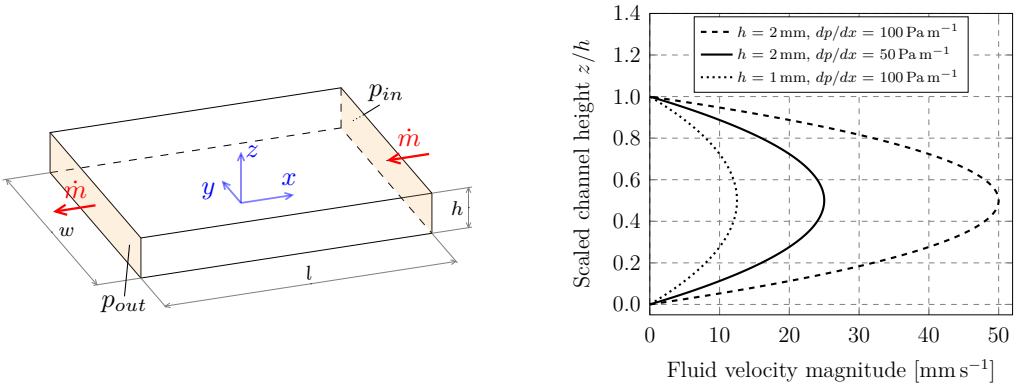

(a) (b)

Figure 2.10: **Mass transport via flow in a square channel**. While (a) shows the considered geometry, (b) shows the corresponding flow profile as defined by Eq. (2.44). The flow profile and with that mass transport through the channel is caused by the pressure gradient $dp/dx = (p_{in} - p_{out})/l$. The variables p_{in} and p_{out} are the pressures at inlet and outlet, respectively; this difference is applied over the distance l. For the dynamic viscosity a value of 1 mPa s was used.

Using Eq. (2.44), the average fluid velocity $\overline{v}$ for flow between two parallel plates is

$$\overline{v} = \frac{1}{h}\int_0^h v(z)\,dz = -\frac{1}{h}\int_0^h \frac{1}{2\mu}\frac{dp}{dx} z\big(h-z\big)\,dz = -\frac{h^2}{12\mu}\frac{dp}{dx}. \tag{2.45}$$

The volume rate of flow Q through the cross-sectional area A is given by [38, ch.(BIB); 39, p.1]

$$Q = A\,\overline{v} = -w\frac{h^3}{12\mu}\frac{dp}{dx}. \tag{2.46}$$

Equation (2.46) is known as the Hagen–Poiseuille law [40, p.61]. The parabolic flow profiles as shown before are a result of the fluid viscosity. As a viscous liquid moves across a surface the molecules closest to the surface adhere to it which is usually denoted as a no-slip condition and hence, fluid velocity directly at the surface is zero.

2.6.2 Diffusion

Compared to flow, the description of diffusive processes is rather simple, assuming that species only occur in dilute states. In this case, these processes can be described using Fick's laws. Considering a one-dimensional problem, Fick's first law is given by [41, p.2]

$$F = -D\frac{\partial C}{\partial x}. \tag{2.47}$$

F is the rate at which the concentration C diffuses through an area per unit time. $\partial C/\partial x$ is the concentration gradient causing this flux and D is the diffusion coefficient given in units of area per unit time. Fick's second law in one dimension is given by [41, p.4]

$$\frac{\partial C}{\partial t} = D\,\frac{\partial^2 C}{\partial x^2}. \tag{2.48}$$

The average length L a particle has diffused after the time t is called diffusion length. For a one-dimensional problem its value is given by [42, p.815]

$$L = \sqrt{\langle x^2 \rangle} = \sqrt{2Dt}. \tag{2.49}$$

Section 3

Methodology, Results and Discussion

The following section will present and discuss simulation[5] results utilising the program COMSOL Multiphysics. At first, all employed methods utilised to approach the problem will be explained, which includes among other things the chosen geometry and used simulations parameters with regard to the employed physics. The second part deals with the mesh refinement study which is necessary to ensure the independence of simulation results from the chosen mesh. In the third part, simulation results using a homogeneous concentration influx through the surface defining the working electrode surface will be presented. Following that, simulations utilising concentration-independent electrode kinetics will be discussed as well as simulations including effects caused by concentration dependence. Finally, the last part of this section will deal with the impact of changing cell parameters on the cell performance. The investigated cell parameters are electrode positioning and changes in the channel height. The latter parameter defines the distance between working electrode (WE) and counter electrode (CE).

3.1 Methodology

Figure 3.1 shows the considered cell geometry which is valid for all simulations, excluding the ones involving parameter studies. For these simulations the geometry will be defined later on during its discussion.

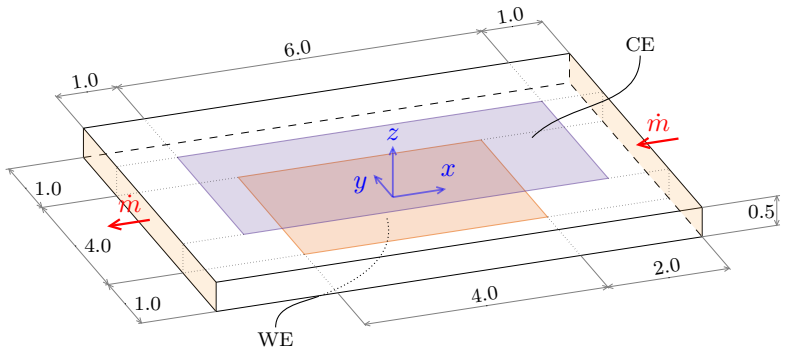

Figure 3.1: **Geometry of the simple test cell in compliance to COMSOL Multiphysics**. This model only depicts the volume occupied by the fluid phase. All units in this figure are given in units of millimetres. See text for details.

[5] The computational results presented in this thesis have been achieved using the Vienna Scientific Cluster (VSC).

Throughout all simulations in this thesis, the WE will always be positioned at the point of origin (centre at x = y = z = 0). Additionally, it will always have the same spatial dimensions. This geometry, including electrode placement, serves as a model test cell for designing the real cell. This means, the final design will look different from what is shown Fig. 3.1. For simulations utilising flow, the inlet is always positioned at x = 4 mm and the outlet is on the opposite side (x = −4 mm). In the *laminar flow* module, all walls except the inlet and outlet are subject to a no-slip condition which means the fluid velocity at these walls is zero. At the outlet a pressure of p = 0 is assumed. At the surface defining the inlet a pressure of 1 Pa is applied. This pressure difference was chosen arbitrarily and does not represent the pressure difference in the final cell design. Using the *laminar flow* module, the velocity profile was calculated. On the inlet surface and outlet surface a pressure condition was applied. At the inlet this condition is given by [27, p.148f]

$$\begin{aligned} \boldsymbol{n}^T[-p\boldsymbol{I}+\boldsymbol{K}]\boldsymbol{n} &= -\hat{p_0}, \\ \hat{p_0} \geq p_0, \quad \boldsymbol{u}\cdot\boldsymbol{t} &= 0, \end{aligned} \tag{3.1}$$

with $\boldsymbol{n}$ being the surface normal, $\boldsymbol{t}$ the tangent vector of the surface and p_0 is the given pressure (1 Pa at the inlet and 0 Pa at the outlet). The inequality in Eq. (3.1) means that backflow is suppressed. A similar condition was applied at the outlet surface which is given by [27, p.148]

$$\begin{aligned} [-p\boldsymbol{I}+\boldsymbol{K}]\boldsymbol{n} &= -\hat{p_0}\boldsymbol{n}, \\ \hat{p_0} \leq p_0, \end{aligned} \tag{3.2}$$

but with the difference that normal flow is not enforced. In both Eqs. (3.1) and (3.2), $\boldsymbol{K}$ denotes the viscous stress tensor [27, p.128] as defined in Eq. (2.35) and $\boldsymbol{I}$ is the second identity tensor. The auxiliary variable $\hat{p_0}$ ensures that no fluid flows in the wrong direction (backflow suppression). Taking the outlet as an example, the normal stress on the respective boundary is adjusted so that $\boldsymbol{u}\cdot\boldsymbol{n} \geq 0$. To achieve this, the prescribed pressure is p_0 if $\boldsymbol{u}\cdot\boldsymbol{n} \geq 0$, but smaller where $\boldsymbol{u}\cdot\boldsymbol{n} < 0$. The inlet is treated similarly but on this boundary the pressure is adjusted so that $\boldsymbol{u}\cdot\boldsymbol{n} \leq 0$ is satisfied. More information about inlet and outlet conditions is given in [27, p.141ff]. Both inlet condition and outlet condition were set to respective pressure values and no other changes were made at these surfaces. This means, the conditions given by Eqs. (3.1) and (3.2) represent the default initialisations in COMSOL Multiphysics.

The Reynolds number was calculated for a variation of channel height and inlet pressure according to Eq. (2.42). This is shown in Fig. 3.2.

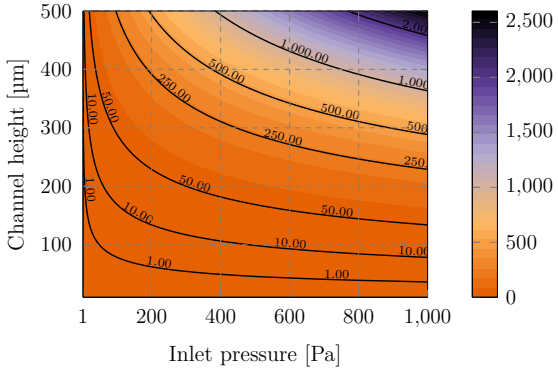

Figure 3.2: **Reynolds number depending on channel height and inlet pressure.**

The length over which the pressure was applied was set to 8 mm. The Reynolds number for a cell with a channel height of 0.5 mm and an inlet pressure of 1 Pa is 2.6. Therefore, the flow is laminar in that case since a Reynolds number above around 1000 is considered to cause turbulent flow in a rectangular channel [43, p. 407 & 449]. This justifies the usage of the *laminar flow* module for the considered geometry. Three different types of simulations were performed. First, a simulation using the *transport of diluted species* module was performed. Using this module, a homogeneous concentration influx over the working electrode surface was applied. The second type of simulation considers electrochemistry. In the *electrochemistry* module, the CE was electrically grounded ($\phi_s = 0$) and at the WE a certain potential was applied. The current density over both electrode surfaces was calculated using a concentration-independent Butler–Volmer equation. The influx of concentration at the WE was realised using an electrode-surface coupling in the *transport of diluted species* module. This means, the creation and annihilation of species is proportional to the current density on the WE surface. The third kind of simulation is similar to the second one but uses a concentration-dependent Butler–Volmer equation at the WE surface. For all simulations using the *electrochemistry* module, symmetric electron transfer ($\alpha_a = \alpha_c = 0.5$) was assumed to take place on both electrode surfaces.

Material parameters were chosen to resemble a possible electrochemical cell. Copper was used for the WE and platinum for the CE. At the WE, which acts as the anode, copper is oxidised and the reaction at this surface is given by

$$\mathrm{Cu(s)} \rightarrow \mathrm{Cu^+(aq)} + \mathrm{e^-}. \tag{3.3}$$

At the platinum CE it is assumed that hydrogen ions are catalysed to hydrogen gas. This reaction is given by

$$2\,\mathrm{H^+(aq)} + 2\,\mathrm{e^-} \rightarrow \mathrm{H_2(g)}. \tag{3.4}$$

The formation of H_2 bubbles was not considered. For the electrolyte, sulphuric acid with a concentration of $10\,\mathrm{mol\,m^{-3}}$ was used. The corresponding electrochemical parameters are given in Table 3.1

Table 3.1: **Electrochemical cell parameters used for COMSOL Multiphysics simulations**. Copper was used as a working electrode (WE) and platinum as a counter electrode (CE). Equilibrium potentials (eq. pot.) are referred against the standard hydrogen electrode (SHE) potential.

Property	Value	Description	Reference
$E_{eq,CE}$ [V]	1.188	Eq. pot. CE against SHE	[44, p.F3034; 13, p.809]
$E_{eq,WE}$ [V]	0.52	Eq. pot. WE against SHE	[13, p.808]
σ [$\mathrm{S\,m^{-1}}$]	4.8	Electrolyte conductivity	[45, p.422; 46, ch.5-71]
$i_{0,CE}$ [$\mathrm{A\,m^{-2}}$]	10.0	Exchange current density of CE	[47, p.354; 48, p.5410]
$i_{0,WE}$ [$\mathrm{A\,m^{-2}}$]	240.0	Exchange current density of WE	[47, p.289]

The diffusion coefficient of the species was set to $10^{-9}\,\mathrm{m^2\,s^{-1}}$. This value holds true for most diluted species in aqueous solutions [49, p.127 f]. A dynamic viscosity of 1 mPa s was used which is the value of water at around 293.15 K [50, p.944ff]. The reaction was chosen arbitrarily and may be different from the reactions of interest in the final cell.

3.2 Mesh Convergence

Performing a mesh refinement study is crucial to verify that the results obtained from simulations represent a valid solution to the given problem. Since time and space are always solved discretised, a convergence study must include a mesh refinement study to ensure that the obtained simulation results are independent of the underlying spatial partitioning. Additionally, it should also include a time-convergence study in which the independence of simulation results with regard to the time step of the solver is examined. Additional parameters like the set accuracy of the solver, must also be considered in this type of study. All these parameters affecting the simulation accuracy may influence each other and one should keep in mind that convergence is a local phenomenon, which means that the solution does not change everywhere the same way when the above mentioned parameters are varied.

In COMSOL Multiphysics the mesh can either be generated using an inbuilt method which creates the mesh automatically depending on the physics employed in the simulation or the mesh can be custom built. The downsides of the automatic mesh generation are the dependence of the mesh on the total size of the geometry and the suboptimal usage of mesh element types. Mesh element types are the building blocks out of which the mesh is being generated, e.g., tetrahedra or cubes. When letting COMSOL Multiphysics take responsibility of meshing, parameters like the maximum mesh element size depend on the size of the geometry, hence it is hard if not impossible to compare the same automatically generated mesh type on different geometries. The second drawback of automatic mesh generation is the fact that it only uses tetrahedra to build the mesh. Using these types of elements, any geometry can be meshed but it comes with the disadvantage of unoptimised usage of mesh elements. A different mesh element than the default may depict the spatial geometry as well as the employed physics in a better way and therefore a custom mesh is usually superior compared to the automatically generated one. Additionally, a custom-built mesh usually optimises the mesh with regard to the geometry, i.e., the mesh is only as dense as necessary to depict the given problem. Beyond a certain threshold, a mesh that is too fine will only result in longer computational times without adding any precision. For certain geometries like ones with a high aspect ratio (which is the case of most geometries in this thesis), these two factors may influence each other in a bad way resulting in a highly suboptimal automatically generated mesh, therefore creating a custom mesh is always advised. The idea of a mesh convergence study is to run the same simulation for different meshes and compare the solutions against each other. When the difference between solutions for different meshes is small enough one can conclude that the obtained solution is independent of the mesh.

3.2.1 Mesh Parametrisation

Due to the square cell geometry a custom mesh was built made out of cubes. To be able to compare solutions using different meshes conveniently against each other, all parameters involving the mesh were defined using a single mesh parameter p. All used mesh properties are listed in Table 3.2 and they were defined arbitrarily for the selected geometry.

Table 3.2: **Properties defining the mesh of the simple test cell**. Using the function $\mathrm{f}(p) = 1 - p$ and $\mathrm{floor}(p)$ which returns the nearest previous integer the parameters of the mesh are defined. See text for details.

Property	Value
Maximum mesh element size [mm]	$\mathrm{f}(p)$
Minimum mesh element size [mm]	$0.01\,\mathrm{f}(p)$
Number of boundary layers	$1 + \mathrm{floor}\left[10\,(1 - \mathrm{f}(p))\right]$
Boundary layer stretching factor	1.2
Thickness of first layer [mm]	$0.05\,\mathrm{f}(p)$

Due to the square geometry of the simple test cell, a mapped mesh was chosen to build the mesh. This mapped mesh was applied at the inlet and swept over the geometry, i.e., swept from inlet to outlet. The properties defining the mesh which are listed in Table 3.2 will be discussed briefly. The maximum mesh element size and minimum mesh element size define the respective size a mesh element can be generated. The last three properties listed in Table 3.2 define the properties of the boundary layers. When using the *laminar flow* module the mesh will be generated with a boundary layer mesh which is a denser mesh at the walls. This is necessary because directly at these surfaces the fluid has zero velocity (no-slip condition) which results in high velocity gradients. To resolve the solution in this regions a denser mesh is required in the vicinity of the walls. The properties of this boundary layer mesh is defined by the thickness of the first layer, the total numbers of boundary layers and the boundary layer stretching factor. The latter property defines the factor of growth between each layer, i.e., it specifies how much the next layer may grow with regard to the previous one. All these mesh properties are now solely defined via the mesh parameter p which indicates the quality of the mesh, with zero indicating a very coarse and one a very fine mesh, as shown in Fig. 3.3.

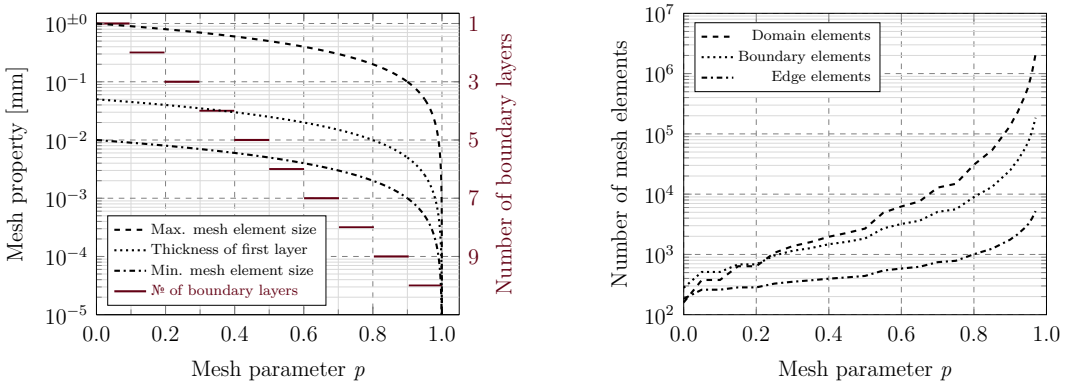

Figure 3.3: **Geometric presentation of mesh properties for the simple test cell**. (a) shows the maximum mesh element size, thickness of the first mesh layer, minimum mesh element size and the number of boundary layers depending on the mesh parameter p as defined in Table 3.2. Please note that the number of boundary layers is depicted using a linear axis scale while the other properties are shown utilising a logarithmic axis. (b) shows the number of mesh elements by generating a mesh using a certain mesh parameter p with 0.97 representing the maximum value. See text for details.

The total number of mesh elements may serve as a rough estimate for the simulation time. Additional factors influencing the time a simulation needs to run are for example the employed

element order as well as the time-dependent behaviour of the solution. Within each mesh element as depicted in Fig. 3.4 shape functions are defined. The solution of the equations is then the linear sum of these shape functions which can be for example of linear, quadratic or cubic order which is the order of the employed polynomials. For higher-order shape functions, i.e., higher element order, additional points must be defined across the mesh, hence the increase in needed computational resources. Additional information about this topic can be found in [51]. Creating a mesh using the parameter p yields a mesh with a certain amount of mesh elements which is shown in Fig. 3.3b. For small parameters p the mesh is coarse and has fewer elements compared to larger mesh parameter. The mesh consists of elements at the walls of the geometry called boundary elements and elements at edges denoted edge elements. Any other mesh element is called a domain element. This means, a domain element resides on the inside of the geometry and is not connected directly to a boundary. A mesh visualisation with a mesh parameter $p = 0.25$ is shown in Fig. 3.4.

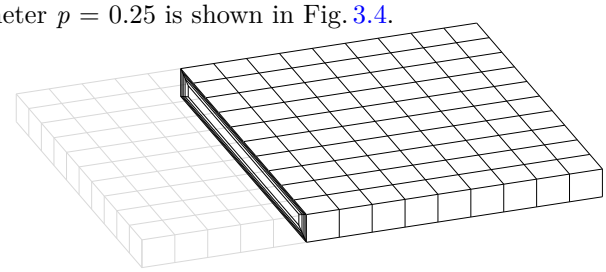

Figure 3.4: **Exemplarily depiction of a mesh using a mesh parameter $p = 0.25$**. Only a part of the mesh is depicted for visualisation purposes.

3.2.2 Application of Mesh Parametrisation for Mesh Convergence Study

Simulations regarding the simple test cell involve the following three steps

1. Stationary study: Laminar flow
2. Current distribution initialisation
3. Time-dependent study: Electrochemistry

All these steps are unified into one single study in COMSOL Multiphysics. This means, during a simulation the above listed study steps are performed sequentially in their respective order. At first, the physics solely concerning laminar flow are being solved. This can be done since the concentrations of all species are low and their impact on the viscosity can be neglected. Therefore, the flow profile is of static non-timedependent nature. The results of this first step are used in the subsequent steps. This means, the generated species due to applied electrochemistry move in the time-constant fluid velocity field. During the second study step, the potential in the liquid and the overpotential are solved using a stationary study which is called current distribution initialisation. This second step is necessary since each step requires initial values which serve as an initial starting point for the simulation. Since electrochemistry is usually hard to compute due to their highly nonlinear nature [19], setting up this initialisation step is advised. The result of the stationary second study step serves as an initial step for the final study step. This third step takes the solution from the initialisation of step two as a starting point while considering the flow field to calculate the time-dependent behaviour of the system due to the applied electrochemistry. All these study steps could have been implemented via a time-dependent study during which all physics are solved for simultaneously. But this would result in a longer simulation time due to the physics regarding

laminar flow being solved during each time step. This study would yield the same results but only if a computation succeeds in the first place due to the complexity of the involved physics. Hence, it is recommended to split the study into steps if feasible.

3.2.3 Mesh Convergence Study

Since the study is split into three parts, the mesh convergence study can also be split into parts. While the convergence study for the first two stationary study steps has to consider only spatial convergence, the last one must consider the behaviour in time as well. Convergence can occur globally or locally. An example of global convergence is when one considers the total current flowing in the cell. With a finer mesh this value may converge against a value and one may deduce convergence of the solution. But to obtain this variable, the local current density must be integrated over the surface. Hence, one loses the local information about convergence. The local convergence also considers variations depending on the spatial position of the mesh. The first step of the study solves the Navier–Stokes equation which yields pressure and velocity at any given point in space. As mentioned earlier convergence can occure locally or globally, with the latter one shown in Fig. 3.7. For the simulations, inlet pressure was set to 1 Pa and outlet pressure to 0 Pa.

3.2.3.1 Global Convergence Study

A global mesh refinement study was performed which is shown in Fig. 3.5.

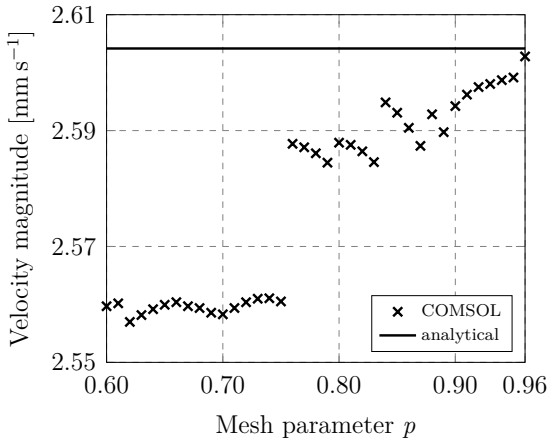

Figure 3.5: **Global mesh convergence: Average fluid velocity magnitude**. Depending on the mesh quality this figure shows the average fluid velocity magnitude which was calculated using the volume average in COMSOL Multiphysics. Additionally, the solid line shows the analytical solution of the average fluid velocity magnitude given by Eq. (2.45) (2.6042 mm s^{-1}).

While there are regions where for subsequential meshes the average fluid velocity magnitude decreases in accuracy, its value approaches the analytical solution with increasing mesh quality in general. The average fluid velocity magnitude does not depend greatly on the mesh since the difference between the best and the worst mesh is less than 2 %. This means, the mesh which is built out of hexahedra depicts the geometry at least for the fluid flow in a good way even for lower quality meshes.

3.2.3.2 Local Convergence Study

Since the global convergence study as described before averages over the volume it does not depict local phenomena of convergence. One way to determine local convergence issues using COMSOL Multiphysics is via a join data set. Using this data set, two solutions can be joined by an operator and this resulting data can be visualised. Using this method, results from simulations with different meshes were joined and the values for pressure and velocity was investigated. The values of the pressure and the fluid velocity magnitude was evaluated on a slice in the yz plane which is shown in Fig. 3.6.

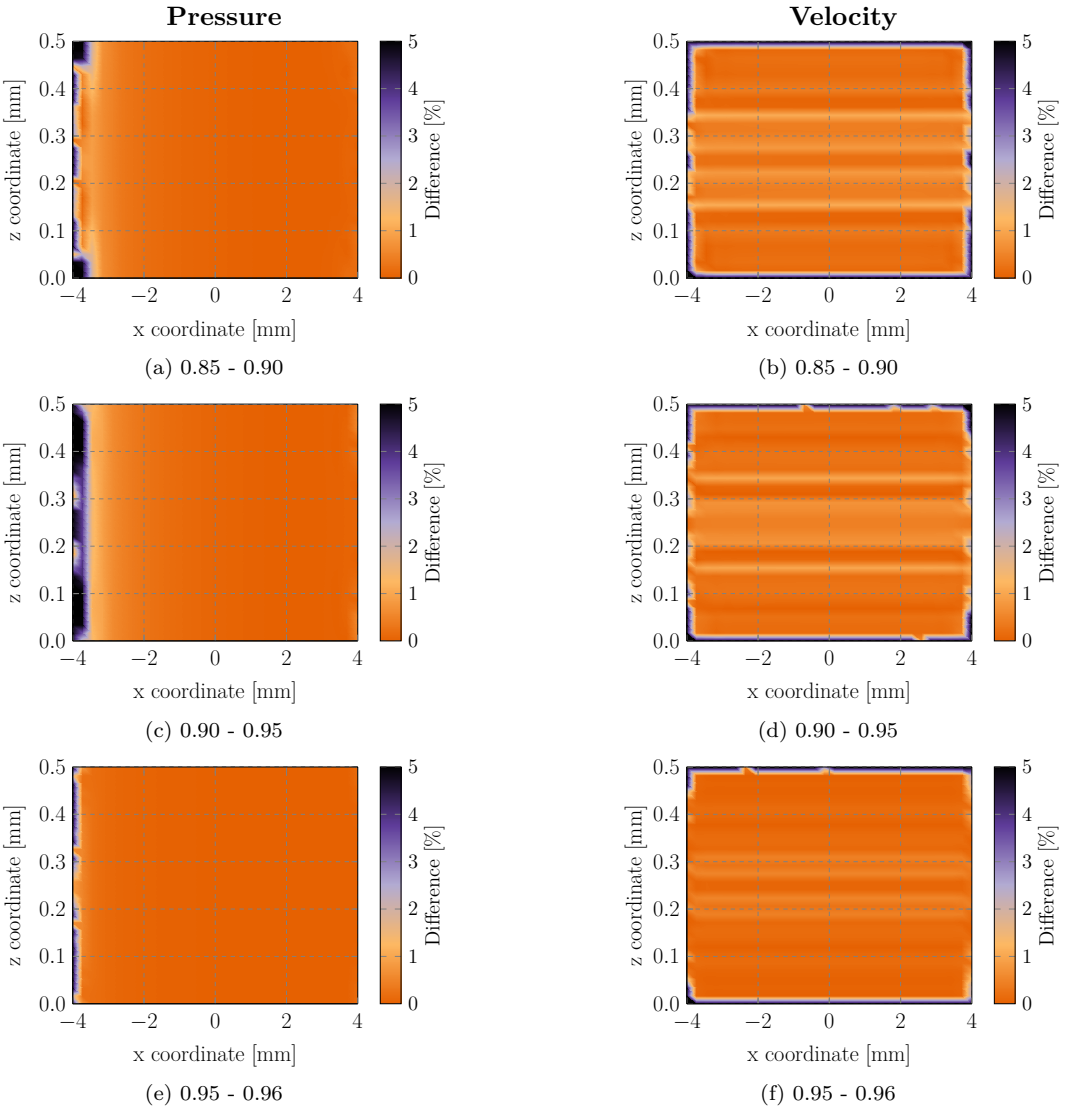

(a) 0.85 - 0.90 (b) 0.85 - 0.90

(c) 0.90 - 0.95 (d) 0.90 - 0.95

(e) 0.95 - 0.96 (f) 0.95 - 0.96

Figure 3.6: **Local mesh convergence (stationary, laminar flow): Slices from COMSOL.** Using a join data set the percentage difference between the simulation results utilising two different meshes was calculated in COMSOL Multiphysics. The three subfigures on the left show differences in pressure and the three subfigures on the right show the evaluation of the velocity magnitude. The considered mesh qualities are given in the subfigure captions. Evaluation of the data was done for an xz slice at y = 0.

Identifying regions where the solutions converge at a slower rate is crucial because these regions need attention. This means, in these regions the mesh needs to be refined or settings in the program must be altered which cause these local convergence issues. Most of the changes in the pressure occur at the outlet (x = −4 mm) while for the rest of the volume the changes are minor. While the differences in pressure at the outlet decrease with increasing mesh quality, they persist for high-quality meshes. The main areas in which the velocity magnitude changes with the mesh are the no-slip boundaries (z = 0 and 0.5 mm) in Fig. 3.6. The data shown in Fig. 3.6 presents a descriptive overview of the differences residing on a slice through the centre of the cell. A different way to present the same data set is by extracting the desired data from a simulation and process this data externally which is shown in Fig. 3.7.

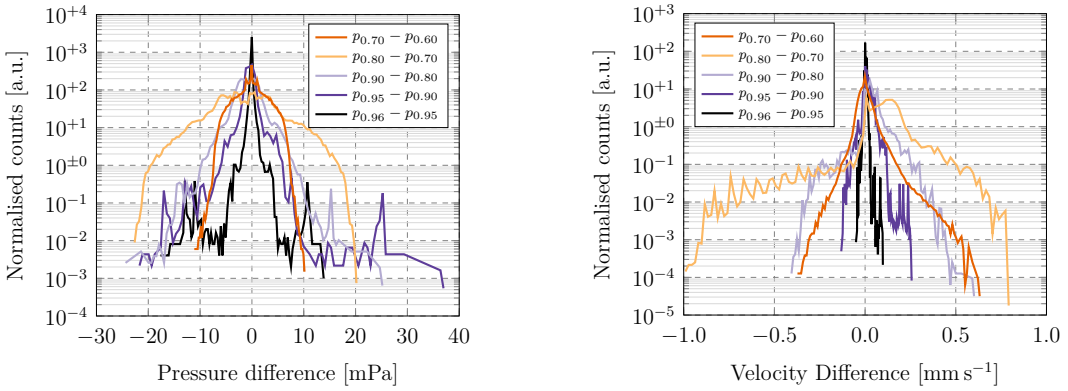

(a) (b)

Figure 3.7: **Global mesh convergence (pressure & velocity), stationary laminar flow study**. Simulations for mesh parameters p = 0.6, 0.7, 0.8, 0.9, 0.95 and 0.96 were performed. On a regular grid of distance 20 µm the values of pressure and velocity magnitude were extracted in each point. Then the difference between two simulations in each point was calculated and binned using a total number of 100 bins spread evenly between the found minimum and maximum value. The lower index of the legend indicates the considered data sets processed. (a) and (b) show a selection of the normalised obtained pressure and velocity magnitude data, respectively.

Both approaches show the same data. Determining positions where convergence may be an issue is easy to examine with a slice evaluation of a join data set in COMSOL Multiphysics directly. Binning and processing the data on the other hand gives information about the convergence over the binned volume with the disadvantage that local effects are not resolvable. Figure 3.7 shows a similar picture as Fig. 3.6. Please note that all data sets shown in Fig. 3.7 are normalised to an area of one and therefore serve as probability density functions.

The reasons for the pressure differences despite the high quality mesh utilised are either due to mesh elements or boundary conditions. For example a mesh element can be distorted or deformed in its positioning causing such behaviour (since all values are examined through these elements). In this case the reason is most likely due to the boundary conditions employed (pressure at inlet and outlet). There are various different ways to apply boundary conditions in the *laminar flow* module in COMSOL Multiphysics like applying a pressure or a velocity. Different boundary conditions have a different robustness of their implementation [27, p.141]. The reason for prescribing a pressure at both inlet and outlet is due to the simplicity in this treatment and additionally the final cell design will be operating by applying pressure

to exert a fluid motion. Due to the main focus of this thesis being electrochemistry, the influence of the small pressure differences for a higher quality mesh at the outlet were disregarded. Additionally, these differences do not interfere with the electrochemistry directly since they do not occur in the vicinity of any electrode surfaces. Due to accuracy and memory constraints, a mesh of quality $p = 0.95$ was chosen for the stationary step involving laminar flow.

3.3 Transport of Diluted Species

At first a simulation using only the two modules *transport of diluted species* and *laminar flow* was conducted. The study in this simulation consists of two steps. First the flow field was calculated using a stationary study and following that a time-dependent study followed which accounts for creation and diffusion of the species. Inflow of concentration was realised using a concentration flux at the working electrode surface. Hence, all electrochemistry was substituted with a simple model using a homogeneous concentration influx across the electrode which means local effects caused due to electrode positioning are not resolved. Various different experiments may be performed using the electrochemical cell, the one focused here being square-wave pulse voltammetry. By using this technique, a voltage pulse of certain duration is being applied at the working electrode while various different parameters of the cell are under investigation. The applied flux on the WE surface is depicted in Fig. 3.8.

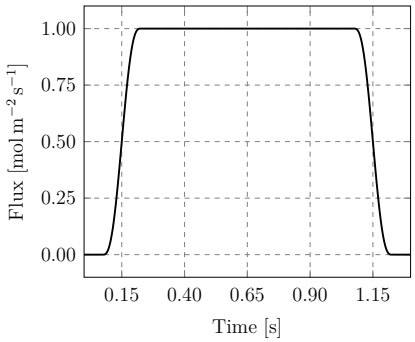

Figure 3.8: **Shape of the flux used in time-dependent mass transport studies**. The flux is defined by a lower limit of t = 0.15 s and an upper limit of t = 1.15 s. Around the rising and falling edge, a size of transition zone of width 0.15 s is being employed which smears the pulse. The area under the curve is one.

The total influx of concentration $C_{tot,c}$ into the cell is 16 µmol. This can be calculated using $C_{tot,c} = J_{0,c} A_{\mathrm{WE}} \Delta t$ with a total flux $J_{0,c}$ set to 1 mol m^{-2} s^{-1}, A_{WE} being the working electrode surface (16 mm^2) and Δt the pulse duration of one second. Broadening or smearing of the pulse at its lower and upper limits is a general approach when dealing with discontinuities of any kind during simulations. Without smoothening the solutions may become discontinuous in space and/or time. Therefore, it is always a good approach to smoothen out jump discontinuities of any kind. During a real experiment using the electrochemical flow cell, the applied voltage pulse at the working electrode provokes a reaction at the electrode-electrolyte interface, accretion or decretion of species occur depending on the sign and magnitude of the applied voltage. This generation of species propagates through space and time towards the outlet of the cell where it may be detected for example by using a mass spectrometer. This

recorded signal is one of the responses of the electrochemical system towards the excitation in form of a voltage pulse and will be called *residence time distribution (RTD)* furthermore. As will be later explained, the RTD-response depends on the geometrical shape of the cell as well as its operational conditions. These conditions include for example operational parameters, like the exerted pressure which defines the fluid flow speed through the cell and the shape of the applied voltage pulse, as well other parameters like surface roughness of walls, used electrolyte (viscosity), temperature, etc. Hence, these response curves may serve as a metric on the quality of the electrochemical cell. By applying an influx of concentration at the working electrode (see Fig. 3.8) and tracking the concentration moving throughout the whole simulated volume, the cell responses as shown in Fig. 3.9 can be generated.

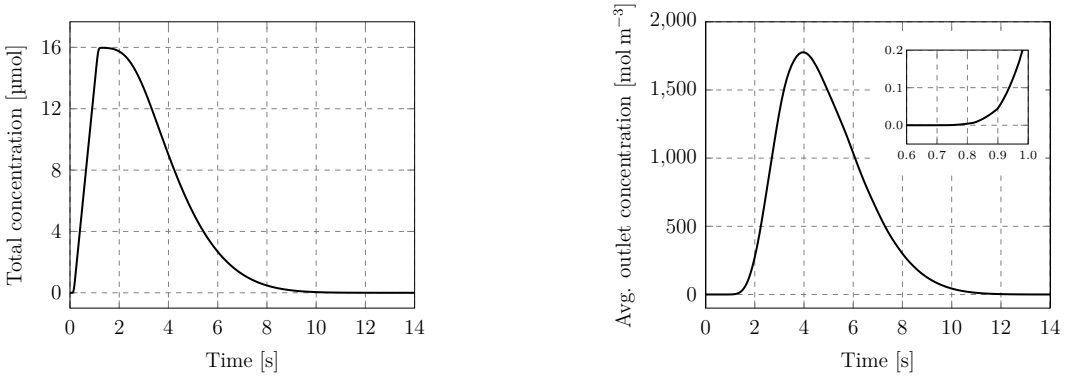

Figure 3.9: **Total cell- and average outlet concentration**. (a) shows the total concentration and (b) the average outlet concentration in the cell for a time-dependent study using a concentration influx as defined in Fig. 3.8. The inset in (b) shows a zoom of the point where the average outlet concentration starts to rise.

With the pressure difference between inlet and outlet set to 1 Pa, the average fluid velocity in the cell is 2.5942 mm s^{-1}. Due to the concentration influx using the square pulse, the first species is being generated at 75 ms which is the time where the concentration start to rise in Fig. 3.9a. With the shortest distance between the working electrode surface and the outlet being two millimetres, the onset of the RTD curve happens at 0.77 s. As will be shown in the next section, for these conditions this happens to be the time it takes species to travel the distance of two millimetres under the average fluid velocity. The maximum of the RTD can be determined by considering the side of the working electrode closest to the inlet. Due to the no-slip conditions at the wall, species transport away from the electrode surface only occurs by diffusion. Species diffused further away from the working electrode surface will be accelerated and be transported faster through the cell which is a major part shaping the RTD curve. With the last species being generated at around 1.225 s and the farthest distance between outlet and electrode surface, the time it takes species to arrive at the outlet on average is 3.69 s which marks the maximum of the RTD. Beyond this point in time, concentration is not generated anymore and can only leave through the outlet. Hence, the decrease of detected species concentration at the outlet beyond the maximum detected concentration occurring at around 3.54 s, as can be seen from Fig. 3.9b. The shape and form of these curves depend on the chosen geometry, operational parameters and physical constants. The applied pressure difference between inlet and outlet and the geometry define the velocity profile. The diffusion in z direction away from the electrode surface depends on the diffusion coefficient. All parameters used for this simulation were chosen arbitrarily.

3.3.1 Parameter Variation

Simulations with different pressure differences between inlet and outlet were performed. While pressure difference was the only parameter which was subject to change, its set value was 0.1, 0.4, 0.7, 1.0, 2.0, 4.0 and 8.0 Pa. Figure 3.10 shows the total cell- and average outlet concentration depending on the applied pressure difference.

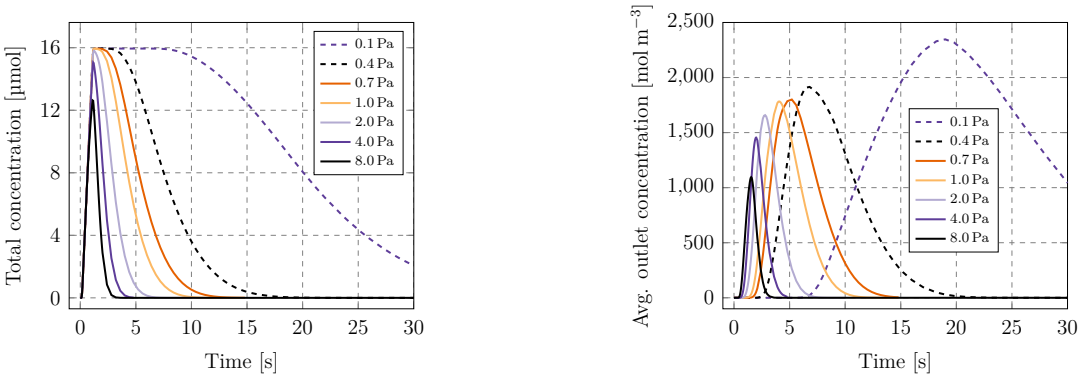

(a) (b)

Figure 3.10: **Total cell- and average outlet concentration**. (a) shows the total concentration and (b) the average outlet concentration in the cell for a time-dependent study using a concentration influx as depicted in Fig. 3.8. The legend indicates the applied pressure difference between inlet and outlet.

When the geometry of the cell remains unchanged and only the pressure difference between inlet and outlet is subject to change, the generated species are transported out of the cell faster with increasing pressure. With a set pressure difference greater than 2.0 Pa, some reaction products leave the cell before the applied pulse at the WE surface ends. Hence, the total amount of generated species (16 µmol) is never inside the cell volume at any given time which can be seen in Fig. 3.10a. The average fluid velocity magnitude was extracted from these simulations which is shown in Fig. 3.11a.

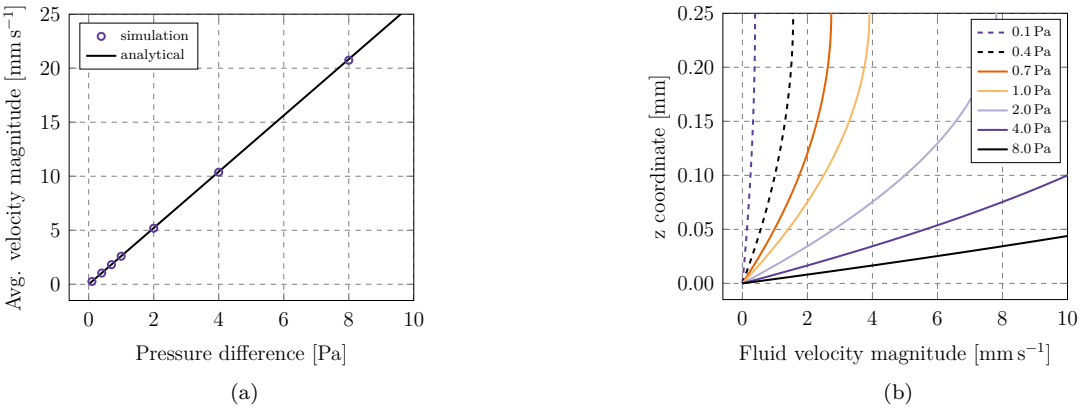

(a) (b)

Figure 3.11: **Average fluid velocity magnitude depending on the pressure difference**. (a) shows the extracted average fluid velocity magnitudes from COMSOL simulations as well as the analytical solution according to Eq. (2.45). (b) shows the velocity profile over half the cell height (0.25 mm) defined by Eq. (2.44).

Figure 3.11b is important for understanding how the reaction products move through the cell, this defines the shape of both the total cell- and average outlet concentration (RTD curve). The products are first generated at the electrode surface which is at height z = 0 in this figure. That means, any species must diffuse away from the electrode surface before it can get moved by the flow of fluid since a no-slip condition is assumed at the surface. For higher pressure differences between inlet and outlet the fluid velocity increases faster with increasing distance away from the electrode surface. This means concerning the shape of the RTD curves, diffusion is mainly responsible for movement perpendicular to the electrode surface and the flow moves the concentration in direction towards the outlet. Both effects are connected since the velocity of the fluid depends on the distance diffused away from the electrode. For each curve shown in Fig. 3.10b two times were extracted. The first is the time at which the average concentration at the outlet starts to rise (onset of the RTD) and the second one is the time at which the maximum average concentration is registered at the outlet (maximum of the RTD). These two data sets are shown in Fig. 3.12.

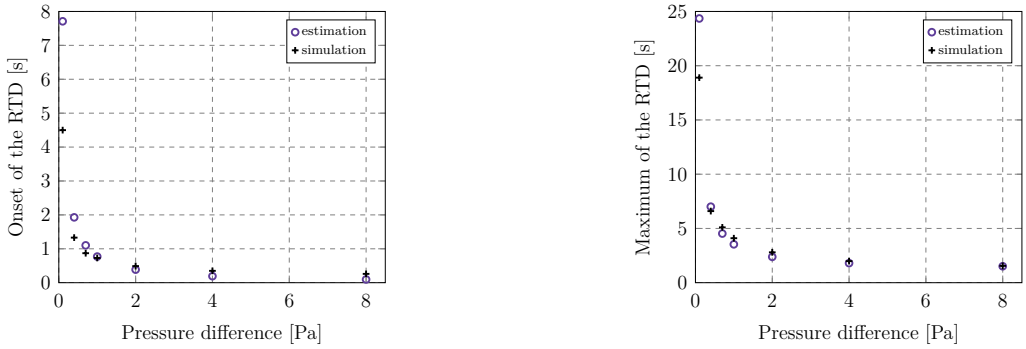

(a) (b)

Figure 3.12: **Maximum- and onset time of the average outlet concentration**. Depending on the applied pressure at the inlet, (a) shows the time at which the average concentration at the outlet starts to rise and (b) shows the time at which the maximum average concentration at the outlet occurs. Both figures show the extracted values from simulations as well as an estimation using the average fluid velocity magnitude. See text for details.

The estimations in Fig. 3.12 were done using

$$\begin{aligned} \text{Onset of the RTD} &= 2\,\text{mm}/\bar{v}, \\ \text{Maximum of the RTD} &= 6\,\text{mm}/\bar{v} + 1.15\,\text{s} + 0.15\,\text{s}/2, \end{aligned} \tag{3.5}$$

with the average fluid velocity magnitude $\bar{v}$. The point in time at which the concentration starts to rise was calculated by dividing the closest distance of the WE to the outlet (2 mm) by the average fluid velocity. It can be seen that the first reaction products can reach the oulet at earlier times than estimated in the case of low pressure difference (low fluid velocities) because then diffusion has enough time to move the products to the centre of the cell, where the fluid velocity is higher than the average. For high pressure differences, the reverse is true.

For the calculation of the time where the concentration at the outlet has its maximum, 6 mm is the distance on the WE farthest away from the outlet and the last two terms in the respective equation shift the time to the end of the pulse (see Fig. 3.8). Beyond this point in time no concentration influx into the cell happens anymore. A detailed discussion of the results from simulations using a pressure difference of 0.1, 1.0 and 8.0 Pa will be discussed and presented following. Figure 3.13 shows the concentration in the centre of the cell (y = 0) for a selection of times.

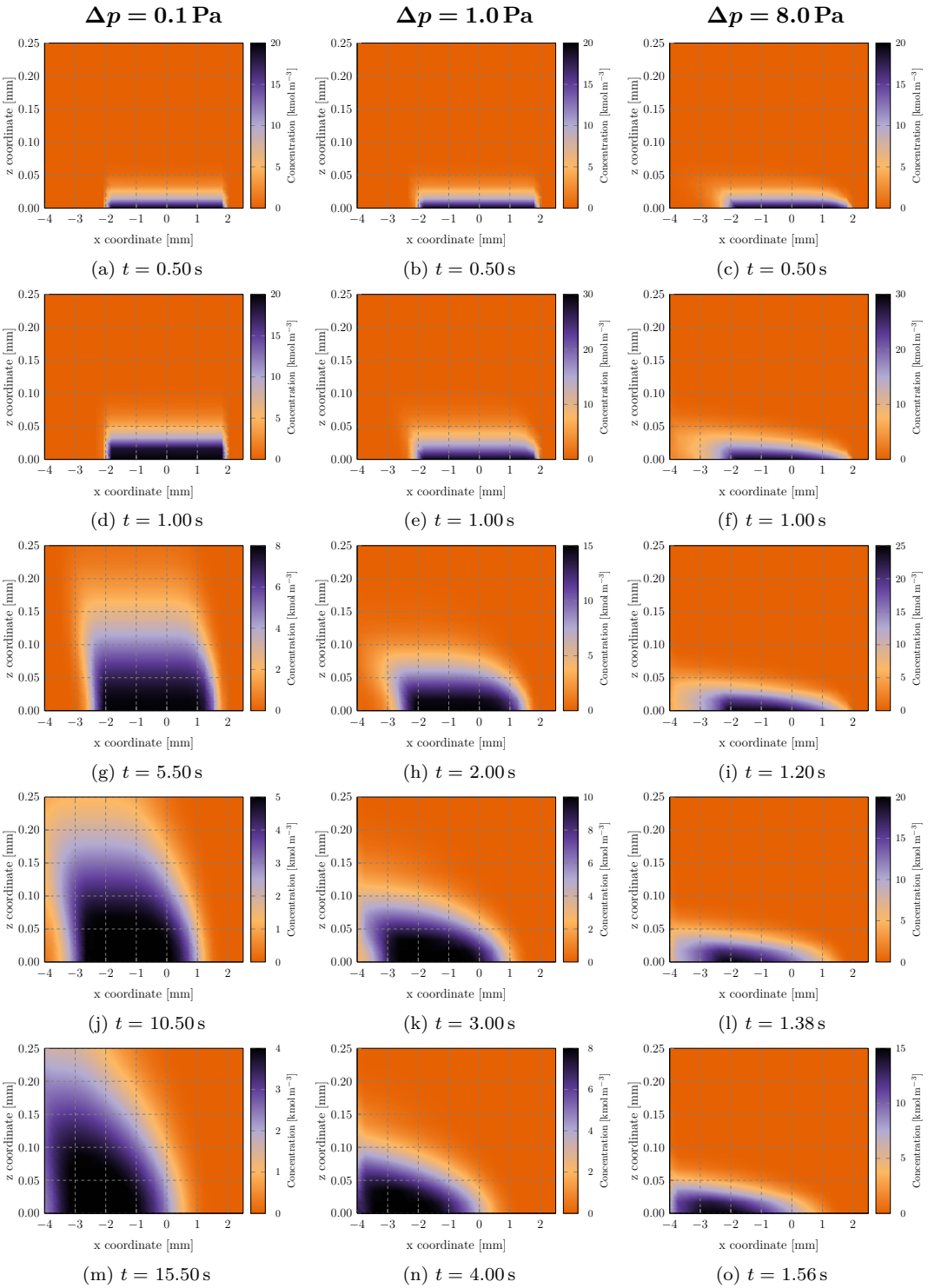

(a) $t = 0.50\,\mathrm{s}$ (b) $t = 0.50\,\mathrm{s}$ (c) $t = 0.50\,\mathrm{s}$

(d) $t = 1.00\,\mathrm{s}$ (e) $t = 1.00\,\mathrm{s}$ (f) $t = 1.00\,\mathrm{s}$

(g) $t = 5.50\,\mathrm{s}$ (h) $t = 2.00\,\mathrm{s}$ (i) $t = 1.20\,\mathrm{s}$

(j) $t = 10.50\,\mathrm{s}$ (k) $t = 3.00\,\mathrm{s}$ (l) $t = 1.38\,\mathrm{s}$

(m) $t = 15.50\,\mathrm{s}$ (n) $t = 4.00\,\mathrm{s}$ (o) $t = 1.56\,\mathrm{s}$

Figure 3.13: **Concentration profiles for different inlet pressures**. For three different inlet pressures ($\Delta p = 0.1$, 1.0 and 8.0 Pa) this figure shows the concentration in the centre of the cell (y = 0). The evaluated times are given in the subfigure captions.

Figure 3.14 shows additional extracted informations from the simulations with a focus on the x position of the maximum of the RTD curves (Maximum of the RTD).

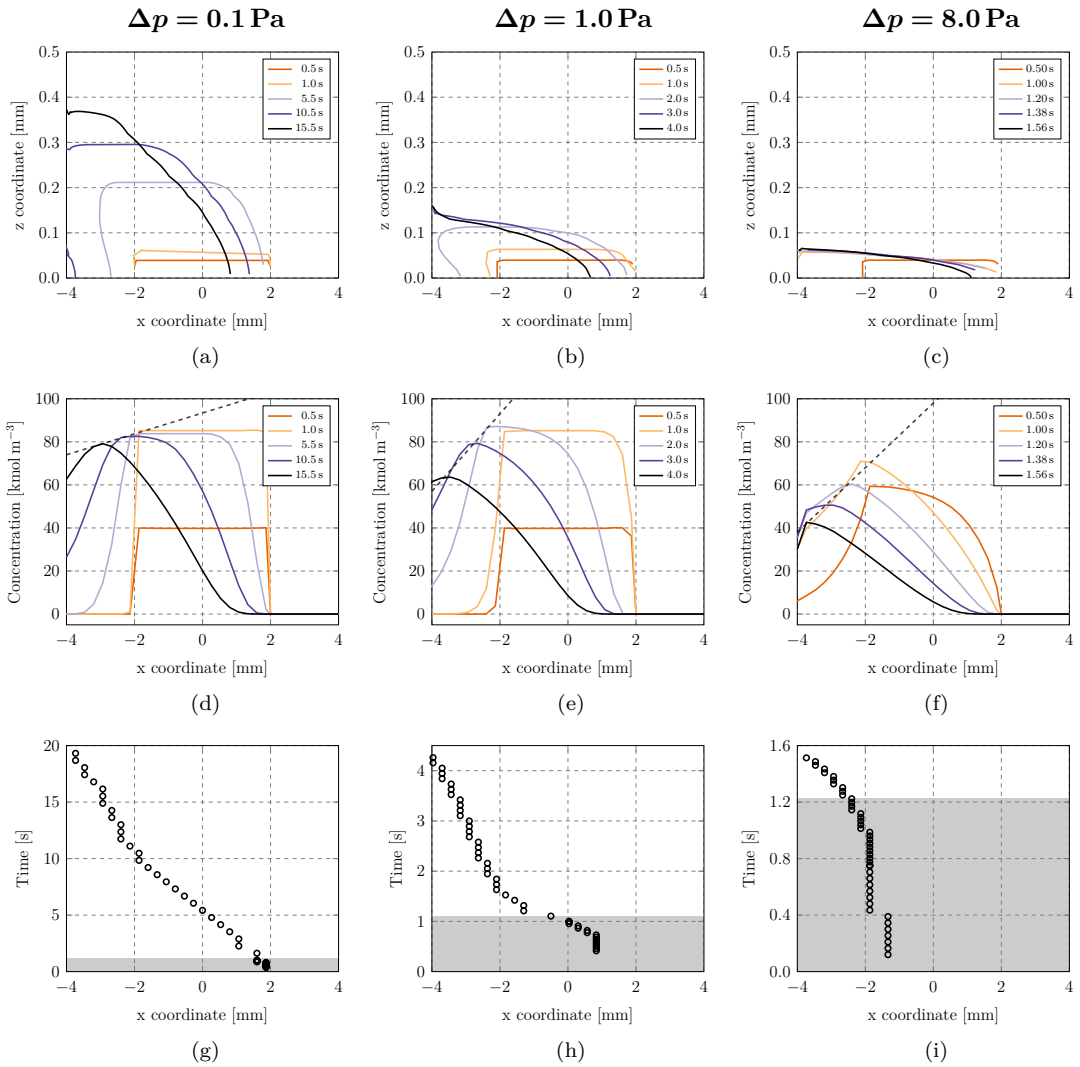

Figure 3.14: **Concentration isolines, sum of concentrations and RTD maximum trace.** Each of the three columns shows extracted data from simulations using different pressure differences ($\Delta p = 0.1$, 1.0 and 8.0 Pa). The first row shows extracted isolines from the data presented in Fig. 3.13. Each one of these lines enclose 95 % of the concentration at the given time. The second row shows the sum of the concentrations in z direction for each x value and additionally a linear function through their maxima is shown for the data points with a time greater than 1 s. The third row shows the x position of the maximum of the RTD curve depending on time for all simulations. Additionally, the time during which an influx of concentration occurs at the WE is highlighted in grey.

The evaluated times for the concentration isolines and the sum of the concentration (first and second row in Fig. 3.14) were chosen deliberately in a way to resolve the pulse. This means, the first two times (0.5 and 1 s) are the same for all three pressure differences. For the remaining three data points the time interval between the end of the applied pulse and

the maximum of the recorded average outlet concentration was divided into equal parts. The second row of Fig. 3.14 shows the sum of the concentrations which was generated from the data which is shown in Fig. 3.13. For each x value, all concentrations in z direction were added up. The evaluation of these curves at the cell outlet ($x = -4\,\mathrm{mm}$) generates the RTD curves (see Fig. 3.10b). The third row in Fig. 3.14 shows the position of the maximum of the z-integrated concentration as a function of time for the whole data set, i.e., for all simulated time steps. From this figure one can see that, depending on the time, the maximum moves linearly through the cell after the pulse was applied at the WE and the concentrations get smeared out enough to show a well defined maximum ($t \gtrsim 1\,\mathrm{s}$ for $\Delta p = 8\,\mathrm{Pa}$, $t \gtrsim 12\,\mathrm{s}$ for $\Delta p = 0.1\,\mathrm{Pa}$).

To gain a better understanding of mass transport depending on flow and diffusion, the following simple model which is shown in Fig. 3.15 will be considered.

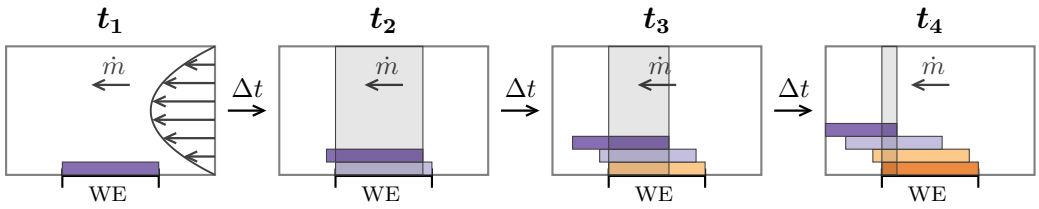

Figure 3.15: **Simple mass transport model (flow and diffusion).** This figure shows a cross section of the cell with the WE on the bottom and flow happens from right to left. The flow profile is drawn schematically for the first time step t_1. In total, four different time steps ($t_1 \ldots t_4$) of the system are shown. The concentration during each time step is depicted as the rectangle. These concentrations are assumed to just move directly away perpendicular from the electrode surface (diffusion in x is neglected). Additionally, the maximum concentration in the slice is highlighted by the shaded grey area.

This simple model gives an intuitive insight on the propagation of concentration through the cell. As concentration diffuses farther away from the electrode surface it experiences a greater velocity and gets displaced more in direction of flow than concentration in the vicinity of the surface; this defines the shape of the high-concentration region (see Fig. 3.13 and the isolines in Fig. 3.14). The maximum of the concentration remains at the surface of the WE as long as the pulse is applied since a steady concentration influx occurs during this time. After the applied pulse the concentration in the cell moves towards the outlet, which defines the location of the concentration maximum (since the concentration farther away of the surface moves faster due to the flow).

Simulation results show that for the given geometry and a certain range of pressure differences between inlet and outlet the maximum position and onset position of the RTD can be estimated using Eq. (3.5). It is important to note that this estimation is only valid for this geometry and applied pressure differences.

3.4 Electrochemistry with Concentration-Independent Current (CIK)

In the previous discussion, all electrochemistry was substituted by using a homogeneous concentration influx through the working electrode. Following, results of simulations using the sec-

ondary current distribution (see page 18) will be presented and discussed.

3.4.1 One-Dimensional Model

To gain a better understanding of the electrochemistry, a one-dimensional model will be discussed first. All involved equations will be solved numerically and compared to results from simulations. We assume a one-dimensional model consisting of two electrodes separated by a distance d as shown in Fig. 3.16.

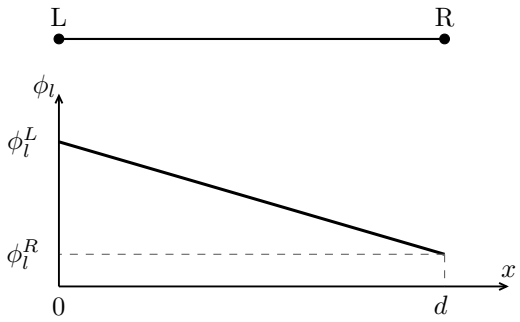

Figure 3.16: **Geometry and liquid potential distribution of the one-dimensional model.** The top part of the figure shows the considered geometry of the one dimensional model consisting of a left electrode (L) and a right electrode (R). The bottom part shows the potential drop in the liquid through the cell which follows a linear trend since the electrical conductivity is assumed to be constant everywhere. Liquid potentials of the electrodes are marked through a subscript, e.g., ϕ_l^L denotes the liquid potential at the left electrode.

For this problem the potentials in the solid phase (ϕ_s^L and ϕ_s^R) are given and the potentials in the liquid phase (ϕ_l^L and ϕ_l^R) are calculated. In this model, concentration overpotentials are ignored and the behaviour of the system is mainly governed by the activation overpotential as well as the electrolyte conductivity. For both electrodes, the activation overpotential is calculated using $\eta = \phi_s - \phi_L - E_{eq}$. Additionally, on the electrode surface the current density is described as a function of the overpotential, for example by the Butler–Volmer equation (ignoring the concentrations). When only considering symmetric electron transfer, i.e, $\alpha_a = \alpha_c = \alpha$, the set of equations describing this problem can be formulated as follows.

$$\left.\begin{aligned} \eta^{(k)} &= \phi_s^{(k)} - \phi_l^{(k)} - E_{eq}^{(k)} \\ i_{loc}^{(k)} &= \vec{i}_l^{(k)} \cdot \vec{n}^{(k)} = 2\, i_0^{(k)} \sinh\left(\frac{\alpha F \eta^{(k)}}{RT}\right) \end{aligned}\right\} \text{both electrodes } (k = R, L)$$

$$\left. i_l = -\sigma_l \frac{\phi_l^R - \phi_l^L}{d} \right\} \text{Ohm's law}$$

The upper index denotes the electrode position, e.g., ϕ_l^R is the liquid potential at the right electrode and the index i can either be R or L for the right or left electrode, respectively. For each of the electrodes, the local current density i_{loc}^k given by the Butler–Volmer equation is set

to the scalar product of the liquid current density and surface normal vectors $\vec{n}^k$, which have opposite orientation ($\vec{n}^L = -1$ and $\vec{n}^R = 1$). Since the current density is constant everywhere in a one-dimensional model, one can rearrange the equations above into

$$\sigma_l \frac{\phi_l^R - \phi_l^L}{d} = 2\, i_0^L \sinh\left[\left(\frac{\alpha F}{RT}\right) \underbrace{\left(\phi_s^L - \phi_l^L - E_{eq}^L\right)}_{\eta^L}\right] \quad \longrightarrow \quad \text{left electrode,} \tag{3.6}$$

and

$$\sigma_l \frac{\phi_l^R - \phi_l^L}{d} = -2\, i_0^R \sinh\left[\left(\frac{\alpha F}{RT}\right) \underbrace{\left(\phi_s^R - \phi_l^R - E_{eq}^R\right)}_{\eta^R}\right] \quad \longrightarrow \quad \text{right electrode.} \tag{3.7}$$

The current densities at the electrodes have opposite sign which means that all charge entering one electrode must exit the other one (conservation of current). Subtracting Eqs. (3.6) and (3.7) yields

$$2\, i_0^L \sinh\left[\left(\frac{\alpha F}{RT}\right) \underbrace{\left(\phi_s^L - \phi_l^L - E_{eq}^L\right)}_{\eta^L}\right] = 2\, i_0^R \sinh\left[-\left(\frac{\alpha F}{RT}\right) \underbrace{\left(\phi_s^R - \phi_l^R - E_{eq}^R\right)}_{\eta^R}\right]. \tag{3.8}$$

For simplicity, we will focus only on the case where the exchange current densities i_0^L and i_0^R for both electrode surfaces are equal ($i_0^R = i_0^L = i_0$). Therefore, Eq. (3.8) yields

$$-\underbrace{\left(\phi_s^R - \phi_l^R - E_{eq}^R\right)}_{\eta^R} = \underbrace{\phi_s^L - \phi_l^L - E_{eq}^L}_{\eta^L}, \tag{3.9}$$

which means the overpotentials have opposite sign ($\eta^R = -\eta^L$). The only unkown variables are the liquid potentials (ϕ_l^L and ϕ_l^R). Solving Eq. (3.9) for ϕ_l^R and inserting this into Eq. (3.6) yields

$$\frac{\sigma_l}{d}\Big(\underbrace{\phi_s^L - \phi_l^L - E_{eq}^L + \phi_s^R - E_{eq}^R}_{\phi_l^R \text{ from Eq. (3.9)}} - \phi_l^L\Big) = 2\, i_0 \sinh\left[\left(\frac{\alpha F}{RT}\right) \underbrace{\left(\phi_s^L - \phi_l^L - E_{eq}^L\right)}_{\eta^L}\right], \tag{3.10}$$

which can be rearranged into

$$\phi_s^L - E_{eq}^L + \phi_s^R - E_{eq}^R - 2\phi_l^L = \frac{2\, i_0\, d}{\sigma_l} \sinh\left[\left(\frac{\alpha F}{RT}\right)\left(\phi_s^L - \phi_l^L - E_{eq}^L\right)\right]. \tag{3.11}$$

Solving Eq. (3.9) for ϕ_l^R and inserting this expression into Eq. (3.6) was an arbitrary choice. A different approach which yields the same result would be solving Eq. (3.9) for ϕ_l^L instead of ϕ_l^R and inserting the obtained expression into either Eq. (3.6) or (3.7). Equation (3.11) represents a transcendental equation which has no analytical solution and can therefore only be solved numerically. The only unkown variable in this equation is the liquid potential at the left electrode (ϕ_l^L). From the obtained value of ϕ_l^L, all remaining properties (ϕ_l^R, i_l, etc.) can be calculated Solutions of the transcendental Eq. (3.11) compared to solutions from COMSOL Multiphysics simulations will be discussed hereinafter. If not stated otherwise the following parameters are used: $\alpha = 0.5$, $d = 0.01\,\mathrm{m}$, $\sigma_l = 10\,\mathrm{S\,m^{-1}}$, $T = 293.15\,\mathrm{K}$, $i_0 = 100\,\mathrm{A\,m^{-2}}$, $\phi_s^R - \phi_s^L = 2\,\mathrm{V}$, $E_{eq}^R = 2\,\mathrm{V}$ and $E_{eq}^L = 3\,\mathrm{V}$.

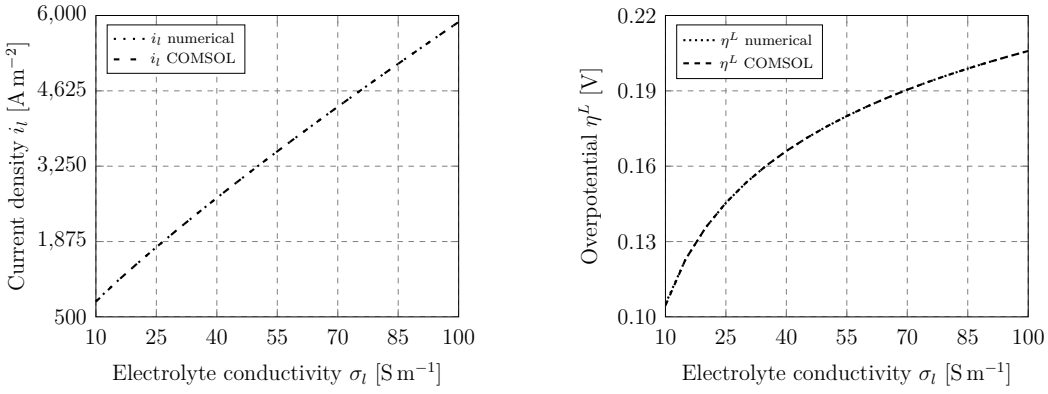

Figure 3.17: **Current density and overpotential: COMSOL vs. numerical solution**. Solutions of Eq. (3.11) and results from COMSOL Multiphysics simulations with the same set values[6] yielding the parameters i_l and η^L are shown in (a) and (b), respectively.

Solutions from Eq. (3.11) agree well with COMSOL Multiphysics simulations, as shown in Fig. 3.17.

3.4.2 Three-Dimensional Model

In this section, simulations using the three-dimensional model as described in Sec. 3.1 will be discussed. In these simulations a concentration-independent Butler–Volmer equation (2.28) was applied at both electrode surfaces. The CE was set to ground and the potential at the WE was changed according to the function shown in Fig. 3.18.

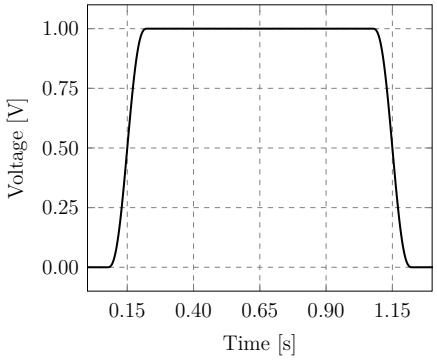

Figure 3.18: **Shape of the applied potential pulse at the working electrode**. This figure shows the voltage pulse which is applied at the working electrode (WE) during the simulations utilising electrochemistry. The potential at the WE (the electrode potential ϕ_s) was set to the open-circuit potential (OCV) plus the pulse as depicted in this figure.

[6] Electrolyte conductivity σ_l was varied in steps of 5 S m^{-1}. While Eq. (3.11) was solved with highest (machine) precision, results from a COMSOL Multiphysics simulation depend on the resolution of the spatial grid (mesh) as well as the set value at which the solver stops computing. For the mesh, the distance A between the electrodes was divided into 100 parts of equal length and the solver was set to a relative tolerance of 10^{-6}.

This means, the potential in the solid at the electrode surface (the electrode potential ϕ_s) was a time-dependent quantity. Before and after the pulse, the open-circuit voltage was applied, i.e., the current was zero. When performing a potential step experiment it is important to know the potential at which no reaction arises. This value where zero current flows through the cell is called open-circuit voltage (OCV). Without current flowing, no reaction happens and no concentration influx happens either. Only when the potential step is being applied a concentration influx occurs and this is the desired mode of operation for this experiment. It is possible to calculate the OCV from the equilibrium potentials: $E_{eq,WE} - E_{eq,CE} = -0.668\,\mathrm{V}$ (see Table 3.1). Using simulations this value was verified.

The pressure difference between inlet and outlet was set to 1 Pa. These simulations resolve the local current density at the electrode surfaces but they do not resolve effects caused by concentration (Nernst equation). This means, the concentration overpotential is not considered. To account for the concentration influx at the working electrode, an electrode surface coupling was applied at the working electrode surface which sets the flux $\boldsymbol{N}_i$ in each spatial point of the mesh depending on the local current density $\boldsymbol{i}_{loc}$ according to

$$\boldsymbol{N}_i = \sum_m \frac{v_{i,m}\,\boldsymbol{i}_{loc}}{n_m\,F}. \tag{3.12}$$

The constant $v_{i,m}$ is the stoichiometric coefficient, n_m the number of electrons involved in the faradaic process and F is Faraday's constant. For the considered electrode material being copper, $v_{i,m}$ and n_m were set to one and minus one, respectively. The other electrochemical parameters used are given in Table 3.1.

3.4.2.1 Current Density on the Working Electrode

Utilising the obtained OCV and a pulse exceeding the OCV by 1 V, a time-dependent simulation was performed. For this simulation the applied voltage at the working electrode (the electrode potential potential ϕ_s) was set to the sum of the OCV and the pulse which is shown in Fig. 3.18. From this simulation, the local current density on the working electrode was extracted which will be discussed following. The distribution of the local current density is important since it governs the rate of species influx. Figure 3.19 shows the normal current density on the working electrode surface. This means, it depicts the current flowing perpendicular to the surface.

Across the working electrode, the current density is not uniform since it depends on the electrode positions. The highest absolute values of the current density occur adjacent to sides where the counter electrode protrudes, i.e., at x = ±2 mm, as can be seen in Fig. 3.19a. All current flowing at the sides where the counter electrode overlaps the working electrode takes the shortest path, hence, the peaks in current density on the working electrode surface. The trend of the working electrode having extreme values of current density on its boundaries as shown in Figs. 3.19b and 3.20 can for example be found in [52–54]. It is important to evaluate the current density close to the edges of the WE (x = ±2 mm) to resolve the trend of its values at these positions properly. While the current density changes at the beginning and end of the applied potential square pulse, the main contribution of the flow of current is where the applied potential has its maximum. Hence, the visualisation in Fig. 3.19 for a simulation time of 0.65 s which is in the middle of the applied potential pulse. The local gradient of the current density over the working electrode can be seen in Fig. 3.19b. The current density

takes values of around $-2.75\,\mathrm{A\,cm^{-2}}$ and $-0.51\,\mathrm{A\,cm^{-2}}$ at the edge (in x) and the centre, respectively, yielding a change by a factor of five.

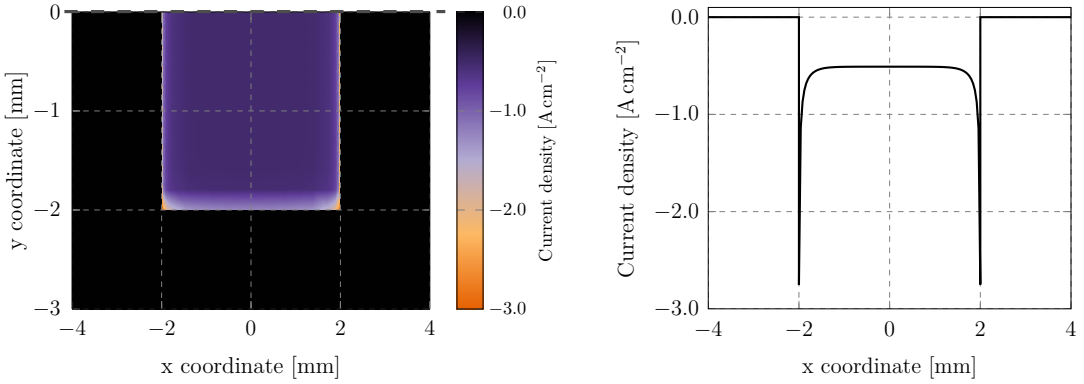

Figure 3.19: **Current density on the working electrode (contour plot and line evaluation)**. For a simulation time of 0.65 s, (a) shows the current density on the surface on which the working electrode is positioned and (b) a line plot of the current density in the centre of the working electrode (at y = 0). The utilised mesh was generated using $p = 0.95$. (a) shows half of the spatial data indicated by the dashed symmetry line.

Since the current density over the working electrode is not uniform, the influx of species will not be uniform either.

Mesh Refinement

The distribution of the current density across the working electrode changes drastically with peaks at the boundaries. Hence, it is expected that the current density distribution across the working electrode depends to a certain extent on the chosen mesh quality which is shown in Fig. 3.20.

Equations in COMSOL Multiphysics are solved on a finite discretised spatial grid, and on each of this grid point polynomials are defined which are called shape functions and their order is named or element order. The final results are then interpolated between these functions. Hence, using a higher element order increases the accuracy of simulations results but also adds a significant amount to the total simulation time. Another option is to refine the generated mesh locally which was done by a refinement in two small volumes defined by $x \in [\pm 1.8, \pm 2.2], y \in [-2, 2]$ and $z \in [0, 0.025]$ around the working electrode edges in units of millimetres. In these two volumes the mesh was subdivided by a total number of two times.

The extrema of the normal electrolyte current density at the edges of the WE (x = ± 2 mm) are better resolved for the optimised geometry which can be seen in Figs. 3.20a and 3.20c. By using quadratic mesh elements the detail of the simulation results in these areas can be improved additionally. To quantify the level of accuracy depending on the geometry and used mesh element order, the data shown in Fig. 3.20 was integrated numerically which is shown in Fig. 3.21.

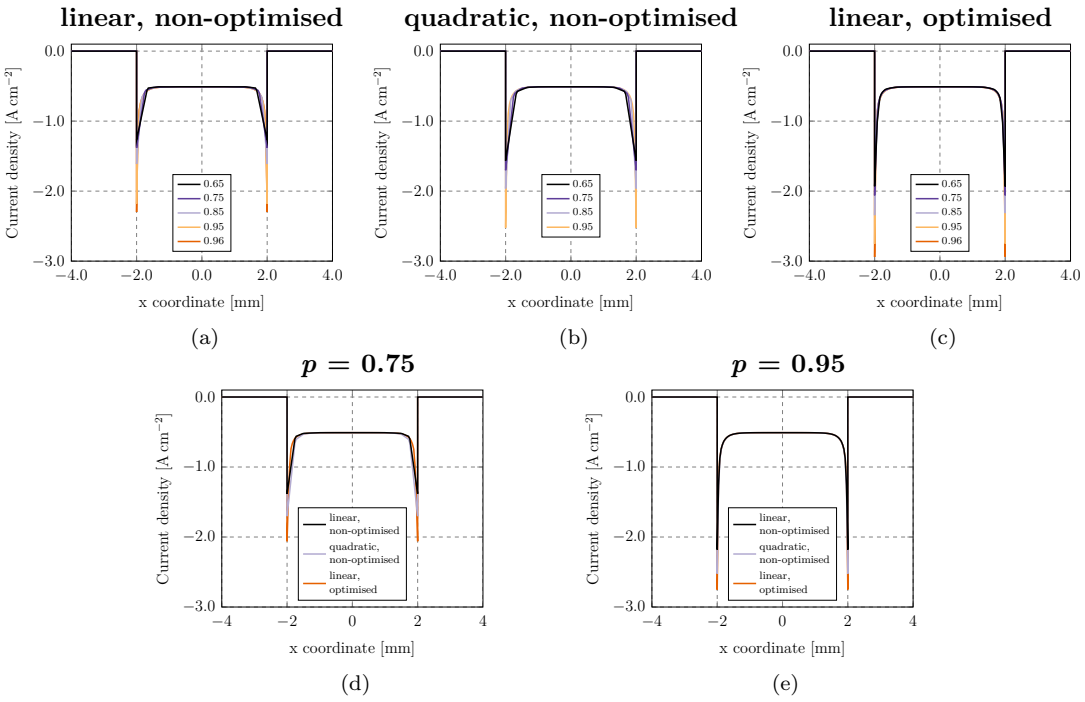

Figure 3.20: **Current density on the WE for different geometries and element orders**. This figure shows the line profile of the normal current density on the WE at t = 0.65 s in the centre, i.e., at y = z = 0. (a) shows linear element orders with a non-optimised geometry, (b) shows results using the non-optimised geometry with quadratic element order and (c) linear element orders using an optimised geometry. The legend indicates the used mesh quality parameter p. The figures in the second row show the current density for the different geometries and element orders for two different meshes ($p = 0.75$ and 0.95). See text for details.

The differences for low-quality meshes are more significant than for meshes with a higher quality, as can be seen from Fig. 3.21.

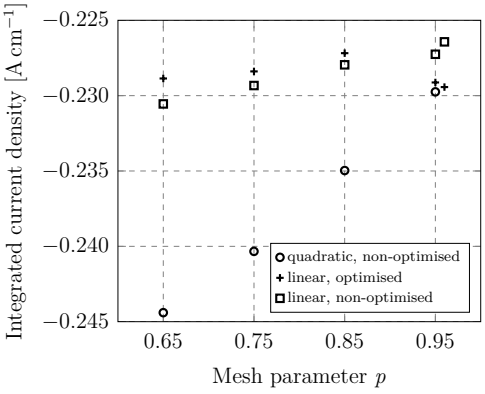

Figure 3.21: **Integration of the current density for different geometries and element orders.** Depending on the geometry and element order this figure shows the line integration of the data shown in Fig. 3.20.

Since there is no significant gain in accuracy of simulation results, a refined mesh at the electrode edges combined with linear order mesh elements and a mesh quality of $p = 0.95$ was chosen for simulations utilising concentration-independent kinetics. The reason for using the optimised mesh is due to the higher accuracy in simulation results directly at the electrode edges (x = ±2 mm). While there is no significant gain in accuracy for different mesh element types and meshes, the mesh refinement as described in this section gives a general idea what can be done to investigate simulation results depending on the mesh. The results presented above show that the optimisation of the geometry and changing of the element orders yield different results in the accuracy of the simulations. For this considered problem, optimising (refining) the mesh is superior compared to employing higher-order mesh elements combined with an unoptimised mesh. Depending on mesh quality and the used element order, simulations may be more or less demanding with regard to, e.g., needed physical memory which is shown in Fig. 3.22.

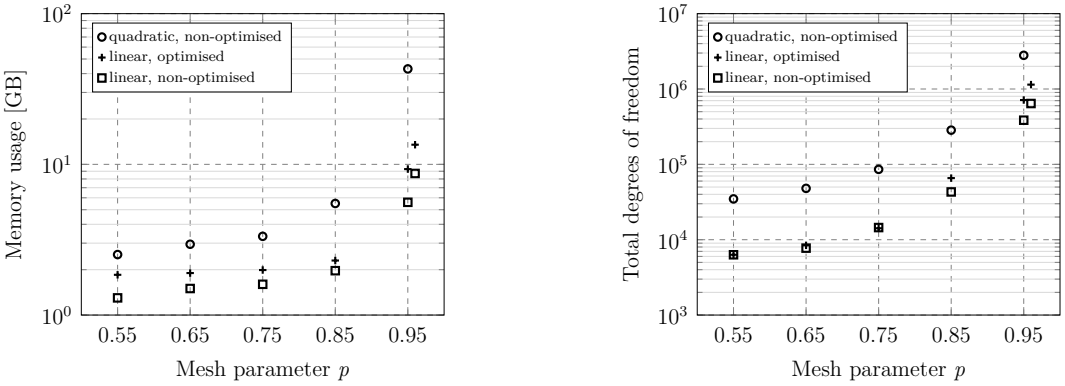

Figure 3.22: **Degrees of freedom and memory usage during simulations**. Runtime information for the simulations depending on mesh and element order. (a) shows the peak-memory usage and (b) the number of total degrees of freedom (total DOF) during the respective simulation. No simulations were performed using a mesh quality of 0.96 in combination with quadratic elements due to memory constraints. These simulations were performed using electrochemistry only (neither fluid flow nor diffusion was considered).

The three main factors influencing the memory usage and DOF are the quality of the mesh, the employed element order and the utilised physics in COMSOL Multiphysics. While the first two define the spatial resolution of the simulation, the latter one defines how many dependent variables are defined in each spatial point which is presented in Table 3.3.

Table 3.3: **Dependent variables depending on the used COMSOL Multiphysics module**. For the three physics modules *laminar flow*, *transport of diluted species* and *electrochemistry* the second column lists the respective dependent variables and the third column the total number of dependent variables for each module.

Physics module	Dependent variables	Number of dependent variables
Laminar flow	Velocity $\boldsymbol{u}(u, v, w)$ Pressure p	4
Transport of diluted species	Concentration c	1
Electrochemistry	Liquid potential ϕ_l	1

For the values given in Table 3.3 it is assumed that only one species occurs in the module *transport of diluted species*, hence only one dependent variable for these two modules. The modules solve for these dependent variables and all desired quantities are calculated from them. For example the viscous stress tensor is calculated [27, p.182] using $\sigma = \mu(\nabla \boldsymbol{u} + (\nabla \boldsymbol{u})^T)$, the concentration diffusive flux via the gradient of the concentration [28, p.121] and the current through the electrolyte is calculated via Ohm's law [19, p.104; 29]. The number of total degrees of freedom is given by [55]

$$(\#\text{degrees of freedom}) = (\#\text{nodes}) * (\#\text{dependent variables}). \tag{3.13}$$

The number of nodes (#nodes) depends on the mesh element type and the used element order (linear, quadratic, cubic, etc). For example when using linear element orders with hexahedral elements the number of nodes is given by (#nodes) = 1.2 * (#elements), with (#elements) being the number of used elements (hexahedra). Using quadratic element orders the multiplication factor is 8.5 instead of 1.2 [55]. The simulations whose results are shown in Fig. 3.22 were done using the *electrochemistry* module solely in combination with a hexahedral mesh. The amount of dependent variables in this case is one and by using Eq. (3.13) the degrees of freedom (DOF) can be estimated. The total amount of DOF is proportional to the mesh elements (cf. Figs. 3.3 and 3.22). Using this information the amount of DOF depending on the utilised mesh, used element orders as well as the employed physics can be estimated. It is important to note that up to now all considerations regarding the current density were considered at a time of 0.65 s for a location in the centre of the electrodes. Motivation for this was the fact that the main impact of the total cell current has its maximum during the plateau of the applied pulse (see Fig. 3.18). Additionally, the current density on the electrode surface is quite homogeneous with respect to the y coordinate, which can be seen in Figs. 3.19a and 3.24a. During the onset and ending of the applied pulse, solutions in the current density may be dependent on the chosen mesh. This is shown in Fig. 3.23.

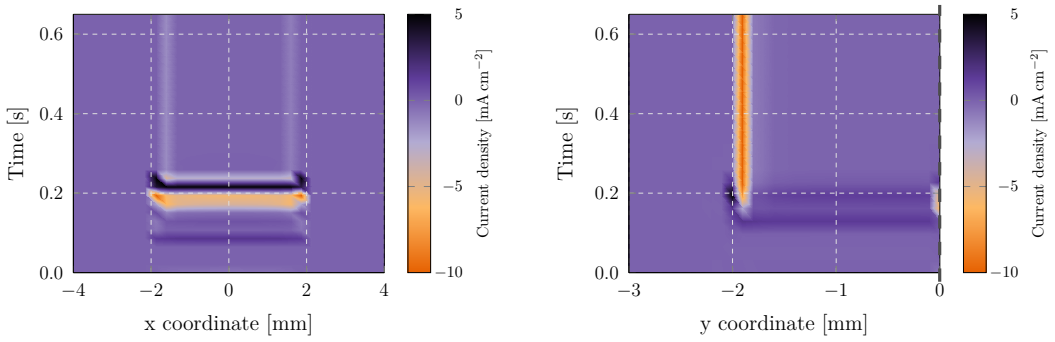

Figure 3.23: **Time-dependent convergence of the current density on the working electrode**. Simulations using a mesh quality of $p = 0.95$ and 0.96 were performed. Both figures show the time dependent difference of the current density between these two meshes, i.e., both show the difference $p_{0.96} - p_{0.95}$. For times greater than 0.65 s both figures show a symmetric behaviour in time due to the symmetry of the applied voltage pulse. While (a) shows a line profile at y = 0, (b) shows a line evaluation at x = 0. Please note that (b) shows only one half of the spatial data indicated by the dashed symmetry line.

Differences emerge when the applied potential at the WE changes and current flows ($t > 0.15$ s). These differences are greatest at the boundaries of the working electrode (y = ± 2 mm) and during the time where the applied pulse changes most ($t \in [0.075\,\text{s}, 0.225\,\text{s}]$).

3.4.2.2 Current Density on the Counter Electrode

The local current density on the counter electrode is shown in Fig. 3.24. The mesh quality has no great impact on the current density at the counter electrode, as can be seen in Fig 3.24b. Similarly to the current density on the working electrode, its distribution over the counter electrode is not uniform and depends on the position of the working electrode. High values of the current density occur where the counter electrode opposes the working electrode, as can be seen in Fig. 3.24a. This can be explained with the current taking paths of least resistance, hence the main contribution of current flows at areas where these two electrodes directly oppose each other.

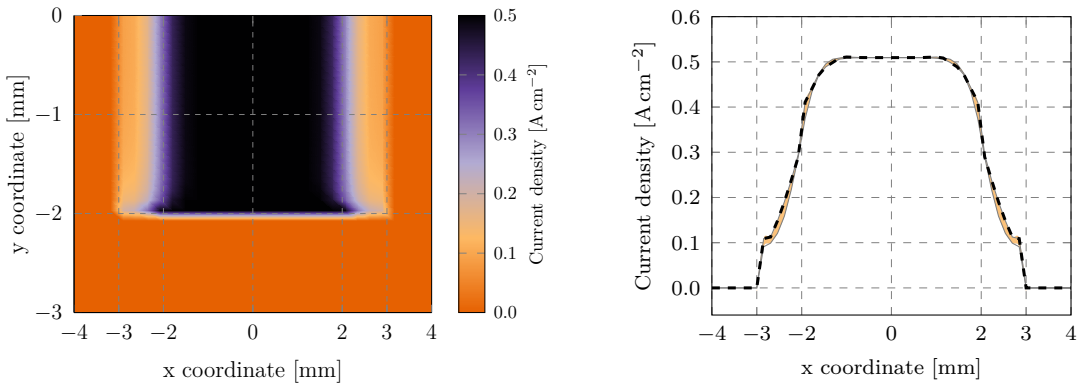

(a) (b)

Figure 3.24: **Current density on the counter electrode (contour plot and line evaluation).** (a) shows the local current density on the surface where the counter electrode is placed, i.e., at z = 0.5 mm. The plot in (b) was generated by evaluating the data from (a) across a line at y = 0 at t = 0.65 s. The electrode surface defining the counter electrode is within x = ±3 mm and y = ±2 mm. The highlighted area in (b) marks the enveloping curves for all meshes. This means results from any simulation ranging from $p = 0.55$ to 0.96 reside in this area. The black dashed line shows the result using a parameter $p = 0.95$.

The local current density on the counter electrode does not change much depending on the quality of the mesh. Therefore, the time-dependent change of the current density will not be shown.

3.4.2.3 Total Current

The total current flowing through the cell can be calculated by surface integrating the local current density across any of the two electrodes which is shown in Fig. 3.25. Due to conservation of charge, the same total current must flow through both electrodes at any time. Since only working electrode and counter electrode may conduct a current, any flow of current exiting the counter electrode must also enter the opposite electrode. The average current is obtained by dividing the values in Fig. 3.25 by the respective electrode surface area. While these plots are not shown, the average current density of the counter electrode is smaller than the value for the working electrode since the counter electrode has a higher surface area. This

explains why one usually designs an electrochemical cell in a way that the counter electrode has a greater surface area than the working electrode. By doing it that way, the counter electrode does not become the limiting factor with regard to the electrode kinetics. This ensures probing the working electrode which is the surface of interest one wants to study.

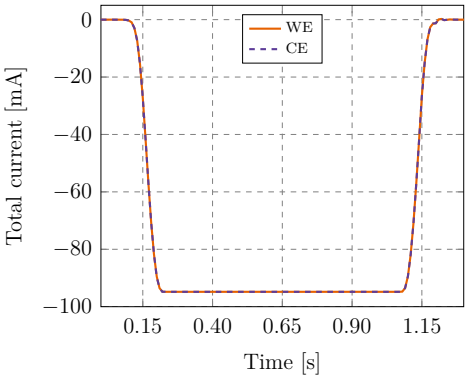

Figure 3.25: **Total current versus time on both electrodes**. This figure shows the total current in the cell at any point in time, obtained by integrating the normal electrolyte current density over both electrode surfaces. This means, they the show the magnitude of current flowing through the working electrode and counter electrode. For times greater than shown here, the total current in the cell is zero. For visualisation purposes, the current values at the counter electrode were multiplied by a constant factor of minus one.

Due to the exchange current density having a significant impact on the Butler–Volmer equation, its value plays an important role in that regard (see Fig. 2.4).

3.4.2.4 Liquid Potential and Overpotential

In simulations the electrolyte potential, which is shown in Fig. 3.26, governs the current flowing through the cell as described by Ohm's law.

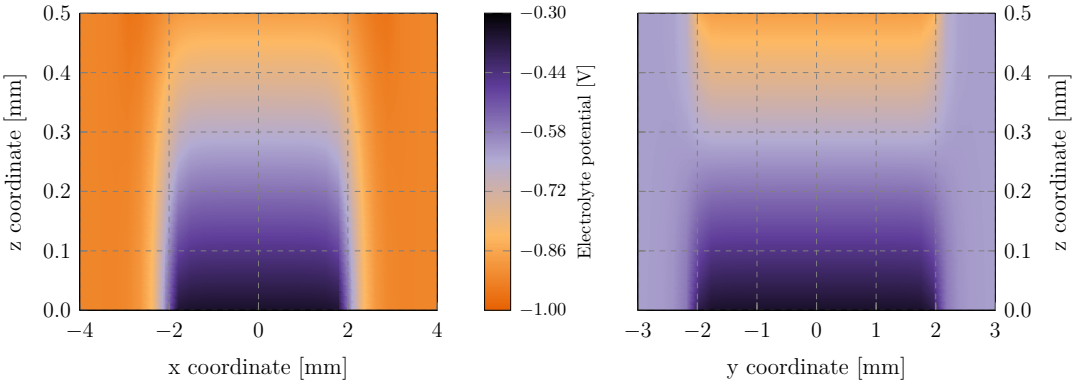

(a) (b)

Figure 3.26: **Contour plot of the electrolyte potential in the cell**. At t = 0.65 s, (a) shows the electrolyte potential in the centre of the cell, i.e., at y = 0, and (b) depicts the electrolyte potential on a yz slice at the centre of the cell at x = 0. The colour bar in the middle applies to both plots.

The electrolyte potential in the liquid drops linearly between working- and counter electrode due to the assumption of the electrolyte having isotropic electric conductivity which yields a constant current gradient between both electrodes. Therefore, the current density i_l near the centre of the cell (x = y = 0) can be calculated using Ohm's law $i_l = -\sigma_l(\phi_l^1 - \phi_l^2)/d^{12}$ with ϕ_l^1 being the liquid potential at point one, ϕ_l^2 being the liquid potential at point two and d^{12} is the distance between the two considered points.

By evaluating the electrolyte potential in the centre of the electrodes, i.e., at x = y = 0, values of $-0.34\,\mathrm{V}$ and $-0.87\,\mathrm{V}$ for the electrolyte potential are obtained on the working- and counter electrode, respectively. The current density obtained by Ohm's law using an electrolyte conductivity of $4.8\,\mathrm{S\,m^{-1}}$ as well as a distance of 0.5 mm between the electrodes is $0.51\,\mathrm{A\,cm^{-2}}$, which agrees with Figs. 3.19, 3.20 and 3.24. This comparison is only possible due to the relatively high homogeneity of the electrolyte potential at the surfaces of both electrodes, as shown in Fig. 3.26. The kinetic overpotential obtained by solving the Butler–Volmer equation is shown in Fig. 3.27.

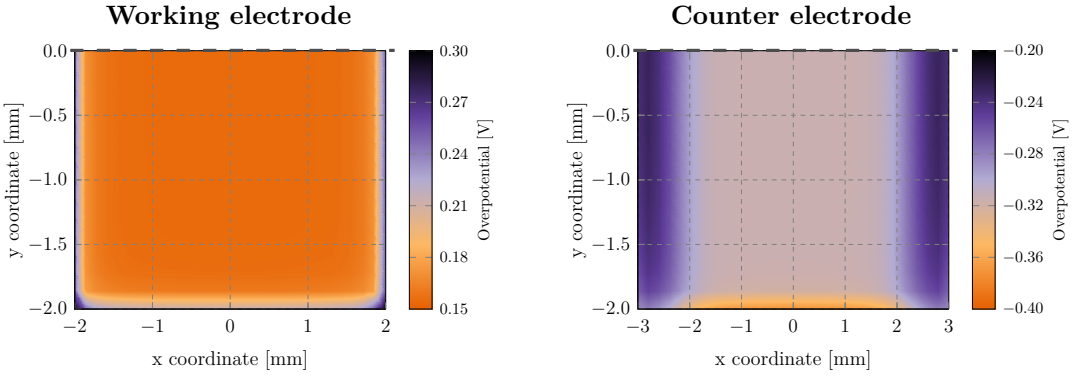

(a) (b)

Figure 3.27: **Overpotential on both electrode surfaces**. Both figures show the overpotential evaluated directly on the working electrode and counter electrode surface for (a) and (b), respectively. All values were evaluated at a time of 0.65 s. In this figure only half of the electrode surfaces is being shown indicated by the dashed symmetry line.

Since the overpotential is defined at the electrode-electrolyte interface boundary, its values are only obtainable directly at the electrode surfaces and nowhere else. When the overpotential is zero, no current flows and in that case the difference $\phi_s - \phi_l$ represents the electrode potential at equilibrium (OCV). The variable ϕ_s is the applied potential at the electrode. Therefore, the overpotential indicates how far away the system is from equilibrium. The overpotential drives the local current density on both electrodes as governed by the Butler–Volmer equation, which can be seen in Fig. 3.27. Other than at the electrode edges, the overpotential is quite homogeneous. While the overpotential on the working electrode has positive values, on the counter electrode it has the opposite sign. Due to the different sign of the overpotentials on the electrodes, the total kinetic overpotential between working electrode and counter electrode is defined as the sum of both absolute values. By calculating the surface average of the data shown in Fig. 3.27 the average overpotential for both electrode surfaces can be obtained. At a simulation time of 0.65 s the average overpotential at the CE and WE is $-0.2955\,\mathrm{V}$ and $0.1677\,\mathrm{V}$, respectively. In COMSOL Multiphysics the overpotential is calculated at both electrode surfaces using $\eta = \phi_s - \phi_l - E_{eq}$. Using this definition the average liquid potential

ϕ_l at the WE surface is given by

$$\phi_l = \overbrace{\underbrace{-0.668\,\mathrm{V}}_{\phi_s} + 1\,\mathrm{V}}^{\mathrm{OCV}} - \underbrace{0.1677\,\mathrm{V}}_{\eta} - \underbrace{0.52\,\mathrm{V}}_{E_{eq}} = -0.3557\,\mathrm{V},$$

and the average liquid potential at the CE surface is given by

$$\phi_l = \underbrace{0\,\mathrm{V}}_{\phi_s} + \underbrace{0.2955\,\mathrm{V}}_{-\eta} - \underbrace{1.188\,\mathrm{V}}_{E_{eq}} = -0.8925\,\mathrm{V}.$$

Since no concentration dependency is considered in this model these values of the liquid potential are valid for all times where the applied voltage pulse is 1 V (see Fig. 3.18).

3.4.2.5 Total Cell Integrated and Average Outlet Concentration

This section describes time-dependent simulations including the *laminar flow* module. During the simulations, the average concentration at the outlet and the total concentration depending on time was evaluated. The average concentration at the outlet depending on time is called residence time distribution (RTD). RTD curves connect the geometry of the cell to its performance and can be used for cell optimisation [56, p.867ff; 57]. Everything was done the same as for the simulations described in Sec. 3.3 but with the addition of electrochemistry. This means, species generation is caused by the local current density on the working electrode. Figure 3.28 shows these two concentrations.

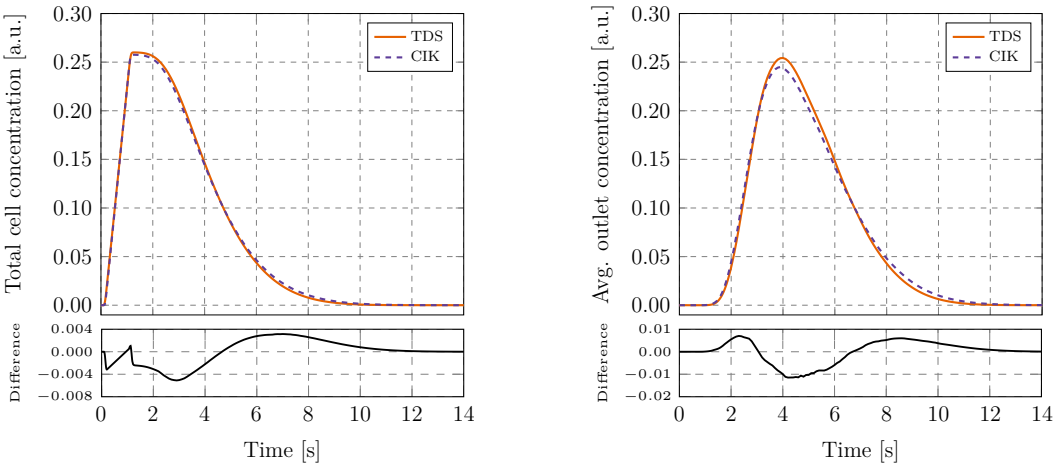

Figure 3.28: **Total cell- and average outlet concentration (TDS and CIK)**. Each of the two top figures show normalised results obtained from time-dependent simulations using a concentration influx via the *transport of diluted species* (TDS) module and concentration-independent kinetics (CIK) where the potential at the working electrode was set according to the square pulse shown in Fig. 3.18. The current was set according to a concentration-independent Butler–Volmer equation. (a) shows the normalised total concentration in the cell as a function of time and (b) the normalised average concentration at the outlet of the cell. The two small figures at the bottom show the respective difference plots, i.e., each one presents the difference between the two normalised data sets above.

When applying electrochemistry it takes more time for the generated species to be flushed out of the cell compared to simulations using the simplification of a constant concentration influx through the working electrode surface. This can be seen in Fig. 3.28b. This is due to the non-uniformity of the current density across the WE (see Fig. 3.19). Both concentrations were normalised to an area of one. The difference between simulations with and without electrochemistry can be seen easily in the difference plots at the bottom of Fig. 3.28. The local extrema in these difference plots correspond to the local current density at the WE. The species is generated at the electrode surface according to the local current density and this concentration moves through the cell. At the outlet it is then being detected. In these difference plots, three extrema are visible. These extrema get smeared out, i.e., they get broader, with time passing. The reason for that is that any concentration must first diffuse away from the electrode before it gets moved by the fluid flow. For example the last extremum in Fig. 3.28b which occurs at around 8.5 s corresponds to the concentration generated at areas of the working electrode closest to the inlet. It takes the species generated at this position longer to reach the outlet and due to diffusive broadening, this peak is smeared out more than the other two extrema. The difference between simulations with and without electrochemistry is not very large despite the non-uniformity of the current density across the working electrode. To explore this further, the surface of the working electrode was subdivided into three parts and a simulation using electrochemistry was done. Since the current density on the working electrode has two pronounced extrema, its surface was subdivided into three parts. The species generated from each of these three parts were tracked separately. Figure 3.29 shows the results of this simulation.

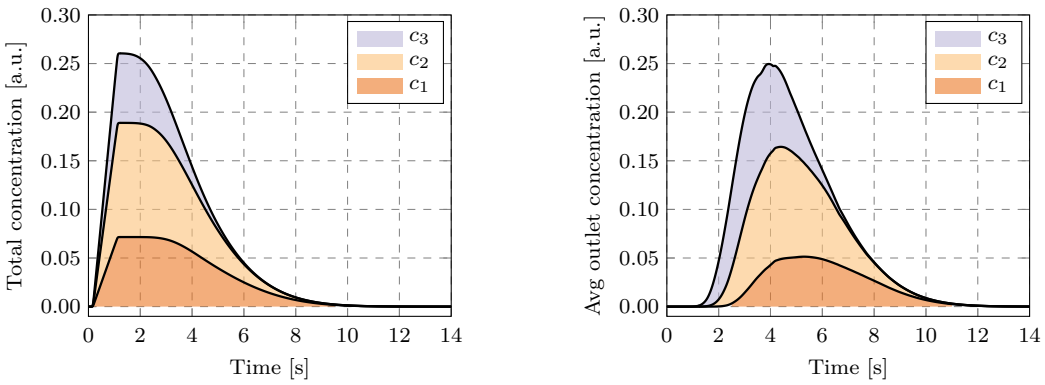

(a) (b)

Figure 3.29: **Total cell- and average outlet concentration (subdivided WE)**. The working electrode surface was split into three parts ranging from $-2 \leq x_3 \leq -1\,\text{mm}$, $-1 \leq x_2 \leq 1\,\text{mm}$ and $1 \leq x_1 \leq 2\,\text{mm}$, with the species c_3, c_2 and c_1 created in these region. Propagation of these species was tracked separately with (a) showing the normalised total cell concentrations and (b) their normalised average outlet concentrations. In both figures the cumulative normalised concentration is plotted which means the coloured difference between curves indicates the fraction of each respective species.

Splitting of the working electrode surface was done at certain x coordinates to reflect the changes in the local current density which can be seen in Fig. 3.19b. In the outermost parts, i.e., giving rise to concentrations c_1 and c_3, the current density is higher, hence, the electrochemical creation of species should also be higher due to the current density. The sum of the outer two regions has the same surface area as the single middle part. From Fig. 3.29b one can see that at the outlet concentration c_3 is detected first, followed by c_2 and c_1. This

is due to the positions of the regions with respect to the cell outlet. The maximum of the total cell concentration occurs around 1.225 s. At this point in time, the contributions of the species concentrations to the total cell concentration are 7.24 a.u., 11.49 a.u. and 7.23 a.u. for c_1, c_2 and c_3, respectively. The contributions of species c_1 and c_3 are almost the same. This is to be expected since the surface areas where these species are being generated are equal and the current density is symmetric across the working electrode (see Fig. 3.19b). By numerically integrating the current density over each split interval of the working electrode, the respective current density percentages may be obtained. As a result, around 27.5 % of the current density occurs at each of the two outer split-surfaces where species c_1 and c_3 are being generated. The respective area fractions are only 25 %. In the middle of the cell where c_2 is being generated (area fraction 50 %), i.e., at a position of x values between minus one and one millimetres, around 45 % of the local current density occurs. The ratios of generated species correspond to the ratios of current densities. Despite the lack of substantial difference between the two models, as can be seen in Fig. 3.28, one should not be tempted to substitute all electrochemistry by using a constant concentration influx over the working electrode instead. With the simplification of utilising an influx, local electrode effects like surface etching due to faradaic currents cannot be investigated. Other effects, like the impact of concentration on the current density, as described in Sec. 3.5 can not be resolved using the simplified approach which utilises a concentration pulse as a substitution of all involved electrochemistry.

Mesh Convergence Study

Both total concentration in the cell as well as the average outlet concentration depend to a certain degree on the used mesh. This is shown in Fig. 3.30.

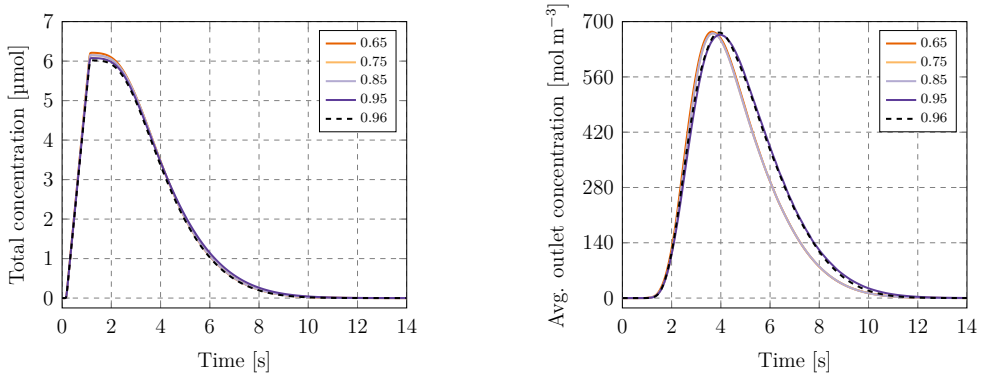

(a) (b)

Figure 3.30: **Total cell- and average outlet concentration depending on mesh quality**. For different meshes ranging from $p = 0.65$ to 0.96, simulations using a concentration-independent Butler–Volmer equation were performed. Depending on the mesh quality, (a) shows the total cell concentration and (b) the average outlet concentration.

The dependence of both average- and total cell concentration is not very sensitive to the mesh since both values average over the surface of the outlet and the total cell volume, respectively. Hence, local concentration discrepancies are not resolved in great detail. The difference in the velocity between the two meshes with the highest accuracy ($p = 0.95$ and 0.96) is less than one percent and therefore the difference in the solutions is small, as can be seen in Fig. 3.30,

which justifies the usage of a mesh with quality $p = 0.95$ for the simulations presented in this thesis. Due to the higher velocity at the outlet, concentration gets transported out of the cell faster for lower-quality meshes, as can be seen in Fig. 3.30b. For meshes with a quality lower than $p = 0.95$, the decay of concentration happens faster after the concentration reached its peak value compared to the two highest quality meshes. It is also worth noting that, similarly to the data shown in Fig. 3.20, one must not conclude that a certain mesh is sufficient in quality by judging only the difference in solutions between subsequent simulations. While simulation results with mesh qualities p between 0.65 and 0.85 do not differ greatly, there is a small but significant difference between $p = 0.85$ and 0.95.

3.4.2.6 Working Electrode Etching

COMSOL Multiphysics provides a timeint-operator which integrates any desired variable over time in each spatial point of the mesh. Since the working electrode is the electrode of interest, Fig. 3.31 shows the time integration of the normal current density $\vec{j}$ and concentration over this surface.

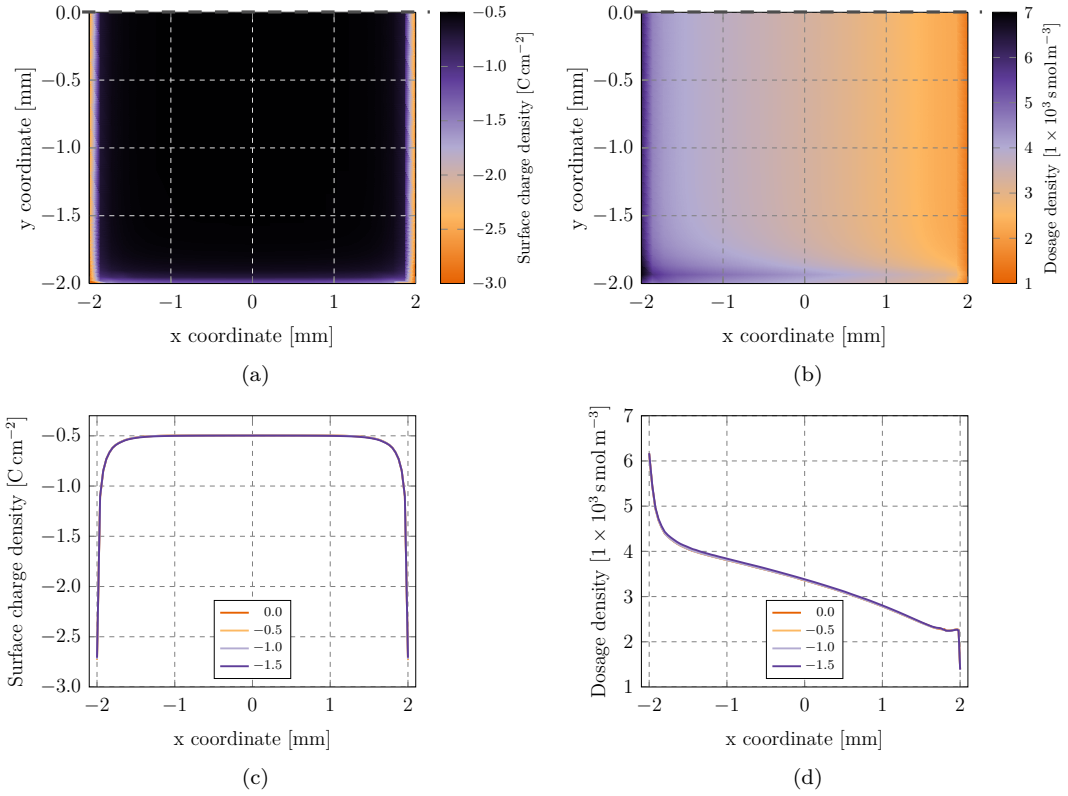

Figure 3.31: **Time integration: current density and concentration**. (a) shows the time integral of the normal current density over the working electrode for all simulation times and (b) the time-integrated concentration over the working electrode for all times. This means, the integration was performed for simulation times between zero and 14 s. Both figures (a) and (b) only show half of the spatial data indicated by the dashed symmetry line. Additionally, (c) and (d) present a line evaluation of the data shown above at different y-positions indicated in the legend. Note that the flow direction is $-x$ (right to left) in all simulations.

Mass removal from the working electrode surface can be estimated from Fig. 3.31a, which may only serve as a worst or best case depending whether one is interested in preserving or etching of the surface. The reason for this is that the current flow is assumed to happen only by means of faradaic reactions. Thus, the mass removal is proportional to the local current density over the electrode surface.

Due to the almost homogeneous current density distribution in most parts of the WE, the influx of species occurs quite uniformly over much of the working electrode surface. Therefore, the time integration of the concentration shows a roughly linear decrease over the surface from inlet to outlet, as can be seen in Fig. 3.31b. From this figure one can also get a feeling what may change when applying concentration-dependent electrode kinetics. The presence of reaction products counteracts the current density, hence, one can assume that the current density at the outlet side to be smaller than on the inlet side, since over the whole simulation time the surface closer to the outlet is being exposed to a higher concentration of products.

3.4.2.7 Mass Transport in the Cell

Concentration can be evaluated in any point of space and time from simulations. Figure. 3.32a shows data directly obtained from COMSOL Multiphysics, i.e., it shows the concentration in the cell at t = 2 s. From this scalar field isolines can be extracted which enclose a certain percentage of concentration. Figure 3.32b shows the extracted isolines for eight different simulation time steps. To generate the isolines, the scalar concentration field was evaluated on a plane and from this data the isolines were extracted.

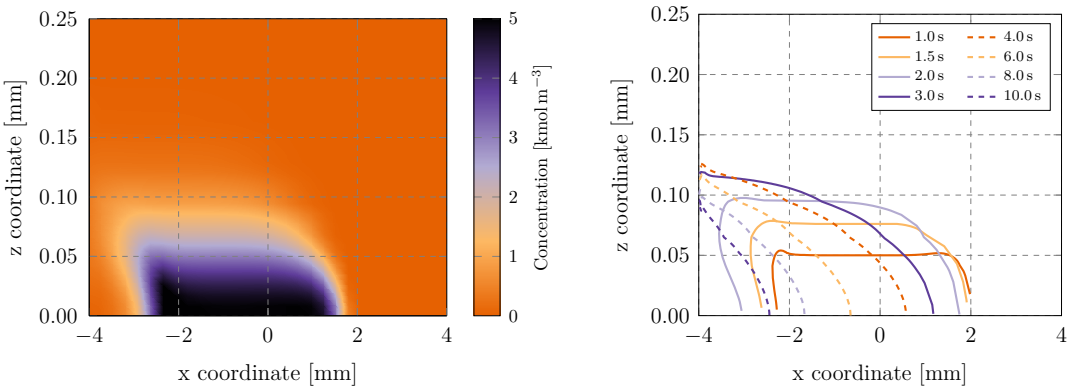

(a) (b)

Figure 3.32: **Concentration slice and extracted isolines for a selection of times**. For a time-dependent study as described above, (a) shows the concentration in a centre xz plane of the cell at t = 2 s extracted from COMSOL Multiphysics. (b) shows 90 % isolines of concentration for a selection of times extracted from simulation results, as shown exemplarily in (a) for t = 2 s. This means, at any given time the corresponding lines in (b) enclose 90 % of the concentration evaluated on a slice in the centre of the cell (at y = 0).

Additional information about the mass transport due to flow and diffusion can be found in Sec. 3.3.1.

3.5 Electrochemistry with Concentration-Dependent Current (CDK)

In this section, results obtained from simulations using concentration-dependent kinetics will be discussed and presented. These simulations are harder to compute than ones without concentration-dependent kinetics since they require a finer mesh. This attention towards the mesh is important since the concentration directly exerts a feedback on the current density as described in Sec. 2.2.2.4. Therefore a mesh with a high quality at the vicinity of the electrode surface is necessary to resolve diffusion processes happening there. Hence, without proper mesh quality there may occur rather large jumps in the current density during simulations and in the worst case the simulation does not compute at all. Best convergence with regard to the solver settings for the time-dependent step has been achieved by using a fully coupled solver with the nonlinear method set to automatic (Newton), an increased minimum damping factor, as well as the maximum number of iterations increased to 250. Additionally, by using concentration-dependent kinetics (CDK), a finer mesh may speed up the simulation despite the increased number of degrees of freedom (DOFs) solved for since the solver converges better due to the larger time steps in the finer mesh compared to the coarser mesh. This means, since during a time-dependent study the equations are solved in discretised time steps, increasing the mesh quality may result in the solver taking larger time steps which is much faster than the case where the time steps are very small (for the coarser mesh). Hence, a finer mesh may result in a faster computatitional time which seems counterintuitive at first. In all previous simulations which utilise electrochemistry and are presented in Sec. 3.4, concentration dependence was not considered. The rate of concentration-influx was governed by the local current density but the generated species did not affect the current density. The current density changes as the voltage applied by the pulse rises and falls, but while the voltage is at its maximum value (see Fig. 3.18), the current density at the electrode does not change. The simulated electrochemical reaction was dissolution of solid copper through an applied voltage pulse. An overview of this set-up, including the reactions assumed to happen at the electrode surfaces, is shown in Fig. 3.33.

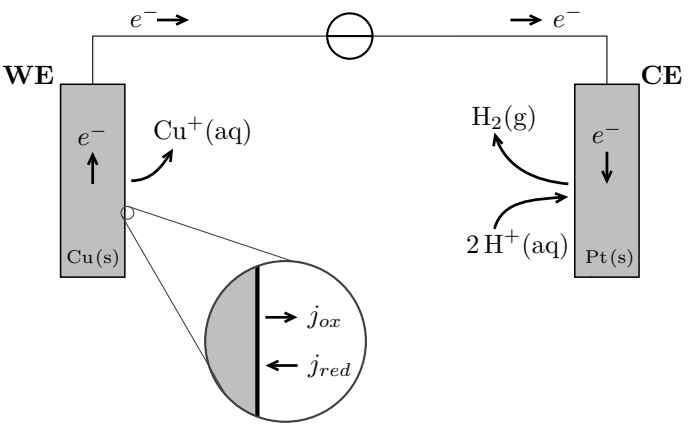

Figure 3.33: **Overview of the electrochemical system including the participating reactions.** Due to the applied voltage between working electrode (WE) and counter electrode (CE) faradaic reactions happen at both electrode surfaces. In addition to the reactions occuring at these surfaces, the contributions of oxidising current (j_{ox}) and reducing current (j_{red}) occuring at the WE are depicted.

All simulations involving concentration-dependent kinetics were performed with the Butler–Volmer equation on both electrode surfaces. Since the WE is the surface of interest and additionally to keep the model as simple as possible only on the WE surface was subject to concentration dependency. This means, on the WE the kinetics were simulated using Eq. (2.31) while at the surface of the CE Eq. (2.28) was applied. Due to the applied voltage pulse oxidation happens at the WE, i.e., solid copper loses an electron and is emitted into the liquid as an ion. On the cathode (CE) reduction happens which means hydrogen ions are assumed to be catalysed to hydrogen gas at the platinum surface. The Butler–Volmer equation describes the current density as a sum of anodic and cathodic currents (see Sec. 2.2.2.1) which is illustrated in Fig. 3.33 for the WE surface. This means, depending on the sign of the overpotential an anodic or cathodic net current occurs at the electrode. At equilibrium both partial currents cancel each other out and the electrode surface is in an (dynamic) equilibrium. For example in the considered system as described above at the WE these partial currents are given by

$$j_{ox} : \mathrm{Cu(s)} \rightarrow \mathrm{e^-} + \mathrm{Cu^+(aq)},$$

and

$$j_{red} : \mathrm{e^-} + \mathrm{Cu^+(aq)} \rightarrow \mathrm{Cu(s)}.$$

At the WE surface the concentration-dependent Butler–Volmer equation which is given by Eq. (2.31) usually depends on the local concentration of reduced species C_R, oxidised species C_O as well as their reference concentrations C_R^* and C_O^*. The local concentrations are the respective values directly at the electrode surface and the bulk concentrations are the values of the concentration away from the electrode surfaces. The used variables depending on the physics module in COMSOL Multiphysics are listed in Table 3.4.

Table 3.4: **Variables used for concentration species depending on the used physics module**. For both physics modules *transport of diluted species* and *electrochemistry* this table lists the variables for oxidising species C_O and reducing species C_R.

COMSOL Multiphysics module	Variable	Description
Transport of diluted species	$C_{O,init}$	Initial concentration for species C_O
	$C_{R,init}$	Initial concentration for species C_R
Electrochemistry	C_O^*	Bulk concentration for species C_O
	C_R^*	Bulk concentration for species C_R

The initial concentrations $C_{O,init}$ and $C_{R,init}$ are used as initial values set in the module *transport of diluted species*. This means, at the beginning of the simulation the concentrations C_O and C_R are set to the values of $C_{O,init}$ and $C_{R,init}$, respectively. Additionally, at the inlet these two initial concentrations are set as a concentration boundary so that any inflow of concentration has the respective concentration according to the set initial values. The bulk concentrations C_R^* and C_O^* only apply to the *electrochemistry* module where they are utilised in the concentration-dependent Butler–Volmer equation (2.31). In the *transport of diluted species* module the two dependent variables which are solved for during a simulation are the concentrations C_O and C_R. This means, initially these two concentrations are set to their initial values and due to electrochemistry they are transformed into each other. Since the Butler–Volmer equation describes a redox reaction ($\mathrm{Ox} + \mathrm{ne^-} \rightleftharpoons \mathrm{Red}$) any increase of C_O

must yield an decrease of the same amount of C_R and vice versa. In the current case (etching of Cu), the reduced species (Cu^0) are in the electrode, not in the electrolyte. Therefore, the C_R/C_R^* fraction in the concentration-dependent Butler–Volmer equation was set to unity at all times [58], therefore the C_R values in the electrolyte are not used in the present simulations. Hence, the concentration C_R acts as an infinite reservoir and the generation of copper ions is not limited. At the start of the simulation no copper ions are present in the electrolyte, i.e., the concentration C_O is zero. To ensure computation the concentration $C_{O,init}$ was set to eps mol m^{-3} with eps $= 2.2204 \times 10^{-16}$. All other concentrations ($C_{R,init}, C_R^*$ and C_O^*) were set to 1000 mol m^{-3} [58]. This means, the value of the open-circuit voltage (OCV) is given for these concentration. In the simulation the concentration C_R represents the solid copper (the WE) which should always be available for a reaction at the WE surface. Hence, the term C_R/C_R^* in the concentration-dependent Butler–Volmer equation was set to one at all times [58]. All other parameters used for the simulations were set the same as before for simulations using concentration-independent kinetics (see Table 3.1).

3.5.1 One-Dimensional Model

To gain a better understanding of electrochemistry involving concentration-dependent electrode kinetics simulations using a simple one-dimensional model were performed. To keep the geometry as close to the three-dimensional model, the two electrodes were separated by a distance of 0.5 mm which is the same distance as the one used in previous simulations. The considered model is depicted in Fig. 3.34.

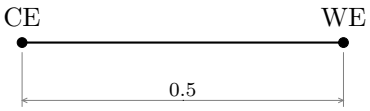

Figure 3.34: **Geometry of the one-dimensional model**. In this one-dimensional model the working electrode (WE) and counter electrode (CE) are separated by a distance of 0.5 mm.

To generate the mesh of this model the distance between WE and CE was divided into 1000 equal parts. All parameters were set as described previously but no fluid flow was considered. In the three-dimensional model, fluid flows perpendicular to the direction between WE and CE which is not feasible in a one-dimensional model. The beginning of the applied voltage pulse was shifted one second in time to resolve effects preceding the pulse. The electrode potential (ϕ_s) at the WE was set according to OCV+pulse(t) where OCV is the open circuit voltage (−0.668 V) of the cell with a Cu^+ concentration of 1000 mol m^{-3} and pulse(t) is the voltage pulse as shown in Fig. 3.35.[7]

[7] This is not the OCV at the initial concentration; see the discussion on page 58.

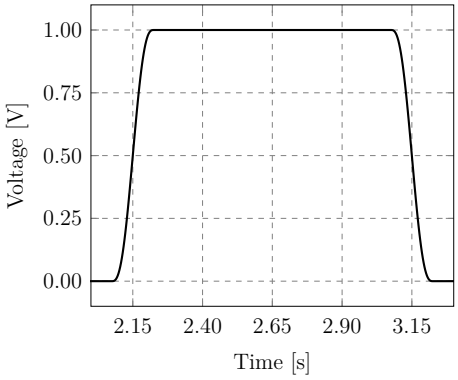

Figure 3.35: **Shape of the applied potential at the working electrode**. This figure shows the voltage pulse which is applied at the working electrode (WE) during simulations which utilise concentration dependent kinetics (CDK) in studies concerning the one-dimensional model. The shape is defined by the lower limit, upper limit and the size of transition zone, which were set to 2.15, 3.15 and 0.15, respectively.

Simulations with these settings were performed which will be discussed and presented following. Figure 3.36 shows the concentrations C_O and C_R, the overpotential at the WE and the current density for the one-dimensional model. Two different kind of simulations were performed for an infinite reservoir ($C_R/C_R^* = 1$) and for a finite reservoir in which this fraction was not set to one.

When the factor C_R/C_R^* is set to one, independent of the actual C_R value (to simulate an infinite reservoir of Cu) the concentration C_R of Cu^0 can reach arbitrary (negative) values. For simulations in which C_R in the electrolyte is considered as a reactant (limited current), the concentration C_R can not reach negative values. The time-dependent behaviour of the concentrations C_O and C_R goes as follows. At the beginning the system is at its initial point, i.e., the respective initial concentrations are set ($C_{O,init}$ and $C_{R,init}$). Before the applied pulse ($t < 2\,s$) the concentration of C_O is smaller than the equilibrium concentration ($1\,kmol\,m^{-3}$) which means during this time oxidation of Cu^0 happens and C_O increases to $\approx 0.05\,kmol\,m^{-3}$ until $t = 2\,s$. C_R decreases by the same amount which has no substantial effect, irrespective of whether its value is taken into account or not. During the applied voltage pulse ($2 < t < 3\,s$) the concentrations C_O and C_R change substantially, as governed by the Butler–Volmer equation. The principle of equivalent change of oxidising and reducing species an be seen here clearly since any change in C_O results in an equal but opposite change in concentration C_R. In case of the unlimited current ($C_R/C_R^* = 1$) the concentration C_R reaches negative values since its contributions in the Butler–Volmer equation is suppressed, i.e., C_R/C_R^* is set to one. When this factor is considered (limited current, Fig. 3.36b), the oxidised species C_O reaches its maximum at $1\,kmol\,m^{-3}$ which is the initial value for the species C_R ($C_{R,init}$). Since for the case of the limited current ($C_R/C_R^* \neq 1$) the concentration C_R can not go below zero, the amount of C_O is limited by the C_R initially present. Therefore, the current decreases in that case during the applied voltage pulse.

After the pulse both concentrations C_R and C_O converge against the equilibrium concentrations (see Fig. 3.37). In case of the unlimited current, the concentration C_O is greater than $1\,kmol\,m^{-3}$ directly after the applied voltage pulse (see Fig. 3.36a) which means redeposition happens. In that case (unlimited current), Cu^+ ions disperse via diffusion and the concentration C_O falls below $1\,kmol\,m^{-3}$. In the long term copper is oxidised until the equilibrium is reached for the potential.

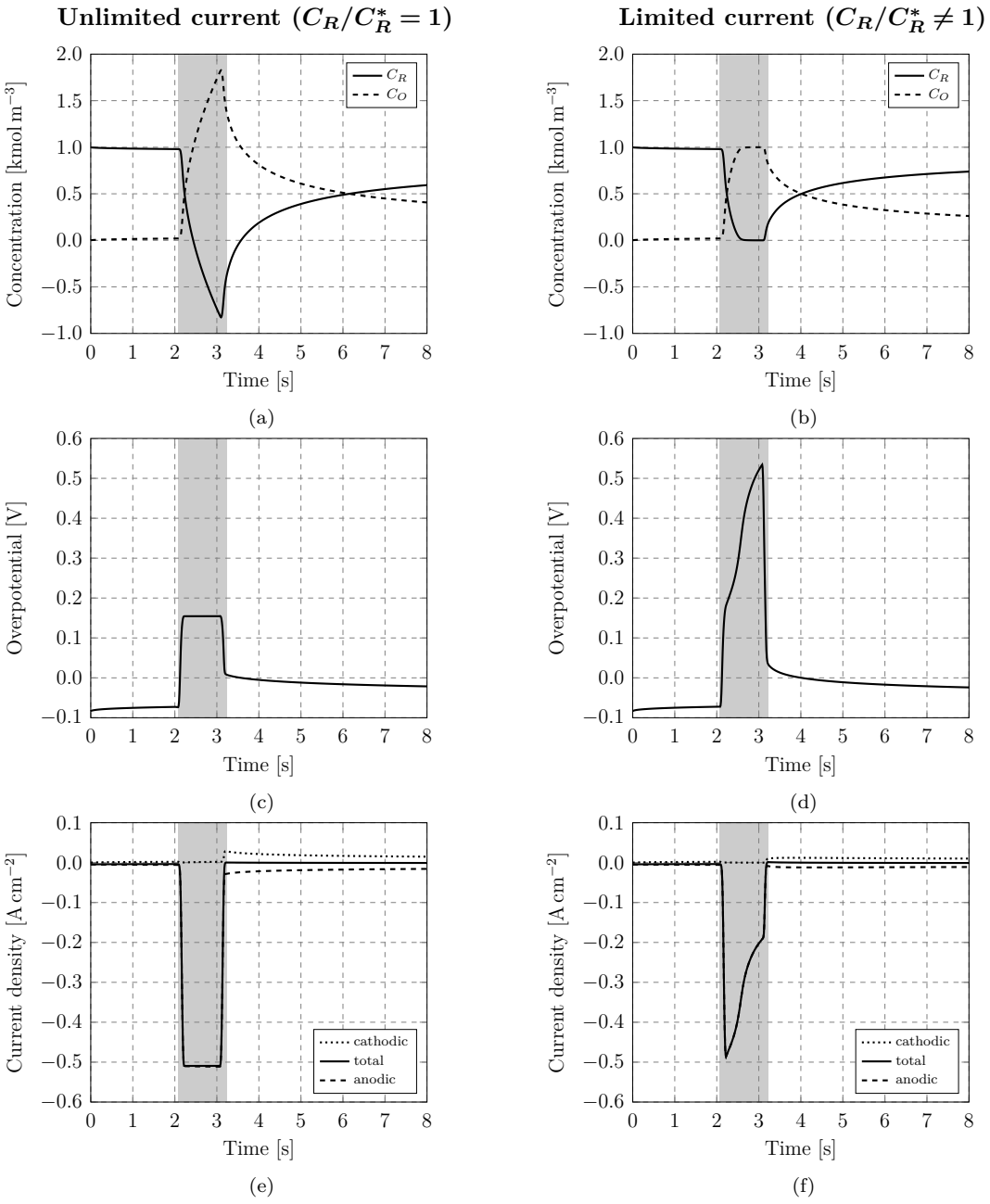

Figure 3.36: **Concentration, overpotential and current density (one-dimensional model)** This figure shows the concentration for oxidising and reducing species (C_O and C_R), the overpotential and the current density at the WE. In simulations which results are shown in the left column the factor C_R/C_R^* in the Butler–Volmer equation was set to one (unlimited current). Simulation results in which this factor was considered, i.e., C_R/C_R^* not set to one, are shown in the right column (limited current). Additionally, the time during which the voltage pulse is applied (pulse(t) $\neq 0$) is highlighted in grey. With the initial values of C_O and C_R set to the respective initial values ($C_{O,init}$ and $C_{R,init}$), their values change due to the applied voltage pulse.

Any results presented in the following were done with C_R/C_R^* set to one (unlimited current). To investigate and verify the concentrations at equilibrium, simulations without the voltage pulse were carried out. This means, the electrode potential ϕ_s at the WE was set to the OCV all the time. Results from these simulations are shown in Fig. 3.37.

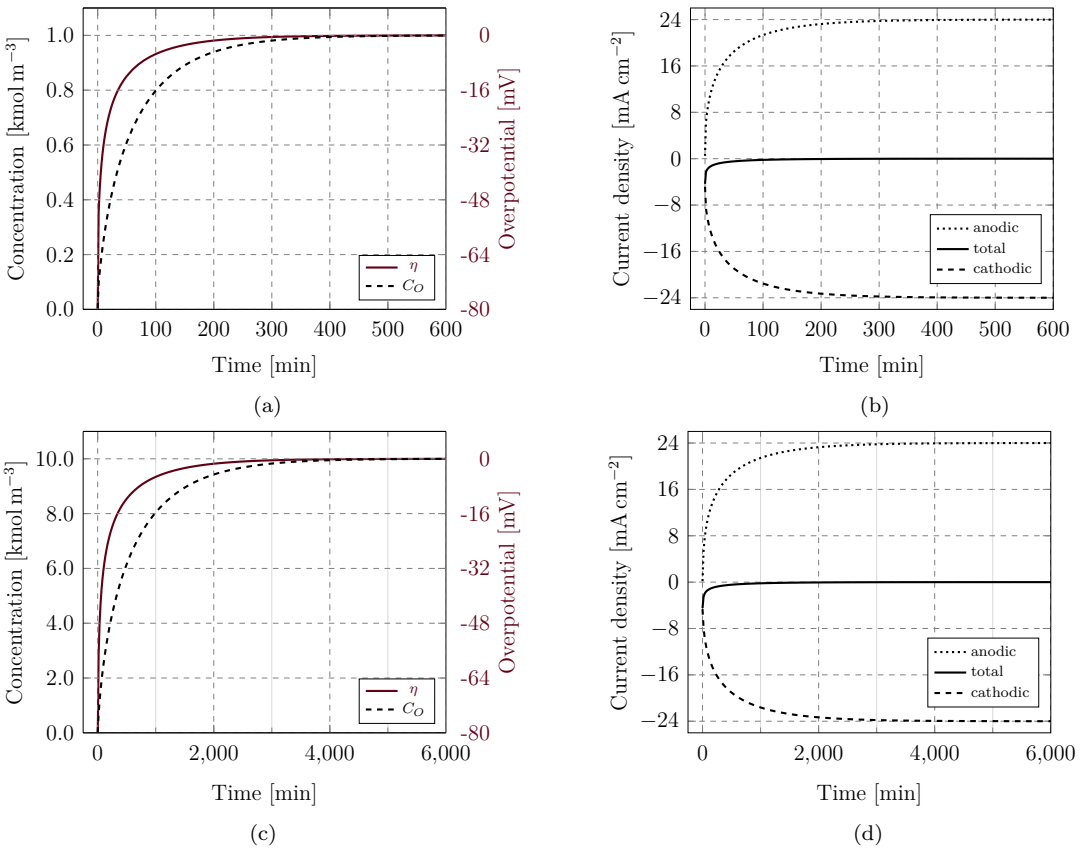

Figure 3.37: **Concentration C_O, overpotential and current density at equilibrium**. This figure shows the concentration C_O, the overpotential and the current density evaluated at the WE. The top two figures show results from simulations for which the bulk concentration C_O^* was set to 1 kmol m^{-3} and the bottom two figures show results from simulations for which C_O^* was set to 10 kmol m^{-3}. Please note the different scaling of the left y axis of the two left figures.

At equilibrium no current flows and the overpotential is zero. Applying these conditions to the concentration-dependent Butler–Volmer equation as defined by Eq. (2.31) yields the concentration C_O at equilibrium which is equal to the reference concentration C_O^*. Due to the rate at which any concentration changes being proportional to the current it takes a long time until equilibrium is achieved. At equilibrium the overpotential is zero and the absolute value of the anodic and cathodic contributions to the Butler–Volmer equation are equal to the exchange current density (24 mA cm^{-2}). Please note that Fig. 3.37 shows results obtained from a time-dependent study. During this current distribution initialisation (see Sec. 3.2.2) which preceeds the time-dependent study as well as during initialisation of the time-dependent step, initial values of the liquid potential and the involved concentrations are determined.

Hence, the obtained values at $t = 0$ in Fig. 3.37 deviate from the set initial values. For the set intial values of the concentrations $C_{R,init}$ and $C_{O,init}$, the overpotential is approximately $-1\,\mathrm{V}$ which can be calculated using Eq. (2.31). This means, at the beginning of the simulation strong etching of the WE occurs due to the set initial values and the etching rate decreases with time. Hence, at $t = 0$ the concentration C_O at the WE is $\approx 4\,\mathrm{mol\,m^{-3}}$ and the overpotential is $\approx -80\,\mathrm{mV}$. The transition from the set initial values to the corresponding values at $t = 0$ are not resolved in the obtained simulation results which are depicted in Fig. 3.37. This transition of parameters from their initial set values until their values at $t = 0$ is not resolved in any simulation concerning this thesis. The intial values of concentrations for oxidising and reducing species were set so that simulation results utilising concentration-dependent kinetics can be compared to simulations in which all electrochemistry was substituted using an influx of concentration (see Sec. 3.3). While the simulated operational mode (square-wave pulse voltammetry) of the cell is only used to optimise its shape and performance, the final operational mode of the electrochemical cell may differ substantially. In general, initialisation of the electrochemical cell especially in regard to the set potential values is quite challenging and must be considered carefully (in relation to the operational mode of the cell). Additional information about this topic can be found in [59, p.470ff; 60; 61; 62].

3.5.2 Three-Dimensional Model

In this section the results of concentration-dependent kinetics using a three-dimensional model will be discussed. The considered model is shown in Fig. 3.1 and only the WE was subject to concentration dependency which was set up as described previously (infinite Cu reservoir).

3.5.3 Comparison of CIK and CDK (Fluid Flow)

Simulations with different pressure differences between inlet and outlet were performed to investigate the impact of mass transport by flow on the electrochemical cell. In the following, a discussion of simulation results which utilised a pressure difference of 1 Pa between inlet and outlet will be given. This applied pressure difference is the same value as the value used in simulations using concentration-independent kinetics (see Sec. 3.4).

3.5.3.1 Concentration and Current Density on the Working Electrode

Similarly as the discussion of the current density utilising concentration-independent kinetics, the main focus will be on the current density at the centre line (y = z = 0) of the working electrode, which represents a good evaluation due to the symmetry of the cell. Figure 3.38 shows the time-dependent behaviour of the current density on the working electrode.

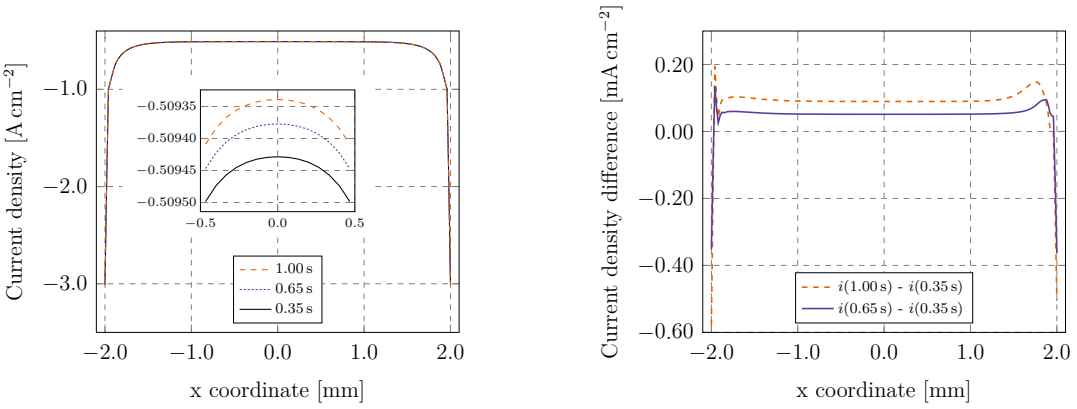

Figure 3.38: **Time-dependent behaviour of the current density on the WE (line evaluation)**. By utilising concentration-dependent kinetics, (a) shows the current density evaluated on a line across the centre of the WE, i.e., at y = z = 0, exemplarily for three different times of the simulation and (b) shows the difference between the two stated data sets. The inset in (a) shows a zoom for values of the current density in the centre.

While for simulations using concentration-independent kinetics the current density does not change while the applied voltage pulse is 1 V its values change with time when concentration dependency is considered. With the exception of the extrema on the edges of the WE (x = ± 2 mm) the current density is quite homogeneous over the electrode surface. Hence, discussion of parameters can be done on three x points located at x = –2, 0 and 2 mm. Figure 3.39 shows the time-dependent behaviour of the current density on the WE evaluated on these three points as well as the concentration profiles across a line evaluation (y = z = 0) on the WE for three different times.

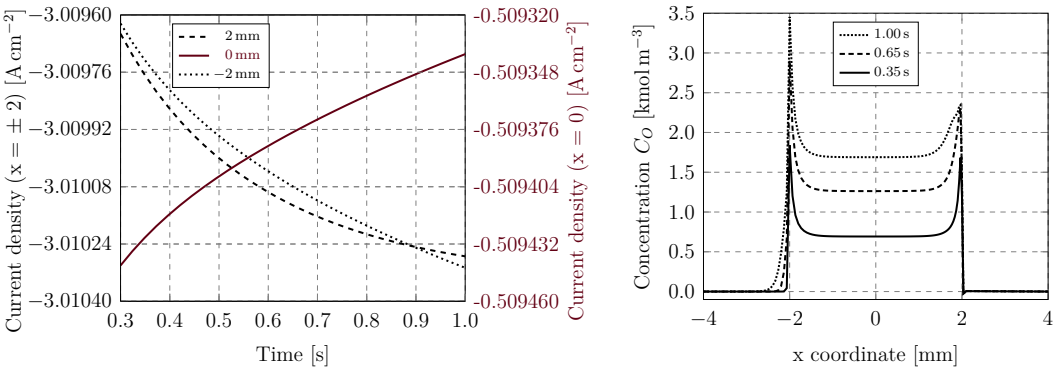

Figure 3.39: **Point trace of current density and a selection of concentrations (flow)**. While (a) shows the time-dependent behaviour of the current density evaluated on three points residing at x = –2, 0, 2 mm on a line in the centre of the WE, i.e., at y = z = 0, (b) shows the concentration C_O for three different times across a line in the middle of the WE, i.e., at y = z = 0.

Figure 3.40 shows a point evaluation of the overpotential and the ratio C_O/C_O^*.

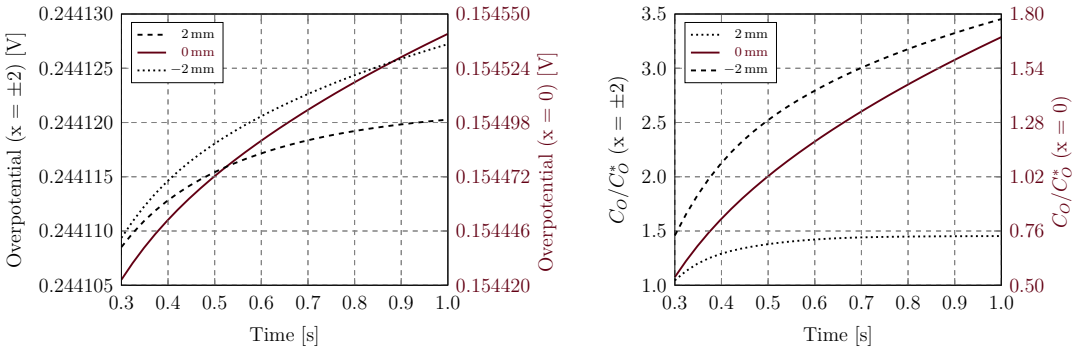

(a) (b)

Figure 3.40: **Point trace of overpotential and concentration C_O (flow).** In the centre of the WE (y = z = 0), (a) shows the overpotential and (b) shows the ratio C_O/C_O^* evaluated at x = –2 and 2 mm. The simulations were done using concentration-dependent kinetics and the pressure difference between inlet and outlet was set to 1 Pa.

The prefactor for the reducing species C_R/C_R^* in the Butler–Volmer equation is set to one and therefore the only source of concentration-dependence is due to the concentration C_O. Since flow transports species C_O from the inlet to the outlet, more concentration accumulates on the side closer to the outlet (x = −2 mm). Depending on the sign and magnitude of the applied potential, the emerging current in the cell depends on the Butler–Volmer equation. Figure 3.41 shows the corresponding potential-dependent current densities occuring at both electrode surfaces for the considered simulated electrochemical system.

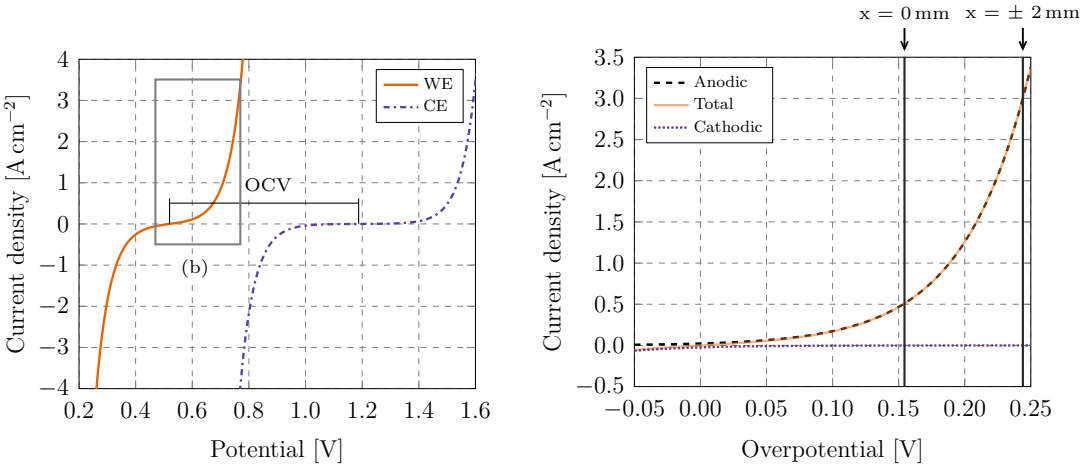

(a) (b)

Figure 3.41: **Anodic, cathodic and total current according to the Butler–Volmer equation.** (a) shows the total current according to the Butler–Volmer equation for the WE and CE surfaces with the x axis representing the electrode potential given by Eq. (2.27). (b) shows a zoom of the data shown in (a) for the WE with the overpotential on the x axis. Additionally, this figure also shows the anodic and cathodic contribution to the total current density as well as the overpotential for three different x positions x = –2, 0, 2 mm on the WE (evaluated on a line where y = z = 0).

No concentration dependence was considered in the depiction of the Butler–Volmer equation

in Fig. 3.41, i.e., the figure was generated using $C_O/C_O^* = 1$. This was done due to the negligible impact of the concentration on the current density. The overpotential at the WE ranges between approximately 0.15 V and 0.24 V at the centre and the edges of this electrode surface, respectively. For these values of the overpotential the anodic part of the current density prevails which is not subject to concentration dependence (infinite reservoir of solid copper). Hence, the small impact of concentration on the current density. The average values of the overpotential at the WE and CE are approximately 0.160 V and −0.295 V, respectively. The average values of the liquid potential are −0.348 V and −0.893 V at the WE and CE, respectively. In all simulations the electrode potential ϕ_s was set to a certain (fixed) value (another way of setting up concentration dependence is to prescribe a fixed (total) current at the electrode interface which results in change of the potential with time). For example between times 0.3 and 1.0 s its value is OVC+1.0 V and does not change with time. During this time ($t = [0.3\,\text{s}, 1.0\,\text{s}]$), the average overpotential increases and the average liquid potential decreases. Since the total current is governed by Ohm's law the total current also decreases in this time interval.

Figure 3.42 shows the anodic and cathodic part of the current density for two different points on the WE.

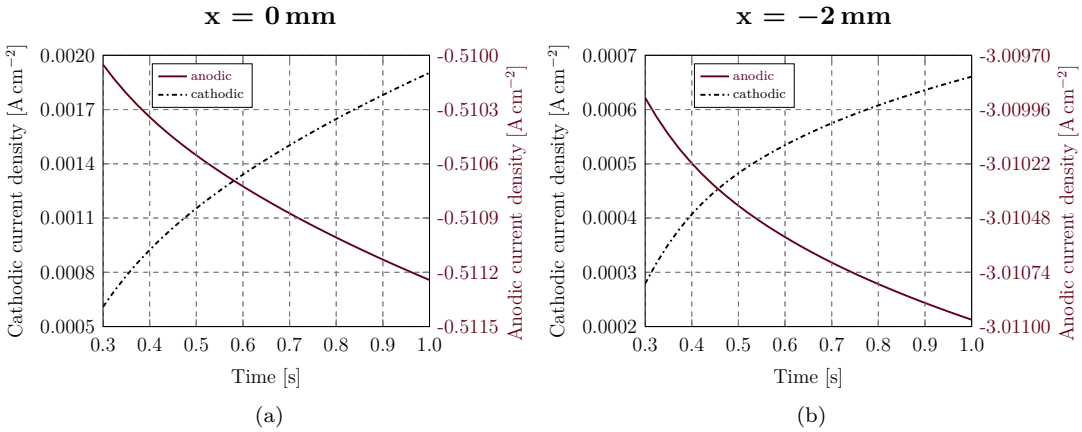

(a) (b)

Figure 3.42: **Point evaluation of the anodic and cathodic current density on the WE**. This figure shows the time-dependent behaviour of the anodic and cathodic contribution to the total current density. (a) shows the point evaluation for x = 0 and (b) the point evaluation for x = −2 mm.

By adding up the anodic and cathodic contribution in each point in Figs. 3.42a and 3.42b the corresponding values of the total current as shown in Fig. 3.39a can be obtained. The values of anodic and cathodic current density are obtained by calculating the scalar product of the current density obtained from the Butler–Volmer equation with the surface normal vector (see Eq. (2.41)). Since the z component of the normal vector at the WE surface is –1 the corresponding values have the opposite sign (cf. Figs. 3.41b and 3.42).

The change in current density across the electrode surface depends on the overpotential as well as the local concentrations. In the centre of the WE (x = 0) the overpotential is smaller than at the edges (x = ± 2 mm). Hence, in the centre the ratio of the anodic to the cathodic contribution to the current density is smaller (taking absolute values). Since the concentration dependence is only considered for the cathodic current, its impact is greater for smaller overpotentials. This can be seen in Fig. 3.42a. The anodic contribution to the

current density slightly increases its absolute value with time at positions x = 0 and 2 mm since the cathodic current increases. The impact of time on the current density is minor since the C_R contributions in the Butler–Volmer equation were suppressed (unlimited current, $C_R/C_R^* = 1$).

3.5.3.2 Total Current

Integration of the local current density across the electrode surface yields to total cell current, which is shown in Fig. 3.43.

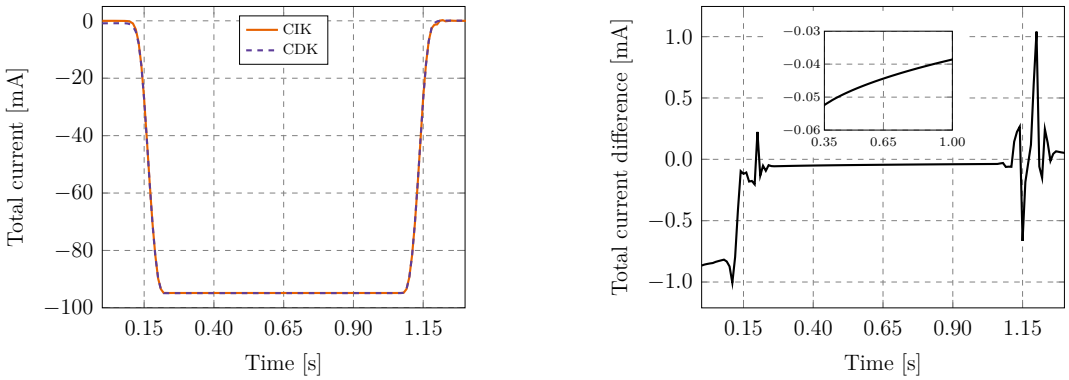

Figure 3.43: **Total cell current versus time (CIK and CDK)**. (a) shows the total cell current as a function of time for simulations using concentration-independent and concentration-dependent Butler–Volmer kinetics denoted CIK and CDK, respectively. (b) shows the difference between the two data sets shown in (a).

Surface integration of the local current density over either of the electrode surfaces yields the total cell current, which has same absolute value but negative or positive sign depending whether integration is being performed over the WE or CE, respectively. The negative sign of the total cell current at the WE is a result of this electrode acting as an anode which means it acts as an electron sink and hence, direction of the local current density must point towards said electrode surface. By observing the trend of the total current in the cell, its values for simulations using CIK are constant at the plateau of the applied voltage pulse, i.e., at times between around 0.2 and 1.05 s the total current in the cell remains constant for CIK simulations. Using concentration dependence the total current decreases with time. The reason for that is the decrease in local current density in the centre of the WE which makes up the major part of the total current (see Fig. 3.39a).

3.5.3.3 Total Cell Integrated and Average Outlet Concentration

A comparison of the total (integrated over the cell volume) and average outlet concentration utilising different assumptions regarding electrochemistry is shown in Fig. 3.44. Each data set shown in this figure was normalised to an area of one under the curve.

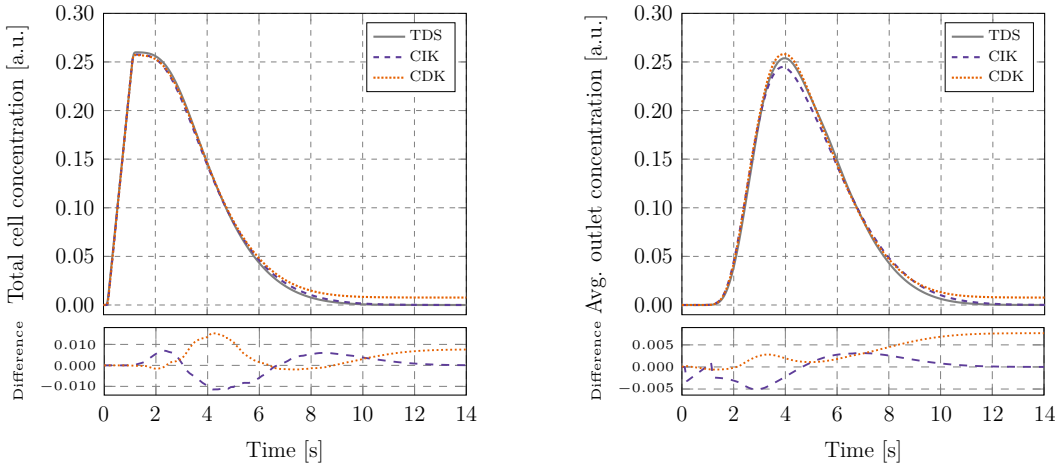

(a) (b)

Figure 3.44: **Total cell- and average outlet concentration (TDS, CIK and CDK)**. Each of the two top figures show normalised results obtained from transient simulations using a concentration influx via the *transport of diluted species* (TDS) module, electrochemistry without concentration dependent electrode kinetics (CIK) and electrochemistry including concentration dependent kinetics (CDK). For simulations using electrochemistry, the potential at the working electrode was set according to the square pulse which is shown in Fig. 3.18, with the OCV at $C_O = 1\,\mathrm{kmol\,m^{-3}}$ applied before and after the pulse. (a) shows the normalised total concentration in the cell and (b) the normalised average concentration at the cell outlet at any given point in time. Both two bottom parts of each figure show the respective difference plot, i.e., each one presents the difference between one of the two above shown normalised data sets. The dashed data in these figures shows the difference between TDS and CIK data which is also shown in Fig. 3.28 and the dotted line indicates the difference between CIK and CDK simulations.

The concentration C_O does not reach zero when a concentration dependent Butler–Volmer equation is used. This means, copper is being etched after the pulse has stopped which can be seen in Fig. 3.44 for $t > 10\,\mathrm{s}$.

3.5.3.4 Working Electrode Etching

With the timeint operater provided by COMSOL Multiphysics any variable can be integrated over time in all mesh points. Using this operator, the surface charge density and total exposure to reaction products (concentration C_O) of the working electrode surface during the whole simulation time was calculated. This is shown in Fig. 3.45. The surface charge density depicts the trend of the local current density over the WE. The extrema occur at the electrode edges ($\mathrm{x} = \pm\,2\,\mathrm{mm}$). In the y direction there is no significant deviation in the surface charge density. The comparison between the two time-integrated data sets with and without concentration dependence is shown in Fig. 3.46.

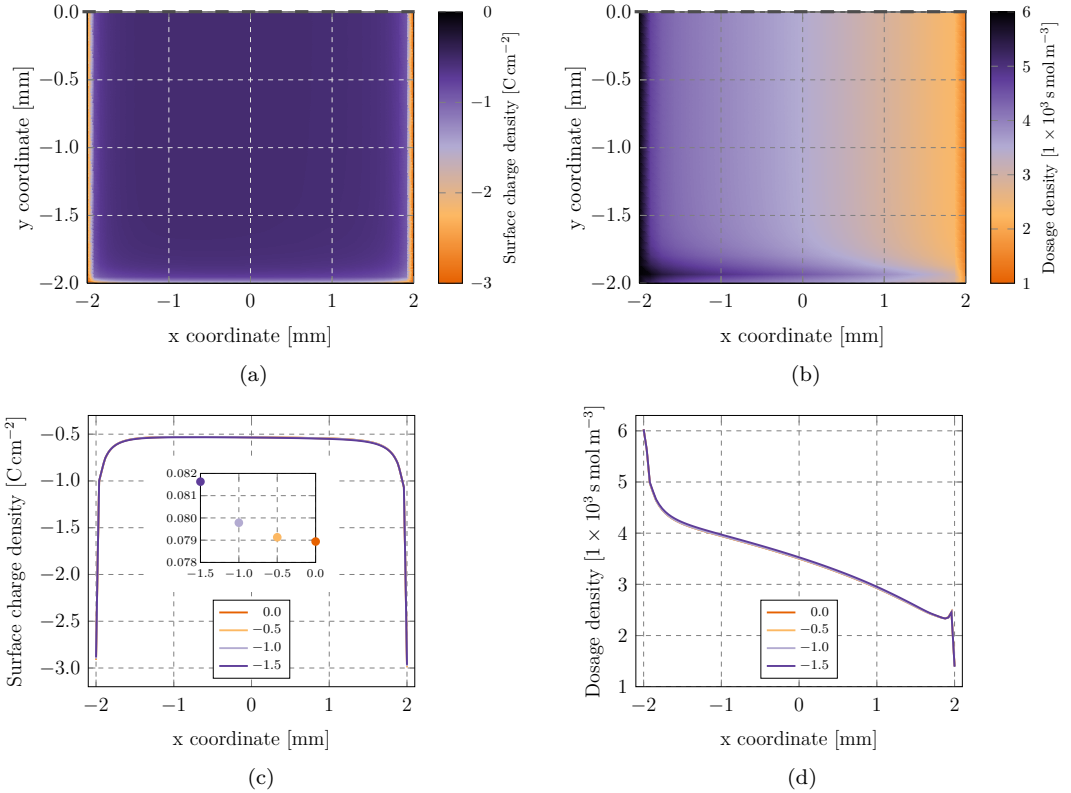

Figure 3.45: **Time integration: current density and concentration**. (a) shows the time integral of the normal current density over the working electrode for all simulation times and (b) the time-integrated concentration over the working electrode for all times. This means, the integration was performed for simulation times between zero and 14 s. Both figures (a) and (b) only show half of the spatial data indicated by the dashed symmetry line. Additionally, (c) and (d) show a line evaluation of the data shown above at different y positions (y = 0, −0.5, −1 and −1.5 mm) indicated in the legend. For the line evaluations in (c) the inset shows the difference between values of the surface charge density located at x = −2 mm and x = 2 mm as a function of y.

During the time of a simulation a total electric charge of 0.1 C flows through each electrode surface. Hence, for the considered reactions at both electrode surfaces the amount of species generated is $n = Q/F = 0.1\,\mathrm{C}/96\,485\,\mathrm{C\,mol^{-1}} \approx 1 \times 10^{-6}$ mol. Assuming faradaic reactions only, this amount of species is equivalent to a total number of transferred copper ions given by $m = nN_A = 1 \times 10^{-6}\,\mathrm{mol} \cdot 6.022 \times 10^{23}\,\mathrm{Cu^+/mol} \approx 6 \times 10^{17}\,\mathrm{Cu^+}$. The atomic volume of copper is $1.182 \times 10^{-29}\,\mathrm{m^3}$ [63]. Therefore, a total volume of $\approx 7 \times 10^{-12}\,\mathrm{m^3}$ is removed from the WE during the simulated experiment. On average a depth of 0.46 µm copper is removed from the WE surface which is equivalent to a number of around 2000 atomic layers. On the CE hydrogen gas is emitted. Under standard conditions 1×10^{-6} mol is equivalent to $\approx 12\,\mathrm{mm^3}$ (the molar volume of an ideal gas is approximately $22.4 \times 10^{-3}\,\mathrm{m^3\,mol^{-1}}$ [64]). Compared to the dimensions of the cell this generated gas volume is substantial and would severely perturb the flow field.

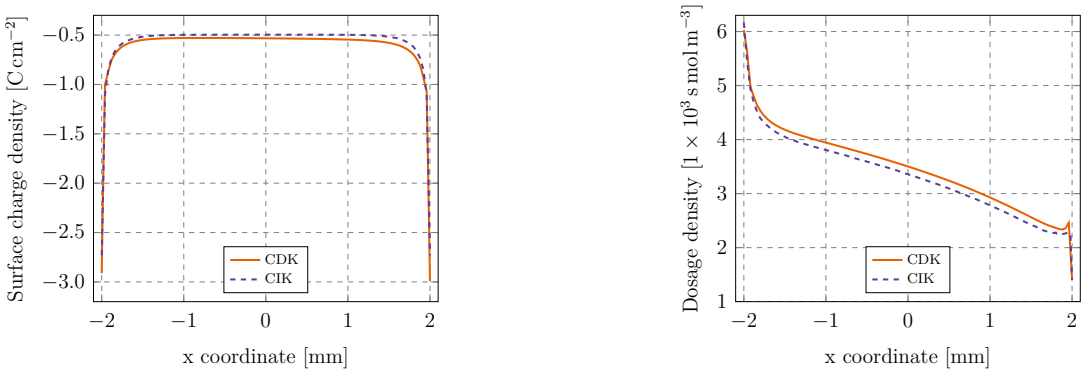

(a) (b)

Figure 3.46: **Time integration: current density and concentration over the WE (CIK vs CDK)**. Evaluated on x = 0 on the WE this figure shows both time-integrated data sets (normal electrolyte current density and concentration C_O for simulations using concentration-dependent kinetics (CDK) and concentration-independent kinetics (CIK).

3.5.4 Dependence on the Flow

In the following, the impact of different values of the pressure difference between inlet and outlet will be discussed with regard to the local current density and concentration across the WE. While the geometry remained unchanged (see Fig. 3.1) two different simulations with a pressure difference between inlet and outlet of 0 and 10 Pa were performed.

3.5.4.1 Concentration and Current Density on the Working Electrode at Fast Flow

In the following, simulations using a pressure difference of 10 Pa will be presented. Figure 3.47 shows a point evaluation of the current density and a line evaluation of the concentration C_O at the WE.

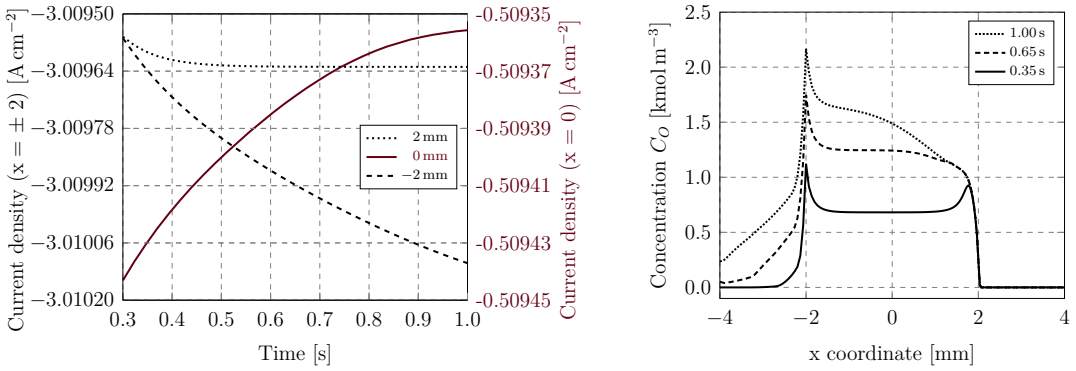

(a) (b)

Figure 3.47: **Current density at selected points and concentration profile for Δp = 10 Pa**. Similar to the data shown in Fig. 3.39, (a) shows the normal current density as a function of time for the points x = −2, 0 and 2 mm (y = z = 0). For a selection of three times, (b) shows the concentration profile of the reaction products on the working electrode (y = z = 0). Both figures present results from a simulation in which the pressure difference between inlet and outlet Δp was set to 10 Pa.

At the WE positions x = ± 2 mm the concentration C_O is the main impact on the current density. Please note the asymmetric distribution of C_O compared to Fig. 3.39b. The overpotential and the ratio C_O/C_O^* are shown in Fig. 3.48.

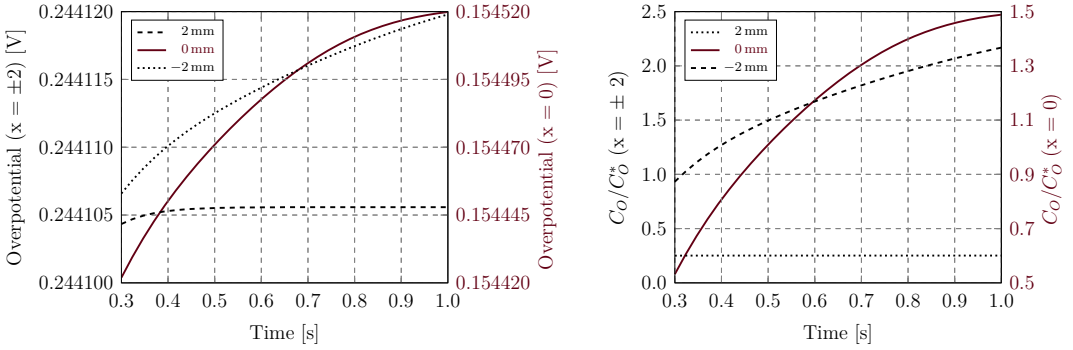

(a) (b)

Figure 3.48: **Overpotential and ratio C_O/C_O^* at selected points for Δp = 10 Pa**. Similar to the data shown in Fig. 3.40, as a function of time, (a) shows the overpotential and (b) the ratio C_O/C_O^* evaluated at the points x = –2, 0 and 2 mm (y = z = 0). Both figures present results from a simulation in which the pressure difference between inlet and outlet Δp was set to 10 Pa.

3.5.4.2 Concentration and Current Density on the Working Electrode without Flow

Simulation results during which no flow happens at all, i.e., where the pressure difference between inlet and outlet was set to 0 Pa, will be presented in this section. Figure 3.49 shows the normal current density at selected points and the concentration C_O evaluated on a line across the WE.

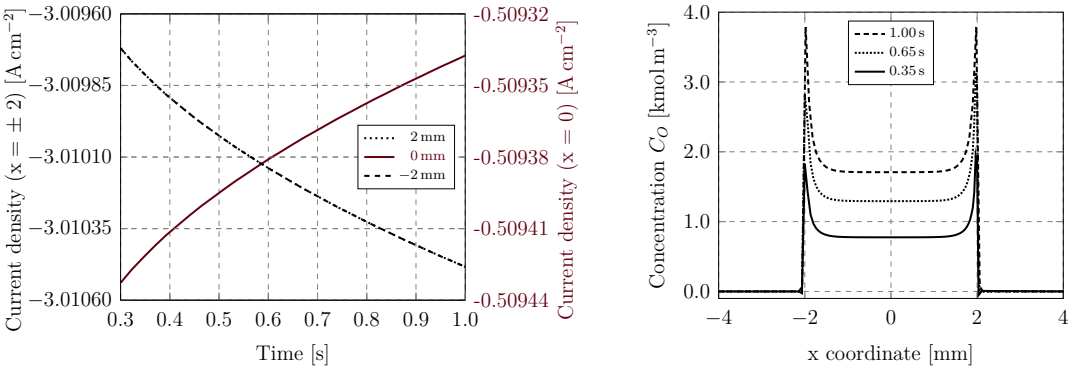

(a) (b)

Figure 3.49: **Current density at selected points and concentration profile for Δp = 0 Pa**. Similar to the data shown in Fig. 3.39, (a) shows the normal current density as a function of time for the points x = –2, 0 and 2 mm (y = z = 0). For a selection of three times, (b) shows the concentration profile of the reaction products on the working electrode (y = z = 0). Both figures show data in which the pressure between inlet and outlet Δp was set to 0 Pa, i.e., no flow happens at all..

The current density is the same for both points where x = ± 2 mm. Figure 3.50 shows the overpotential and the ratio C_O/C_O^* at x = –2, 0 and 2 mm.

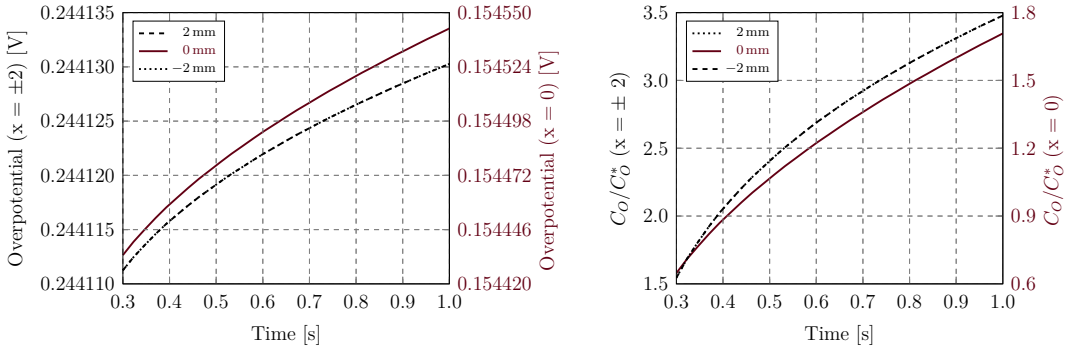

(a) (b)

Figure 3.50: **Point trace of current density and concentration C_O for Δp = 0 Pa**. In the centre of the WE (y = z = 0), (a) shows the overpotential at x = –2, 0 and 2 mm and (b) shows the ratio C_O/C_O^* evaluated at x = –2, 0 and 2 mm. The simulations were done using concentration-dependent kinetics and the pressure difference between inlet and outlet was set to 0 Pa.

3.5.5 Total Current Depending on the Flow

In the following, impact of the applied pressure difference on the total cell current, which is shown in Fig. 3.51, will be discussed.

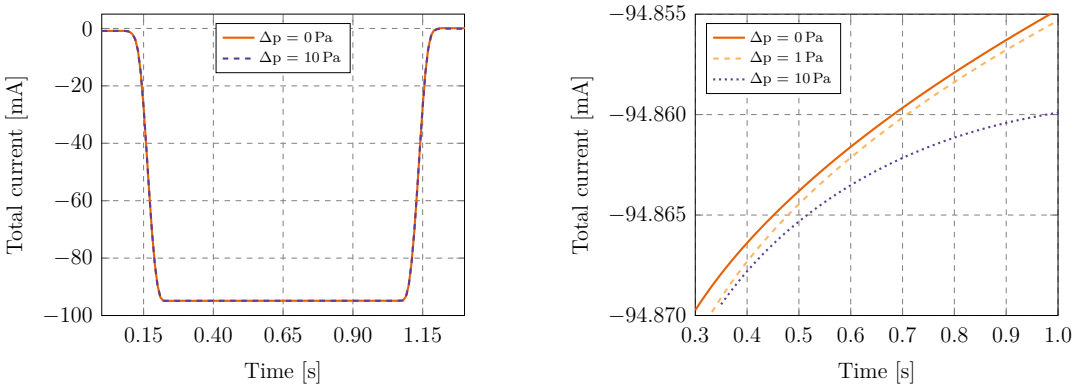

(a) (b)

Figure 3.51: **Comparison of total cell current depending on inlet pressure and time**. a) total cell current versus time for simulations utilising pressure differences between inlet and outlet of 0 and 10 Pa. (b) shows a zoom of the same data for times between 0.3 and 1.0 s.

While the impact of flow on the total cell current is very small, it is still interesting to analyse the effect of flow in detail, see Fig. 3.51b. The absolute value of the total cell current decreases less with increasing throughput and the decrease of current in time arises from the increase of the concentration C_O. This effect is very small since the flow of current is mainly governed by the electrical conductivity of the electrolyte rather than the overpotential.

3.6 Parameter Variation

In order to investigate the cell performance with changing cell parameters, simulations utilising different electrode positions and channel heights were carried out. The channel height is defined as the distance between working electrode (WE) and counter electrode (CE), which was set to 0.5 mm in previous simulations. This parameter is important when probing the surface using infrared spectroscopy due to the liquid layer in the channel height attenuating light due to absorption. Hence, this distance should be as small as possible. Additionally, the surface of the WE must be freely accessible to infrared light. The placement of the CE is crucial here since in general materials which conduct electricity either absorb or reflect infrared radiation. Both parameters will be investigated independently, i.e., first the electrode positioning will be varied while the distance between WE and CE is kept constant. Then, the impact of changing the channel height for fixed electrode positioning will be examined. The main focus of these studies was to determine the influence of both parameters on the current density distribution on the WE.

3.6.1 Electrode Position Variation

All simulations in this parameter study were performed with the WE at a fixed position while the position of the CE was subject to change. For this channel height of 0.5 mm the simulations using concentration- and concentration-independent kinetics do not differ greatly (see Secs. 3.4 and 3.5). Therefore, all simulations regarding electrode position variations were carried out without concentration dependence. Two different studies were conducted, the first one where WE and CE have the same surface area but are shifted against each other. The second type of study utilises a split CE where its surface was split into two different parts.

3.6.1.1 Single Counter Electrode

At first, the relative positioning of two equally sized electrodes, as shown in Fig. 3.52, will be discussed.

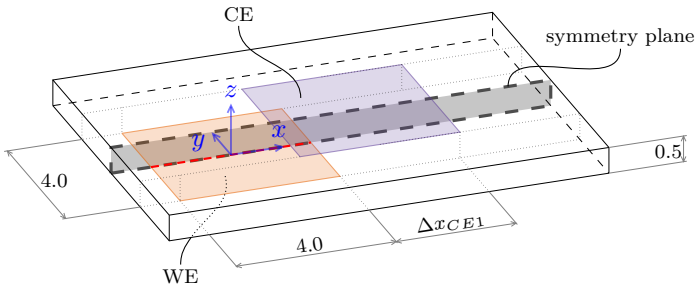

Figure 3.52: **Model of the geometry with single CE displaced towards the inlet**. Both electrodes have the same surface areas ($4 \times 4\,\mathrm{mm}^2$) and are separated by a fixed z distance of 0.5 mm which is denoted channel height. Additionally, the counter electrode (CE) is shifted relatively to the working electrode (WE) by the distance Δx_{CE1}, e.g., a value Δx_{CE1} = zero means both electrodes are perfectly aligned in the xy plane. The subscript of the variable Δx_{CE1} indicates that there is a single counter electrode present. While the depicted geometry represents the whole geometry, in COMSOL Multiphysics only one half was simulated, indicated by the grey xz symmetry plane. The red dashed line which shows the intersection of the symmetry plane and the WE will be used to evaluate data later on. All dimensions in this figure are given in millimetres.

Please note that size and position of the WE surface was not changed compared to any previously performed simulations. The edge of the cell in ±x direction was set so that there is enough space between electrode surfaces and cell boundaries.

For these studies the symmetry of the model was implemented using [19, p.76]

$$\boldsymbol{i_l} \cdot \boldsymbol{n} = 0 \qquad \text{and} \qquad \boldsymbol{i_s} \cdot \boldsymbol{n} = 0. \tag{3.14}$$

Equation (3.14) was applied over the whole symmetry plane which means neither ionic nor electric current is allowed to pass through this surface. Simulations with and without symmetry were done to verify their equality. Simulations for a parameter Δx_{CE1} between 0 and 8 mm with a total number of 20 equally sized steps were performed. Figure 3.53 shows the current density evaluated on the WE for a selection of simulation results.

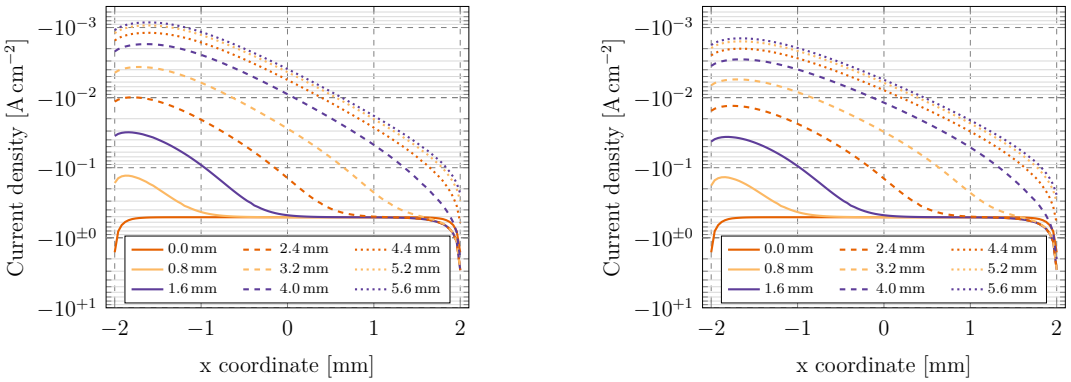

Figure 3.53: **Line evaluations of the current density on the WE for different CE positions** Δx_{CE1}. The legend indicates the displacement of the counter electrode (CE) in units of millimetres, i.e., the parameter Δx_{CE1}. All values depicted in this figure were evaluated at a simulation time t = 0.65 s with (a) and (b) showing a line profile of the current density across the WE (along the red dashed line in Fig. 3.52). (a) y = 0 and (b) y = −1 mm.

Even for the case in which CE and WE are placed directly opposite each other ($\Delta x_{CE1} = 0$) the current density on the electrode edges (x = ±2 mm) has extrema, due to edge effects. With the CE being shifted in positive x direction, the absolute current density at the side of the WE facing the CE (at x = 2 mm) increases locally (up to $\Delta x_{CE1} < 4$ mm), as can be seen in Fig. 3.53. On the other side of the electrode, not facing the CE, (at x = −2 mm) the opposite happens (the current density decreases). At the x = 2 mm side, the change is due to the CE protruding over the WE in direction of the shift, i.e., in positive x direction, which results in a similar current density behaviour as with the model described in Sec. 3.4 where the CE protrudes over both sides of the WE. This behaviour is similar to the simulation results shown in Secs. 3.4 and 3.5. In the model concerning these simulations, the CE overlapped the WE on both sides and the current density on the WE exhibited local extrema at sides closest to this overlap. For a value of Δx_{CE1} between 0 and 4 mm the current density depends on Δx_{CE1} (see Fig. 3.53a). Beyond this distance, i.e., for $\Delta x_{CE1} > 4$ mm, the CE does not face the WE any more. For $\Delta x_{CE1} > 4$ mm, the shape of the $j(x)$ curve does not change substantially. In these cases, the current density just decreases over the whole electrode

surface by a constant factor, as can be seen in Fig. 3.53. This decrease in current density with increasing values of Δx_{CE1} is governed by Ohm's law. The resistance between both electrodes increases since they are farther apart from each other.

The change in current density perpendicular to the shift direction can be inferred from Fig. 3.53a. This figure shows a line profile similar to Fig. 3.53a but evaluated at y = 1 mm. Comparing these two figures one can see that most changes in the current density across the WE occur in the shift direction (x direction). In case where both electrodes directly oppose each other ($\Delta x_{CE1} = 0$), there is no variation of the current density in y direction (see Figs. 3.53a and 3.53b). As the CE is shifted against the WE, the absolute value of the current density in the centre of the WE for a given x value has a minimum at y = 0. This can be seen for example by comparing Figs. 3.53a and 3.53b at x = −1.5 mm for values of the parameter Δx_{CE1} set to 5.6 mm.

3.6.1.2 Split Counter Electrode

The surface area of the WE must be accessible to ensure probing with infrared light during a measurement. While there are many ways to achieve this, this section will consider the case in which the CE is split into two parts, giving direct unobstructed access to the surface of the WE. The geometry considered in this study is shown in Fig. 3.54. Please note that in all parameter studies involving a split CE; the parameter indicating the distance by which the CE are shifted is denoted Δx_{CE2}.

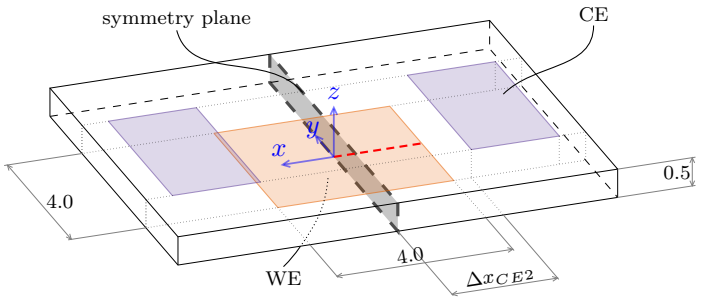

Figure 3.54: **Geometry with a split CE**. The sum of both CE surface areas is equal to the surface area of the WE ($4 \times 4\,\mathrm{mm}^2$) and the z distance between WE and both CE parts is the channel height, set to 0.5 mm. Both CE are each shifted a distance Δx_{CE2} against the WE, as shown in the figure. Similarly to Fig. 3.52, this figure includes a grey symmetry plane which was utilised during simulations as well as a red dashed line indicating a line where values are evaluated. Dimensions are given in millimetres.

A total number of ten simulations were carried out with $0 \leq \Delta x_{CE2} \leq 3.6$ mm. Figure 3.55 shows a selection of results from these simulations. From this figure one can see that results using a single CE are similar to the results from simulations utilising a split CE. Shifting the CE induces a strong gradient in the current density on the WE for $0 < \Delta x_{CE2} < 2$ mm (as long as the electrodes at least partially face each other) and beyond $\Delta x_{CE2} = 2$ mm, the current density increases without a major change of the shape of the curve.

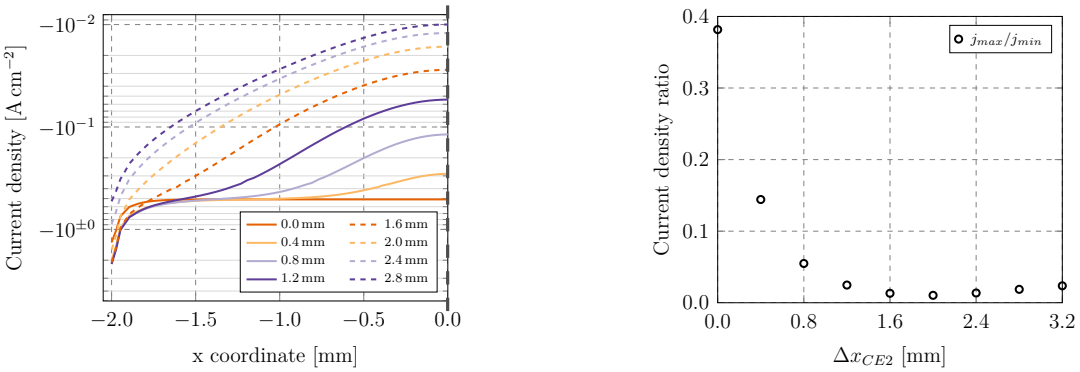

Figure 3.55: **Line profile of the current density on the WE with a split CE**. (a) current density on the WE at t = 0.65 s, evaluated across a line in its centre (see red dashed line in Fig. 3.54), for different Δx_{CE2} positions. (b) shows the ratio between the maximum and minimum value of the current density for the whole data set shown in (a). Please note that (a) only shows data for half the cell indicated by the dashed symmetry line.

This can also be seen in Fig. 3.55b which shows that the relative difference between the minimum and the maximum value of the current density has its minimum at around $\Delta x_{CE2} = 2\,\text{mm}$. Minimum- and maximum absolute value of the current density on the WE surface occur in the centre (x = 0) and the electrode edges (x = ±2 mm), respectively. Please note that Fig. 3.55a shows only half of the total geometry indicated by the dashed line at x = 0. The distribution of the current density across the whole electrode surface is shown in Fig. 3.56 for $\Delta x_{CE2} = 1.2\,\text{mm}$.

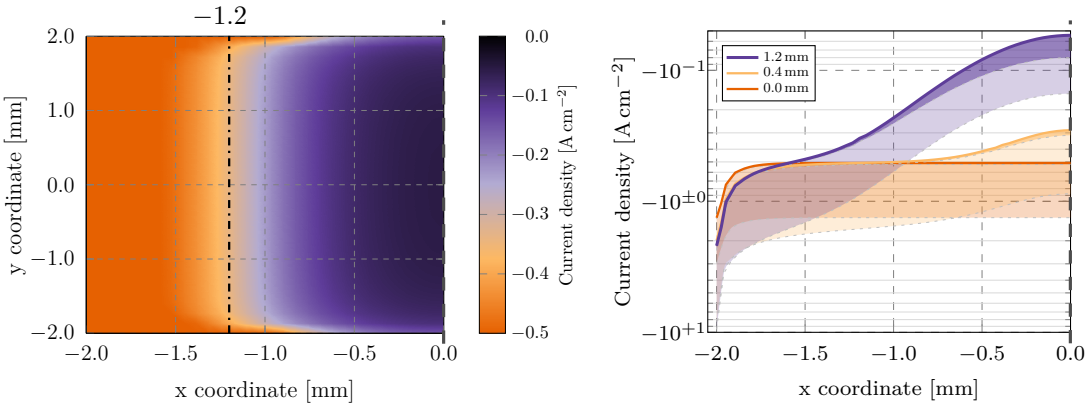

Figure 3.56: **Evaluation of the current density on the WE (split CE)**. (a) Current density on the WE for a parameter $\Delta x_{CE2} = 1.2\,\text{mm}$. The projected x position of the CE edge on the WE is indicated by a dash-dotted line. (b) Current density on the WE in x direction with the shaded area indicating the variation of the current density in the y direction (dark colour: $|y| \leq 1.724\,\text{mm}$ and light colour: $|y| \leq 2\,\text{mm}$). This means, for the three Δx_{CE2} values in the legend, the profile of the current density across a line in x direction will reside in the respective shaded area. See text for details.

Extraction of the data as shown in Fig. 3.56b goes as follows. For three values of the parameter Δx_{CE2}, the current density was evaluated on a regular grid across the WE surface. One of these data sets ($\Delta x_{CE2} = 1.2\,\text{mm}$) is shown in Fig. 3.56a. The y coordinate of this data was then compressed. This means, for each x value of the scalar field, the corresponding minimum- and maximum value of the current density in y direction was extracted. The extracted data are shown in Fig. 3.56b. To retain a certain amount of information on the variation of the current density in x direction, two different intervals were considered. The y value of 1.724 mm which divides these two intervals was chosen arbitrarily. Results show a similar trend as results from simulations using a single CE (see Sec. 3.6.1.1). At y = 0, the absolute value of the current density has a minimum. With increasing or decreasing values of the y coordinate, the absolute value of the current density increases. The largest change in the current density on the WE occurs at its edges (at y = ±2 mm) and the gradient depends on the value of Δx_{CE2}, as can be seen in Fig. 3.56b.

3.6.2 Channel Height Variation

This section deals with the impact of a change in the channel height, i.e., the distance between both electrodes in z direction. To decouple effects caused by electrode positions and due to a change in channel height, all simulations presented in this section were performed using simulations with both electrodes at a fixed position, facing each other. The chosen positions for working electrode (WE) and counter electrode (CE) represent the case for $\Delta x_{CE} = 0$ (see Figs. 3.52 and 3.54). All simulations regarding this study were performed using concentration-dependent kinetics. To be able to compare different simulations utilising different channel heights, the inlet pressures were set so that the average velocity in the channel given by

$$\overline{v} = \frac{1}{h}\int_0^h u(z)\,dz = \frac{1}{h}\int_0^h \frac{1}{2\mu}\frac{dp}{dx} z(h-z)\,dz = \frac{h^2}{12\mu}\frac{dp}{dx}, \tag{3.15}$$

was constant for any set channel height h. At the cell outlet a pressure of p = 0 is assumed and the length over which the pressure difference is being applied remains the same for all simulations. Using these premises and Eq. (3.15), a relationship between different channel heights and inlet pressures, indicated by their respective subscript index, given by

$$p_{in,2} = \left(\frac{h_1}{h_2}\right)^2 p_{in,1}, \tag{3.16}$$

can be obtained. Equation (3.16) means that in order for the average fluid velocity to remain constant, by increasing the channel height by a factor of two one must decrease the inlet pressure by a factor of four. Simulations for this paramter variation were performed the following. The average velocity in the channel was set to a constant value of $2.6042\,\text{mm}\,\text{s}^{-1}$ which corresponds to an inlet pressure $p_{in,1} = 1\,\text{Pa}$ and a channel height $h_1 = 0.5\,\text{mm}$, which is the value for the geometry and settings corresponding to all previously performed simulations. Simulations with different channel heights h_2 were performed while the pressure $p_{in,2}$ was set according to Eq. (3.16) to ensure a constant average fluid velocity throughout the cell. All simulations were performed using concentration-dependent kinetics with the same settings as before, e.g., the potential at the WE was set to a pulse of one second length according to the function depicted in Fig. 3.18, etc. Inserting the above given values of h_1 and $p_{in,1}$

into Eqs. (3.15) and (3.16) yields the desired constant value of $\overline{v}$ which is not dependent on the channel height anymore. Figure 3.57 shows the fluid velocity profile exemplarily for two different values of the channel height.

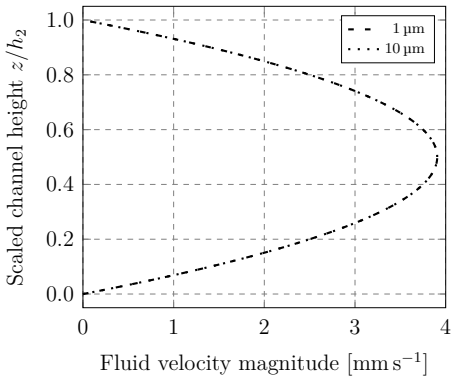

Figure 3.57: **Fluid velocity profile $u(z)$ for two different channel heights h_2.** Fluid velocity $u(z)$ as a function of the scaled z coordinate according to Eq. (2.44). The evaluation was done using Eqs. (3.15) and (3.16) with h_1 and $p_{in,1}$ set to 0.5 mm and 1 Pa, respectively. The pressures 2.5 kPa and 250 kPa were set for channel heights 10 µm and 1 µm, respectively.

From this figure it can be seen that the fluid velocity profile across the scaled z coordinate is independent of the channel height. While the analytical solution and simulation agree down to channel heights of 1 µm, one should be careful because for example the role of surface roughness becomes more important the smaller the distance between the electrodes gets; this is not considered in simulations. Hence, the lower limit of the channel height for the simulations was set to an arbitrary value of 5 µm and simulations with channel heights ranging from 5 to 25 µm in 5 µm steps were performed.

3.6.2.1 Current Density on both Electrodes

Figure 3.58 shows the current density on both electrode surfaces for simulations with a channel height of 5 and 25 µm

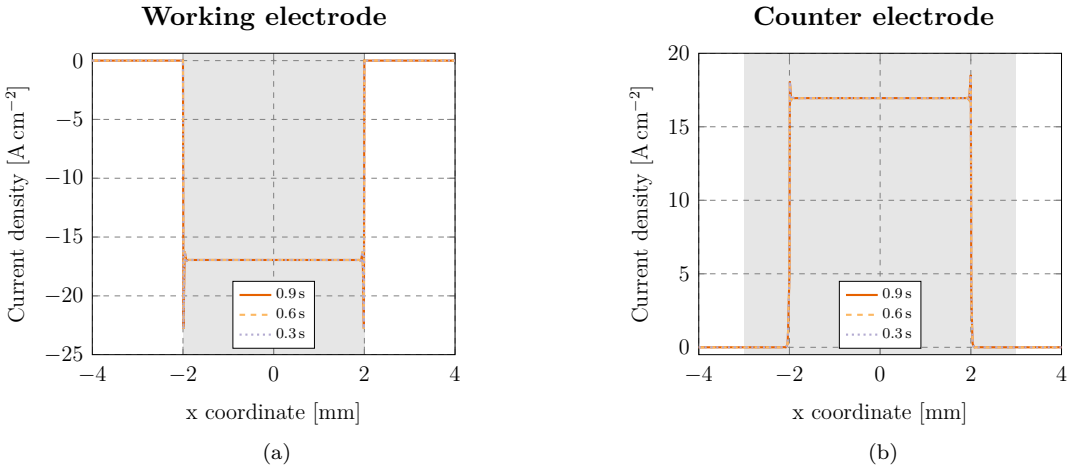

(a) (b)

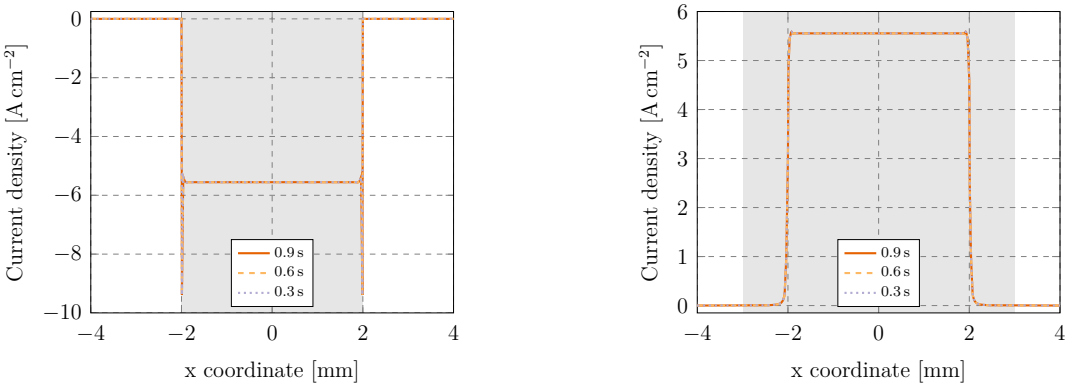

Figure 3.58: **Current density on both electrodes (5 µm and 25 µm channel height).** For three different times all figures show the normal current density evaluated on a y = 0 line. The figures in the first row show results from simulations performed with a channel height of 5 µm and the second row show results from a simulation utilising a channel height of 25 µm. The left column shows evaluated values on the WE (z = 0) and the right column the corresponding values at the CE (z = 5 and 25 µm). Additionally, the grey areas highlight the respective electrode surfaces, e.g., the CE ranges between x = ± 3 mm.

Similar to previously discussed simulations using electrochemistry, the current density on the WE has extrema at the edges (x = ± 2 mm) for simulations utilising a small channel height. At these small distances between WE and CE, the current flows to the most part only directly between these two electrodes. This means, while the CE ranges between x = –3 and 3 mm the current density is greater than zero only for –2 < x < 2 mm which are the dimensions of the WE. With the distane between WE and CE increasing, the current density on the CE is non-zero at x < −2 mm and x > 2 mm (cf. Figs. 3.24b and 3.58d).

3.6.2.2 Total Current

Figure 3.59 shows the total cell current as a function of time, as was obtained by surface integration of the local current density over the WE surface at each time step of the simulation.

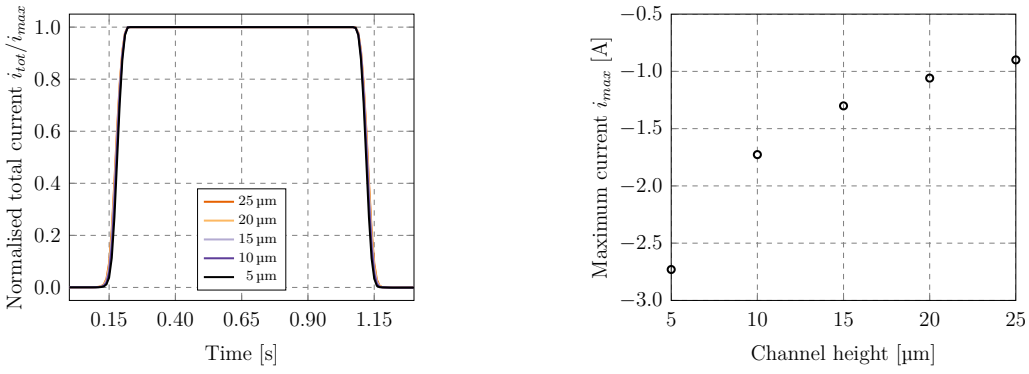

Figure 3.59: **Total cell current as a function of time, depending on the channel height.** (a) shows the normalised surface integration of the local current density across the WE depending on the set channel height and b) the maximum total current i_{max} as a function of the channel height. Hence, values from (b) represent the factors by which each respective plot in (a) was normalised.

The total current in the cell increases with decreasing channel height as can be seen in Fig. 3.59b. Figure 3.60 shows a zoom of the normalised total current for times between 0.25 and 1.05 s.

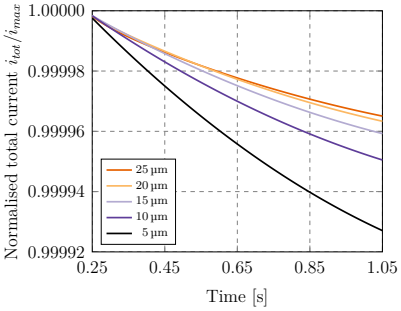

Figure 3.60: **Total cell current as a function of time, depending on the channel height (zoom)**. This figure shows the same data as Fig. 3.59a for a zoom on the x axis.

3.6.2.3 Total Cell Integrated and Average Outlet Concentration

Figure 3.61 shows the total (integrated over the cell volume) and average outlet concentration in the cell depending on the channel height. Each of the data sets was normalised to an area of one.

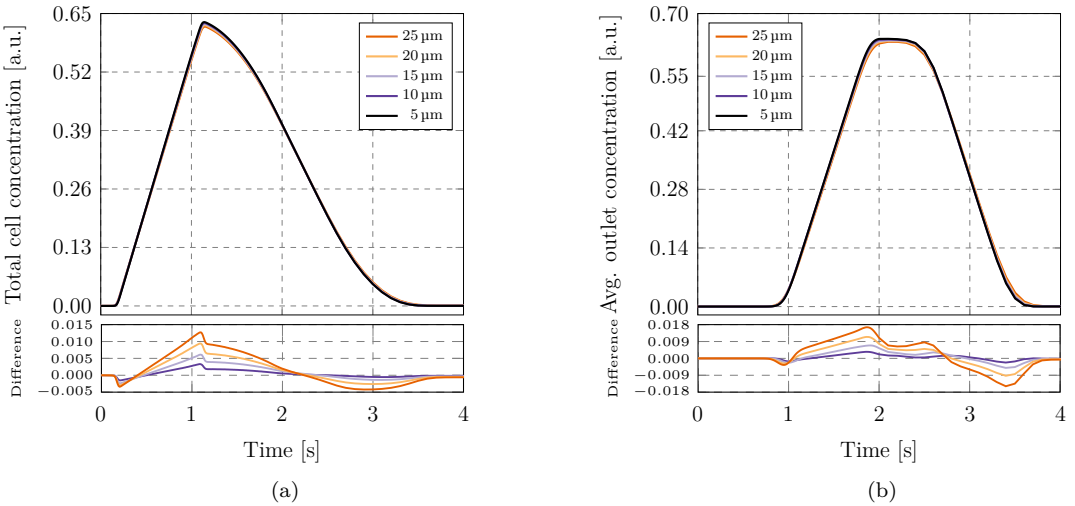

Figure 3.61: **Total cell integrated and average outlet concentration depending on the channel height**. The top part of (a) and (b) show the total cell concentration and average outlet concentration, respectively. Simulations using concentration-dependent kinetics with varying channel heights between 5 and 25 µm in 5 µm steps were performed. Each of the bottom parts in (a) and (b) show the difference between the data set for h = 5 µm and the four others, calculated for the data shown in the top part.

Increasing the channel height while adjusting the pressure difference in order to keep the average fluid velocity constant causes the generated species to remain slightly longer in the cell volume. For comparison, for a channel height of 0.5 mm the last concentration exits the cell at around 12 s (cf. Figs. 3.28 and 3.61). This behaviour can be explained with the information presented in Sec. 3.3.1. By keeping the average fluid velocity constant, the scaled velocity profile in z direction is the same (see Fig. 3.57). This means, for a larger channel height the diffusion length away from the electrode in relation to the channel height is smaller which results in the reaction products leaving the cell more slowly with increasing channel height.

3.6.2.4 Line Profiles of the Concentration on the Working Electrode

For a selection of times, Fig. 3.62 shows the concentration C_O on the working electrode. It must be noted that these values are not physically meaningful, one would have to reduce the voltage of the pulse for realistic values. Nevertheless, the results demonstrate the effect of flow on the concentration profiles.

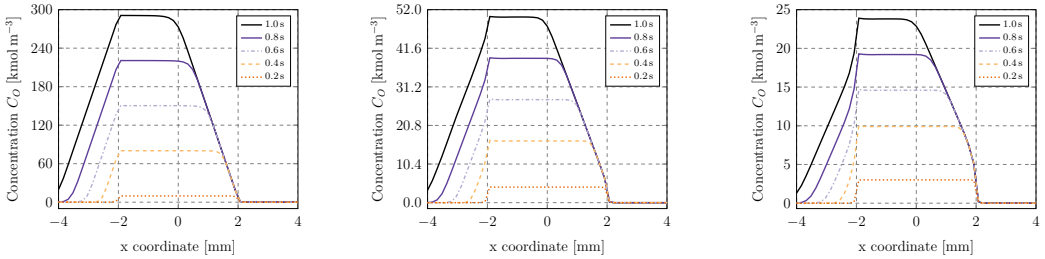

Figure 3.62: **Time-dependent line profiles of the concentration C_O at the WE for different channel heights**. For a selection of times, this figure shows the concentration C_O at y = z = 0, for channel heights of 5, 15 and 25 µm in (a), (b) and (c), respectively.

3.6.2.5 Working Electrode Etching

The time integration of the current density and concentration C_O across the WE surface is shown in Fig. 3.63.

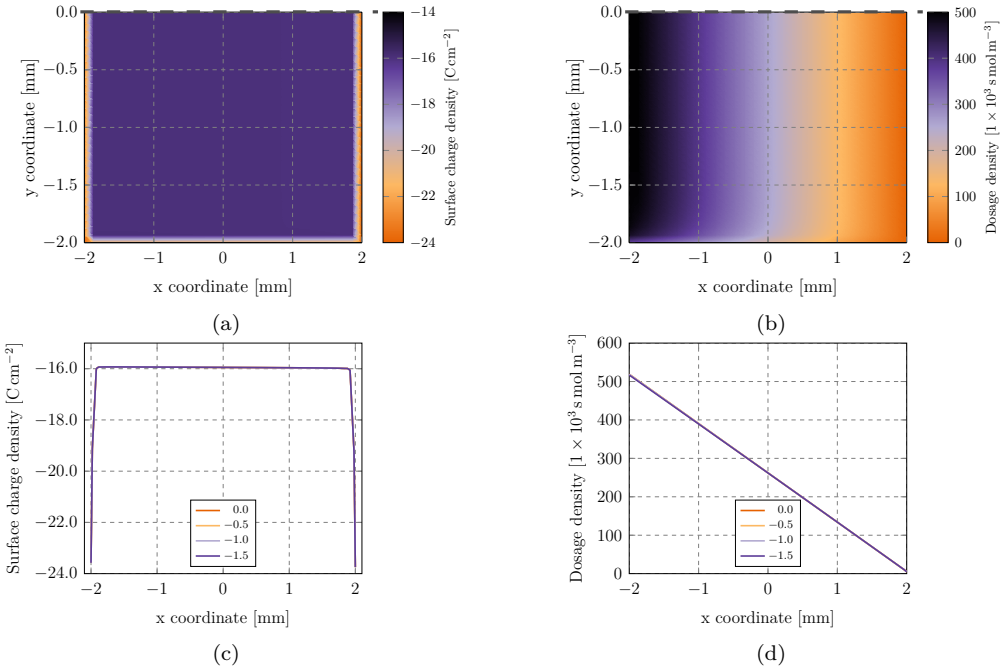

Figure 3.63: **Time integration: current density and concentration**. (a) shows the time integral of the normal current density over the working electrode for all simulation times and (b) the time-integrated concentration over the working electrode for all times. This means, the integration was performed for simulation times between zero and 14 s. Both figures (a) and (b) only show half of the spatial data indicated by the dashed symmetry line. Additionally, (c) and (d) present a line evaluation of the data shown above at different y positions indicated in the legend.

3.6.2.6 Mass Transport in the Cell

In the following, the transport of species C_O through the cell will be discussed depending on time for two different channel heights.

Five Micrometre Channel Height

Figure 3.64 shows the concentration in the cell for a channel height of 5 µm for a selection of simulation time steps. The concentration isolines should be compared with the ones as shown in Fig. 3.32 on page 54 (500 µm channel height). Extraction of these lines was performed by evaluation of the concentration C_O on a slice in the centre of the cell and from this data the isolines were extracted as described on page 54. As for the thicker cells, inlet is positioned at x = 4 mm, the outlet resides on the opposite side, and fluid moves from right to left in Fig. 3.64. The WE is positioned between x = ±2 mm. The concentration was evaluated on the central plane of the cell, i.e., y = 0. Despite this evaluation on a single plane one can assume that the shown concentration on a slice will be the same for a wide range in y direction. This is due to the fact that the current density in y direction is very homogeneous which has been shown previously.

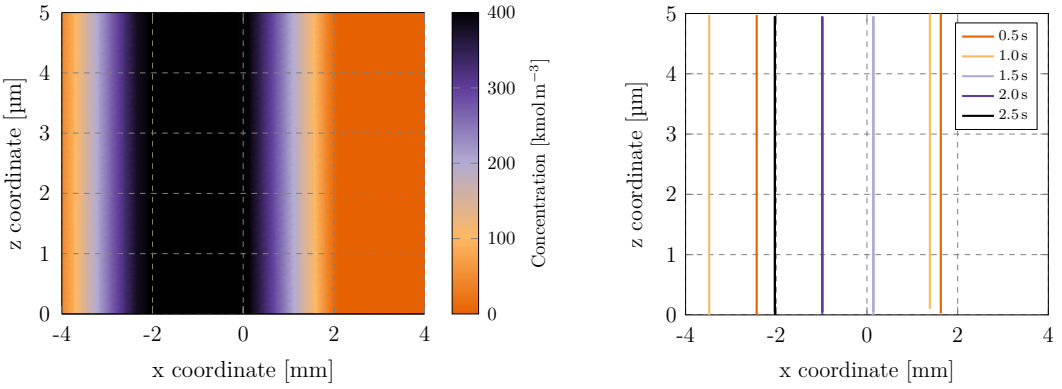

Figure 3.64: **Reaction product concentration in the y = 0 plane and extracted isolines (5 µm channel height)**. Both figures evaluate the concentration C_O in the central plane of the cell, i.e., at y = 0. (a) shows this concentration at a simulation time of 1 s and (b) shows 95 percent isolines of concentration at different times. This means, at each time step the lines enclose 95 percent of the total concentration residing in the slice.

For times around up to 1 s, the concentration C_O has not reached the outlet side of the cell. For times greater than 1.5 s, there is only one single isoline enclosing 95 % of the concentration. Hence, the second line enclosing 95 % of the concentration is beyond the simulated cell outlet for these times. Boundaries enclosing the 95 percent isosurfaces are straight lines since it takes any concentration released at the electrode surface only a few milliseconds to reach to opposite wall by diffusion. The time it takes a particle to diffuse the distance between the electrodes can be calculated using Eq. (2.49).

25 Micrometre Channel Height

For a channel height of 25 µm, the concentration C_O in the y = 0 plane is plotted in Fig. 3.65, exactly the same way as in Fig. 3.64.

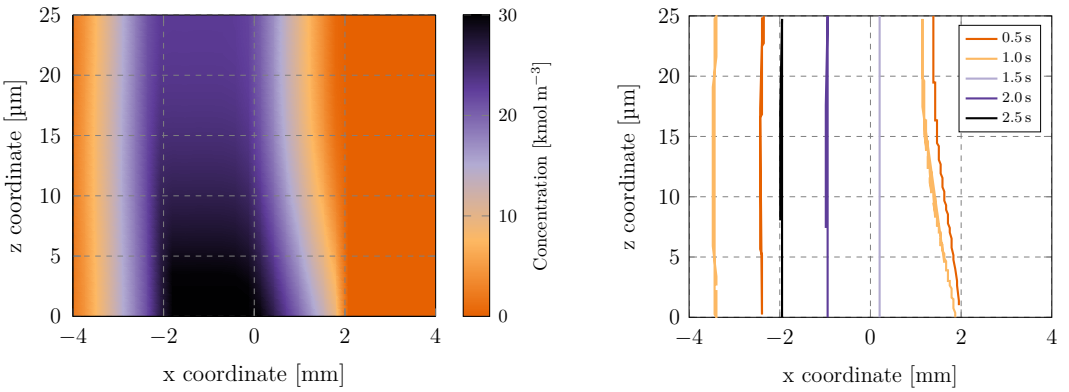

(a) (b)

Figure 3.65: **Reaction product concentration in the y = 0 plane and extracted isolines (25 µm channel height).** Both figures evaluate the concentration C_O in the central plane of the cell, i.e., at y = 0. (a) shows this concentration at a simulation time of 1 s and (b) shows 95 percent isolines of concentration at different times. This means, at each time step the lines enclose 95 percent of the total concentration residing in the slice.

Using this channel height, it takes any species emitted at the electrode surface around 100 ms to reach the other electrode side. Since the fluid velocity in the centre of the channel is higher than at the vicinity of the WE surface, the lines enclosing 95 percent of the concentration are curved in direction of the flow. From this figure it can also be seen that for larger channel heights the concentration in the vicinity of the WE surface is higher due to the longer time it takes species to diffuse away from the electrode surface (in contrast to Fig. 3.64, where diffusion from the bottom to the top is extremely fast).

Section 4

Conclusion and Outlook

In this thesis, simulations of an electrochemical flow cell were performed with the goal to assess its performance and provide design criteria for the practical implementation of such a cell. This section will present a brief summery and overview of the information gained.

Designing an electrochemical flow cell is a challenging task especially in the field of surface science. In this application, greatest care must be taken with respect to the probed surface since one is interested in the state of the surface on an atomistic level. The final design of the cell will incorporate many different techniques. These are for example coupling the electrochemical cell to an ultra-high vacuum system, probing the surface during measurements in-situ using infrared absorption spectroscopy and detection of reaction species via differential electrochemical mass spectrometry (DEMS). The simulations in this thesis serve as a good starting point to model the real cell. In this thesis an electrochemical flow cell was simulated using a simple model geometry. The simplified square geometry was chosen to investigate involved effects separately. These are for example the positioning of electrodes, mass transport in the cell and the channel height (distance of the liquid above the surface which is being probed with infrared).

The surface will be probed for example by applying a voltage pulse. Due to this voltage pulse applied at the working electrode (the surface of interest) current flows in the electrochemical cell. The local current density distribution on the electrodes depends on its positioning. At the electrode-electrolyte interface the electric current is converted into an ionic current. This means, species are generated and the rate of generation is proportional to the local current density. The generated species are then transported from the surface to the outlet due to fluid flow and diffusion. This concentration detected at the outlet yields the residence time distribution (RTD curve). These RTD curves, which represent the average outlet concentration depending on time, can be used to optimise the cell. Optimisations include electrode positioning as well as other cell parameters like for example the cell geometry. Using these curves one may for example determine concentration residing in the cell for an unwanted long time (dead spots). This increases the tail of the RTD curves and using simulations, these regions causing a prolongation of RTD curves may be identified.

Simulations of an applied voltage pulse were performed and this results in a local current density on the electrode surface which depends on the positioning of the electrodes in the cell. The electrodes in simulations were defined so that local effects caused by their placement can be resolved. These effects are mainly the distribution of the current density over the electrode surfaces. Using simulations, regions with high current densities, i.e., with a high reaction rate can be identified directly via surface evaluation of the current density. With this information the electrode positions in the cell can be optimised. The ideal cell has a uniform

current density across the electrode surface. In this case the whole surface will be probed at the same rate which is important in surface science. Different contributions of the current density to the RTD curves can also be extracted using simulations as was demonstrated in this thesis.

Mass transport by flow and diffusion plays an important role. Directly at the electrode surface, the fluid velocity is zero. Therefore, any species generated at the electrode must first diffuse some distance before it gets transported by the fluid flow. The flow of fluid is necessary to transport the species away from the electrode to the point where it is being detected. The time it takes for species to be moved away from the electrode therefore depends on diffusion and the fluid velocity. With a low velocity, reaction products will accumulate more in the vicinity of the electrode surface. An increasing concentration of reaction products will shift the equilibrium potential and lead to a deacreasing reaction rate. Effects of concentration on the performance of the electrochemical cell, called concentration dependence, are very important when designing cells which utilise a thin layer of electrolyte (thin layer cells). Using the concentration-dependent Butler–Volmer equation, the RTD curvee was calculated and compared to the one without using concentration dependence. For the chosen geometry which has a channel height of 0.5 mm and the reaction rate depending only on the concentration of the reaction products, no substantial difference between these two cases was observed (The channel height is defined as the height of the liquid layer above the working electrode).

In the last part of this thesis, simulations were performed to investigate the impact of two different cell parameters. These two parameters were positioning of electrodes and impact of the channel height on the cell performance. For the first study the current density on the working electrode (WE) was evaluated depending on the position of the counter electrode (The counter electrode (CE) is the electrode which completes the circuit which means current flows between WE and CE). For these simulations, both electrodes are assumed to have the same surface area and are separated by a distance of 0.5 mm, i.e., the channel height. Starting from the case where both electrodes are directly opposing each other, simulations were performed with the CE shifted against the WE. Even for the case in which both electrodes are directly opposing each other, the current density on the electrodes is not uniform but is higher on the edges. With a shift between both electrodes, high local gradients in the current density across the electrode surfaces occur and the reaction rate becomes very inhomogeneous. This is especially important when the surface is probed with infrared spectroscopy, where a CE facing the WE would block the IR light. The second parameter study involved the channel height. In this study, only the distance between the electrodes was subject to change. The in-plane positions of the WE and the CE remained the same (directly opposing each other) and the channel height was changed. For channel heights between five and 25 µm, simulations were performed, including effects of concentration dependence. Results show that for the simulated experiment (dissolution of metal by an applied voltage) no significant impact of the reaction products on the cell performance occurs. This means, results from this thesis are only valid for this experiment and the simulations must be adapted if the experiment differs.

Using simulations, the concentration of generated species can be evaluated at any point and time. With this information it is possible to evaluate and visualise the mass transport of reaction products through the cell due to flow and diffusion. An application of these simulations may be to optimise the position of the DEMS detection. At the optimal position, a maximum concentration of reaction products would be detected via DEMS which can be

determined using simulations.

With all the above described, points a good starting point for an optimisation of the real cell is provided. Depending on the final design, certain simplifications used in the simulations performed in this thesis may not hold to a certain extent and certain points must be considered.

- **Two dimensional electrode surfaces (WE and CE)**
  The working and counter electrode were modelled using two-dimensional surfaces. A three dimensional electrode will have a different current density distribution over its surface. The more the real electrode placement of WE and CE differes from a two-dimensional set-up, the more severe this effect becomes. This can only be resolved by modelling these electrodes in three dimensions.

- **Effects caused by the reference electrode**
  To keep the simulations simple, no reference electrode was considered. In COMSOL Multiphysics the reference electrode is only available through a point constraint. This means, it has no volume and it is simulated using only a single point. Since no current flows through the reference electrode (the overpotential is zero) its measured reference potential is proportional to the liquid potential [19, p.133]. Due to the spatial extent of a real reference electrode it will average the sensed liquid potential. The greater the variations of the liquid potential over the reference electrodes spatial extents, the more severe this effect gets [65, 66]. Using simulations this effect can be investigated. Since the provided interface of the reference electrode is only available as a point constraint in COMSOL Multiphysics version 5.4, an implementation this electrode in more than one dimension must be set up manually.

- **High current density**
  For simplicity the electric potential of the WE in all simulations utilising electrochemistry remained the same. This naive approach resulted in large values of the current density. This impacts the rate at which reaction products are generated and it also impacts the potential drop in the electrolyte. Additionally, the potential in the electrolyte is not constant which may impose problems with the reference electrode.

- **Hydrogen gas evolution**
  The amount of hydrogen gas evolving at the CE depends on the current density at the electrode surface. Depending on the operational parameters of the cell (spatial dimensions, applied pressure between inlet and outlet, etc.) this effect may influence the performance of the cell severly. Hence, its impact must be considered in the final design of the cell.

- **Reaction products reaching the counter electrode**
  Another important point are reaction products emitted from the WE reaching the CE during a measurement. This is especially important for cells with a small distance between the electrodes where probing with infrared is desired. One way to circumvent this behaviour is to move the CE upstream which results in an inhomogeneous current density over the electrode surfaces. Both effects can be investigated with the help of simulations.

- **Electrolyte concentration**
  For all simulations, the electrolyte concentration was assumed to be high enough to justify the usage of Ohm's law with a fixed conductivity of the liquid phase. With a low electrolyte concentration, this is not applicable and the Nernst–Planck equations must be solved (named "tertiary current distribution" in COMSOL Multiphysics). In that case, the current in the electrolyte phase is calculated using the concentrations of the dissolved species.

List of Figures

Section 1 – Introduction

Section 2 – Fundamentals

Section 3 – Methodology, Results and Discussion

Mesh Convergence

Transport of Diluted Species (TDS)

Electrochemistry with Concentration-Independent Current (CIK)

Electrochemistry with Concentration-Dependent Current (CDK)

Parameter Variation

List of Tables

Section 3 – Methodology, Results and Discussion

Bibliography

[1] C. R. Catlow, M. Davidson, C. Hardacre, and G. J. Hutchings, "Catalysis Making the World a Better Place", *Philosophical Transactions of the Royal Society A: Mathematical, Physical and Engineering Sciences*, vol. 374, no. 2061, p. 20150089, 2016. (Cited on page 1.)

[2] D. Murzin, *Catalytic Kinetics*. Amsterdam: Elsevier, 2005. (Cited on page 1.)

[3] National Research Council, *Catalysis Looks to the Future*. Washington, DC: The National Academies Press, 1992. (Cited on page 1.)

[4] G. S. Parkinson, "Evolving Single-Atom Catalysis: Fundamental Insights for Rational Design (ERC Research proposal [Part B2])", 2019. (Cited on page 1.)

[5] O. Brummel, F. Faisal, T. Bauer, K. Pohako-Esko, P. Wasserscheid, and J. Libuda, "Ionic Liquid-Modified Electrocatalysts: The Interaction of $[C_1C_2Im][OTf]$ with Pt(111) and its Influence on Methanol Oxidation Studied by Electrochemical IR Spectroscopy", *Electrochimica Acta*, vol. 188, pp. 825–836, 2016. (Cited on page 2.)

[6] D. E. Molina, A. S. Medina, H. Beyenal, and C. F. Ivory, "Design and Finite Element Model of a Microfluidic Platform with Removable Electrodes for Electrochemical Analysis", *Journal of The Electrochemical Society*, vol. 166, pp. B125–B132, 2019. (Cited on page 2.)

[7] Y. Li, W. V. Roy, L. Lagae, and P. M. Vereecken, "Analysis of Fully On-Chip Microfluidic Electrochemical Systems under Laminar Flow", *Electrochimica Acta*, vol. 231, pp. 200–208, 2017. (Cited on page 2.)

[8] S. Sansuk, E. Bitziou, M. B. Joseph, J. A. Covington, M. G. Boutelle, P. R. Unwin, and J. V. Macpherson, "Ultrasensitive Detection of Dopamine Using a Carbon Nanotube Network Microfluidic Flow Electrode", *Analytical Chemistry*, vol. 85, no. 1, pp. 163–169, 2012. (Cited on page 2.)

[9] R. B. Channon, M. B. Joseph, E. Bitziou, A. W. T. Bristow, A. D. Ray, and J. V. Macpherson, "Electrochemical Flow Injection Analysis of Hydrazine in an Excess of an Active Pharmaceutical Ingredient: Achieving Pharmaceutical Detection Limits Electrochemically", *Analytical Chemistry*, vol. 87, no. 19, pp. 10064–10071, 2015. (Cited on page 2.)

[10] M. A. Boles and Y. A. Çengel, *Thermodynamics: An Engineering Approach, fifth Edition*. 2006. (Cited on page 3.)

[11] H. B. Callen, *Thermodynamics and an Introduction to Thermostatistics*. 1985. (Cited on pages 3 and 4.)

[12] S. Glasstone, *Thermodynamics for Chemists*. 1947. (Cited on pages 3 and 4.)

[13] A. J. Bard and L. R. Faulkner, *Electrochemical Methods: Fundamentals and Applications*. John Wiley and Sons, second ed., 2000. (Cited on pages 5, 7, 8, 12, 13, 15, and 25.)

[14] M. Levitus, *Mathematical Methods in Chemistry*. LibreTexts, 2020. (Cited on page 5.)

[15] H. Voigt and T. Neils, "The Equilibrium Constant. (2020, August 22)". https://chem.libretexts.org/@go/page/1362, accessed April 13, 2021. (Cited on pages 6 and 7.)

[16] P. Atkins and J. de Paula, *Physical Chemistry*. eighth ed., 2006. (Cited on pages 6, 7, and 8.)

[17] "IUPAC. Compendium of Chemical Terminology, second ed. (the "Gold Book"). Compiled by A. D. McNaught and A. Wilkinson. Blackwell Scientific Publications, Oxford (1997). Online version (2019-) created by S. J. Chalk". https://goldbook.iupac.org/terms/view/S05908, accessed April 13, 2021. (Cited on page 6.)

[18] F. Scholz, *Electroanalytical Methods: Guide to Experiments and Applications*. Heidelberg New York: Springer, 2010. (Cited on page 7.)

[19] COMSOL Inc., "Electrochemistry Module User's Guide, version 5.3". www.comsol.com, 2017. (Cited on pages 8, 9, 12, 13, 18, 28, 46, 72, and 85.)

[20] T. Yonekura, Y. Tachikawa, T. Yoshizumi, Y. Shiratori, K. Ito, and K. Sasaki, "Exchange Current Density of Solid Oxide Fuel Cell Electrodes", *ECS Transactions*, vol. 35, no. 1, pp. 1007–1014, 2019. (Cited on page 10.)

[21] J. Ekspong, E. Gracia-Espino, and T. Wågberg, "Hydrogen Evolution Reaction Activity of Heterogeneous Materials: A Theoretical Model", *The Journal of Physical Chemistry C*, vol. 124, no. 38, pp. 20911–20921, 2020. (Cited on page 10.)

[22] C. Gabrielli, F. Huet, M. Keddam, A. Macias, and A. Sahar, "Potential Drops due to an Attached Bubble on a Gas-Evolving Electrode", *Journal of Applied Electrochemistry*, vol. 19, no. 5, pp. 617–629, 1989. (Cited on page 12.)

[23] A. Rędzikowski, "Three-Electrode Setup for Measurement of Potential". https://upload.wikimedia.org/wikipedia/commons/2/2f/Three_electrode_setup.png, 2019 (accessed January 09, 2021). (Cited on page 13.)

[24] Enseeg, "Scheme of a Potentiostat". https://upload.wikimedia.org/wikipedia/commons/7/72/Potentiostat3.png, 2008 (accessed January 24, 2021). (Cited on page 14.)

[25] E. Gileadi, *Electrode Kinetics for Chemists, Chemical Engineers, and Materials Scientists*. New York: VCH, 1993. (Cited on page 15.)

[26] G. Inzelt, A. Lewenstam, and F. Scholz, *Handbook of Reference Electrodes*. Springer, 2013. (Cited on page 16.)

[27] COMSOL Inc., "CFD Module User's Guide, version 5.4". www.comsol.com, 2018. (Cited on pages 17, 24, 31, and 46.)

[28] COMSOL Inc., "Chemical Reaction Engineering Module, version 5.4". www.comsol.com, 2018. (Cited on pages 17 and 46.)

[29] COMSOL Inc., "Which Current Distribution Interface Do I Use?". https://www.comsol.com/blogs/current-distribution-interface-use/, 2014 (accessed April 16, 2020). (Cited on pages 18 and 46.)

[30] M. Schlesinger, ed., *Modern Aspects of Electrochemistry No. 44*. Springer New York, 2009. (Cited on page 18.)

[31] S. J. Cobb and J. V. Macpherson, "Enhancing Square Wave Voltammetry Measurements via Electrochemical Analysis of the Non-Faradaic Potential Window", *Analytical Chemistry*, vol. 91, no. 12, pp. 7935–7942, 2019. (Cited on page 18.)

[32] M. Biesheuvel, S. Porada, and J. Dykstra, "The Difference Between Faradaic and Non-Faradaic Electrode Pocesses", 2018. (Cited on page 18.)

[33] P. Biesheuvel and J. Dykstra, *Physics of Electrochemical Processes*. 2020. (Cited on page 18.)

[34] O. Reynolds, "IV. On the Dynamical Theory of Incompressible Viscous Fluids and the Determination of the Criterion", *Philosophical Transactions of the Royal Society of London. (A.)*, vol. 186, pp. 123–164, 1895. (Cited on page 19.)

[35] S. Kandlikar, S. Garimella, D. Li, S. Colin, and M. R. King, *Heat Transfer and Fluid Flow in Minichannels and Microchannels*. 2016. (Cited on page 19.)

[36] A. Willis, J. Peixinho, R. Kerswell, and T. Mullin, "Experimental and Theoretical Progress in Pipe Flow Transition", *Philosophical Transactions of the Royal Society A: Mathematical, Physical and Engineering Sciences*, vol. 366, no. 1876, pp. 2671–2684, 2008. (Cited on page 19.)

[37] H. Schlichting (Deceased) and K. Gersten, *Boundary-Layer Theory*, p. 26. Springer, fourth ed., 1979. (Cited on page 19.)

[38] C. E. Brennen, "An Internet Book on Fluid Dynamics". http://brennen.caltech.edu/fluidbook/, 2006 (accessed April 11, 2021). (Cited on page 20.)

[39] G. McKinley, "2.25 Advanced Fluid Mechanics. Fall 2013. Massachusetts Institute of Technology: MIT OpenCourseWare, https://ocw.mit.edu. License: Creative Commons BY-NC-SA.". https://ocw.mit.edu/courses/mechanical-engineering/2-25-advanced-fluid-mechanics-fall-2013/equations-of-viscous-flow/MIT2_25F13_Couet_and_Pois.pdf, 2008 (accessed April 11, 2021). (Cited on page 20.)

[40] R. J. Houghtalen, A. O. Akan, and N. H. C. Hwang, *Fundamentals of Hydraulic Engineering Systems*. fourth ed., 2009. (Cited on page 20.)

[41] J. Crank, *The Mathematics of Diffusion*. second ed., 1975. (Cited on pages 20 and 21.)

[42] E. A. Codling, M. J. Plank, and S. Benhamou, "Random Walk Models in Biology", *Journal of The Royal Society Interface*, vol. 5, pp. 813–834, Apr. 2008. (Cited on page 21.)

[43] M. K. S. Verma and V. Kumaran, "A Multifold Reduction in the Transition Reynolds Number, and Ultra-Fast Mixing, in a Micro-Channel due to a Dynamical Instability Induced by a Soft Wall", *J. Fluid Mech.*, vol. 727, pp. 407–455, 2013. (Cited on page 25.)

[44] R. K. Ahluwalia, D. D. Papadias, N. N. Kariuki, J.-K. Peng, X. Wang, Y. Tsai, D. G. Graczyk, and D. J. Myers, "Potential Dependence of Pt and Co Dissolution from Platinum-Cobalt Alloy PEFC Catalysts Using Time-Resolved Measurements", *Journal of The Electrochemical Society*, vol. 165, no. 6, pp. F3024–F3035, 2018. (Cited on page 25.)

[45] H. E. Darling, "Conductivity of Sulfuric Acid Solutions.", *Journal of Chemical & Engineering Data*, vol. 9, no. 3, pp. 421–426, 1964. (Cited on page 25.)

[46] W. M. Haynes, ed., *CRC Handbook of Chemistry and Physics, 91st Edition (CRC Handbook of Chemistry & Physics)*. 2010. (Cited on page 25.)

[47] R. Holze, "Table 5.1. Exchange Current Densities and Rate Constants in Aqueous Systems: Datasheet from Landolt-Börnstein - Group IV Physical Chemistry Volume 9A: "Electrochemical Thermodynamics and Kinetics" in SpringerMaterials (https://doi.org/10.1007/978-3-540-45316-1_22)". (Cited on page 25.)

[48] N. M. Marković, B. N. Grgur, and P. N. Ross, "Temperature-Dependent Hydrogen Electrochemistry on Platinum Low-Index Single-Crystal Surfaces in Acid Solutions", *The Journal of Physical Chemistry B*, vol. 101, no. 27, pp. 5405–5413, 1997. (Cited on page 25.)

[49] E. L. Cussler, *Diffusion: Mass Transfer in Fluid Systems*. third ed., 2009. (Cited on page 25.)

[50] J. Kestin, M. Sokolov, and W. A. Wakeham, "Viscosity of Liquid Water in the Range –8 °C to 150 °C", *Journal of Physical and Chemical Reference Data*, vol. 7, no. 3, pp. 941–948, 1978. (Cited on page 25.)

[51] COMSOL Inc., "Understanding, and Changing, the Element Order". https://www.comsol.de/support/knowledgebase/1270, 2020 (accessed February 14, 2021). (Cited on page 28.)

[52] V. Krasteva and S. P. Papazov, "Estimation of Current Density Distribution Under Electrodes for External Defibrillation", *BioMedical Engineering Online*, vol. 1, no. 1, p. 7, 2002. (Cited on page 42.)

[53] S. Tungjitkusolmun, E. J. Woo, H. Cao, J.-Z. Tsai, V. Vorperian, and J. Webster, "Finite Element Analyses of Uniform Current Density Electrodes for Radio-Frequency Cardiac Ablation", *IEEE Transactions on Bio-Medical Engineering*, vol. 47, pp. 32–40, 2000. (Cited on page 42.)

[54] M. Nandanwar and S. Kumar, "Modelling of Effect of Non-Uniform Current Density on the Performance of Soluble Lead Redox Flow Batteries", *Journal of the Electrochemical Society*, vol. 161, pp. A1602–A1610, 2014. (Cited on page 42.)

[55] COMSOL Inc., "What Does Degrees of Freedom (DOFs) Mean in COMSOL Multiphysics?". https://www.comsol.com/support/knowledgebase/875, 2020 (accessed February 19, 2021). (Cited on page 46.)

[56] H. S. Fogler, *Elements of Chemical Reaction Engineering*, p. 879. Pearson Education, fourth ed., 2006. (Cited on page 50.)

[57] V. Shkirskiy, P. Maciel, J. Deconinck, and K. Ogle, "On The Time Resolution of the Atomic Emission Spectroelectrochemistry Method", *Journal of The Electrochemical Society*, vol. 163, pp. C37–C44, 2016. (Cited on page 50.)

[58] A. Pahl (COMSOL Inc.). Private Communication, 2021. (Cited on page 57.)

[59] D. C. Grahame, "The Electrical Double Layer and the Theory of Electrocapillarity.", *Chemical Reviews*, vol. 41, no. 3, pp. 441–501, 1947. (Cited on page 61.)

[60] D. Hochfilzer, J. E. Sørensen, E. L. Clark, S. B. Scott, I. Chorkendorff, and J. Kibsgaard, "The Importance of Potential Control for Accurate Studies of Electrochemical CO Reduction", *ACS Energy Letters*, vol. 6, no. 5, pp. 1879–1885, 2021. (Cited on page 61.)

[61] J. Schnaidt, S. Beckord, A. K. Engstfeld, J. Klein, S. Brimaud, and R. J. Behm, "A Combined UHV-STM-Flow Cell Set-Up for Electrochemical/Electrocatalytic Studies of Structurally Well-Defined UHV Prepared Model Electrodes", *Physical Chemistry Chemical Physics*, vol. 19, no. 6, pp. 4166–4178, 2017. (Cited on page 61.)

[62] C. C. Herrmann, G. G. Perrault, and A. A. Pilla, "Dual Reference Electrode for Electrochemical Pulse Studies", *Analytical Chemistry*, vol. 40, no. 7, pp. 1173–1174, 1968. (Cited on page 61.)

[63] N. J. Simon, E. S. Drexler, and R. P. Reed, "Properties of Copper and Copper Alloys at Cryogenic Temperatures", 1992. (Cited on page 67.)

[64] P. J. Mohr, D. B. Newell, and B. N. Taylor, "CODATA Recommended Values of the Fundamental Physical Constants: 2014", *Rev. Mod. Phys.*, vol. 88, p. 035009, 2016. (Cited on page 67.)

[65] J. C. Myland and K. B. Oldham, "Uncompensated Resistance. 1. The Effect of Cell Geometry", *Analytical Chemistry*, vol. 72, no. 17, pp. 3972–3980, 2000. (Cited on page 85.)

[66] K. B. Oldham and N. P. C. Stevens, "Uncompensated Resistance. 2. The Effect of Reference Electrode Nonideality", *Analytical Chemistry*, vol. 72, no. 17, pp. 3981–3988, 2000. (Cited on page 85.)